# Three-Dimensional Forward Modelling and Inversion for the CSAMT Method Using Unstructured Grids

by

©Kadir Bahadır Kara

A thesis submitted to the School of Graduate Studies in partial fulfillment of the requirements for the degree of

**Master of Science**

**Department of Earth Sciences**

Memorial University of Newfoundland

January 2022

St. John's Newfoundland and Labrador

# Abstract

Three-dimensional forward-modelling and inversion problems are investigated for the controlled-source audio-frequency magnetotelluric (CSAMT) method and both forward-modelling and inversion codes written. The finite-element (FE) method, which is a numerical method for obtaining approximate solutions to boundary-value problems, is used for forward modelling. A potential formulation, specifically the decomposition of the electric field into vector and scalar potentials for the Helmholtz and the conservation of charge equations, is used. Vector and scalar basis functions are used for the potentials. The equations are discretized using the weighted residual method, which results in a sparse linear system. Modelling domains are subdivided into unstructured tetrahedral grids. The linear system is solved by the direct solver, MUMPS, with LU factorization. A number of examples are presented for the validation of the code. A minimum-structure method with Gauss-Newton iterations is used for the inversion. Iterative preconditioned conjugate gradient and nonpreconditioned generalized minimal residual methods are used to solve the linear systems of equations for the model updates. These solvers do not request explicit calculations of the matrices; therefore, this significantly reduces memory demand. Three benchmark tests are presented to verify the inversion code.

# Acknowledgements

I would like to thank my supervisor, Dr. Colin Farquharson, for his guidance and encouragement during my MSc program. I am grateful to Dr. Seyedmasoud Ansari for giving me permission to use his subroutine regarding intersections for the calculation of the source. I would like to thank Dr. Peter Lelièvre, who is the developer of the FacetModeller software, for making it available for us. I would like to also thank Drs. Hormoz Jahandari and Ming Zhang for sharing their numerical results with me.

I am grateful for the financial support provided by the Republic of Turkey Ministry of National Education. I am eternally grateful to Mustafa Kemal Atatürk, who is the founder of the Republic of Turkey and who enshrined this scholarship in law. Last but not least, I would like to thank each member of my family and fiancée; I could not complete my study without their supports.

# Table of Contents

# List of Tables

# List of Figures

# Chapter 1

# Introduction

Electromagnetic (EM) methods, including profiling and sounding techniques, are used to determine the changes in the electrical conductivity of the earth with both depth and laterally. These methods include methods that use natural and artificial sources and which operate in the time and frequency domains. Most EM measurements are conducted at a number of frequencies or times using fixed source and receiver locations since the strength of the EM fields depends on the earth's conductivity and signal frequency (Spies and Frischknecht, 1991). The controlled-source audio-frequency magnetotelluric (CSAMT) method is a frequency-domain EM method that uses a grounded dipole or horizontal loop as a source. Since the source ensures a stable and reliable signal, the method is more able to determine the earth conductivity than methods using a natural source. One or two sources can be used depending on the consideration of surveys and the geologic complexity of the survey area (e.g., Bartel and Jacobson, 1987; Boerner et al., 1993; Wannamaker, 1997). Apparent resistivity and phase are defined by using mutually orthogonal electric (**E**) and magnetic (**H**) fields (Sandberg and Hohmann, 1982; Zonge and Hughes, 1991).

The CSAMT method has been used in geophysical exploration applications such as mineral explorations (Sasaki et al., 1992; Boerner et al., 1993; Başokur et al., 1997;

Wang et al., 2018), geothermal explorations (Sandberg and Hohmann, 1982; Wannamaker, 1997; Savin et al., 2001), hydrocarbon explorations (Bartel et al., 1981; Hughes and Carlson, 1987), and aquifer explorations (Fu et al., 2013; Pedrera et al., 2016; Šumanovac and Orešković, 2018).

Many methods have been used for the numerical modelling of controlled-source electromagnetic methods (CSEM) as a result of developments in computer science. Although integral-equation (IE) formulations are one of the difficult methods for modelling in terms of mathematics, unknown fields only need to be found in anomalous regions. Hence, the memory demand of IE solutions is less than other modelling methods, and the method attracted attention in the early days of 3D modelling (e.g., Hohmann, 1975; Wannamaker et al., 1984). However, the method becomes very complicated for complex geology (Hohmann, 1983; Avdeev, 2005). In three-dimensional (3D) CSEM modelling, another widely used method is the finite difference (FD) method using rectangular cells (e.g., Newman and Alumbaugh, 1995; Streich, 2009; Li and Han, 2017; Lin et al., 2017; Wang and Tan, 2017). The implementation of the FD method is easier than other methods, and the method allows modelling of the entire region of interest. In the so-called staggered scheme (Yee, 1966), electric field components are calculated on the edges of the cells while magnetic field components are calculated on the faces of the cells, or vice versa.

Due to the inflexibility of the traditional rectangular grids, the FD method may cause inadequate results in 3D modelling. In other words, real geological features such as contacts between rock units and topography require powerful and flexible modelling. In contrast to the traditional FD method, different types of grids can be used for the

finite element (FE) and finite volume (FV) methods (e.g., for the FE method: Mitsuhata, 2000; Mitsuhata and Uchida, 2004; Ansari and Farquharson, 2014; for the FV method: Haber et al., 2007; Lu and Farquharson, 2020). Even though quadtree and octree grids, which have child rectangular and prismatic elements where they are desired, are computationally more efficient than unstructured grids (see, Haber et al., 2007), these grids do not provide as much flexibility as unstructured girds for geological structures. They cause stair-casing and pixelation in the modelling domain. In this study, the FE method is used for the forward-modelling of the CSAMT method with unstructured girds. The method has been successfully applied to CSEM modelling (e.g., Badea et al., 2001; Schwarzbach et al., 2011; Dunham et al., 2018), and detailed information is given by Coggon (1971) about the FE method. The main attraction to the FE method is that the method can overcome topography and bodies that have arbitrary shapes in complex geology by using unstructured tetrahedral elements. Also, the unstructured tetrahedral elements can be refined locally where desired or can be chosen coarser depending on the problem; therefore, the desired accuracy can be obtained with a reasonable number of grids.

The solution of the FE method can be obtained by weighting of the differential equations, or minimizing a functional, the result of which is equivalent to the differential equations (Sadiku 2001; Jin, 2014). In these equations, the unknown parameters, either the E or H fields, are approximated by using scalar or vector interpolation (basis) functions. By defining the scalar interpolation functions at nodes for each tetrahedron element in a 3D domain, fields are interpolated, and these functions ensure the tangential continuous condition of the electric field between different conductivities (e.g., Mogi, 1996). However, the node-based FE method

contravenes the discontinuity condition for the normal component of the electric field, and further, the electric field does not satisfy the divergence-free condition in source-free elements. To meet the necessary conditions, the vector-based FE method introduced firstly by Whitney (1957) can be used. The application of the vector-based FE method is given by Nédélec (1980) for tetrahedral elements, and applications of the method to geophysical EM problems are given by, e.g., Schwarzbach (2009), Farquharson and Miensopust (2011), Castillo-Reyes et al. (2018). The electric field is approximated along the edges by using vector basis functions in all these studies. This satisfies the necessary interface boundary conditions of the electric fields.

EM modelling can be done by using either direct E-field methods or potential methods. The commonly used method, in potential methods, is the **A**-$\phi$ decomposition in which potentials are expressed as magnetic vector (**A**) and electric scalar ($\phi$) potentials (for the FD method: Haber et al., 2000, Weiss, 2013; for the FE method: Badea et al., 2001, Ansari and Farquharson, 2014; for the FV method, Jahandari and Farquharson, 2015, Lu and Farquharson, 2020). Other decompositions can also be applied (e.g., Mitsuhata and Uchida, 2004). Since frequencies are very low in exploration geophysics, the linear system of the direct E-field method is poorly conditioned compared to the potential methods. Therefore, iterative solvers struggle to solve the systems. However, the linear system can be solved by using direct solvers. Because the **A**-$\phi$ approach gives a better conditioned linear system, which is more computationally expensive, the linear system of the method can be solved by either iterative solvers or direct solvers. A comparison is given by Ansari and Farquharson (2014). Also, **A**-$\phi$ methods provide the potentials separated into galvanic and

inductive parts (Ansari and Farquharson, 2014; Jahandari and Farquharson 2015; Lu and Farquharson, 2020). The galvanic part is the contribution from the direct flow of current through the subsurface, and across interfaces and conductivity gradients, whereas the inductive part is the contribution from eddy currents and the linkage between different parts of a current system by the time-varying magnetic field.

Even though the coefficient matrices of both systems are very sparse, direct solvers are more expensive in terms of memory compared to iterative solvers. On the other hand, the advantage of the direct solvers over iterative solvers is that they allow factorizations to be reused after a solution step. This is particularly significant for the CSAMT method because data acquisition of the method can be made by using more than one source. This means that only the right-hand side of the linear system will change for the forward modelling; therefore, the factorized matrix can be reused for multiple sources without additional computational effort. Furthermore, this feature is also important for inversions when a gradient-based method is used to invert a data-set. In this case, the calculation of the sensitivities is required, and the factorized left-hand side matrix can be reused for this calculation.

Inversion methods can be mainly separated into local (gradient-based) and global methods. Although global methods have the ability to reach the global minimum and use less memory, due to their nature, they have to call the forward-modelling operator many times. Therefore, gradient-based methods have become more attractive for higher dimensional inversions. The most favored gradient-based methods are the Newton and conjugate-gradient methods, and their variants such as Gauss-Newton (GN), nonlinear conjugate-gradient (NLCG), and quasi-Newton (QN). These methods

have been extensively used by researchers; reviews and strategies about the methods are given by Newman and Hoversten (2000), Avdeev (2005), Siripunvarapron (2012). In this study, the GN method is used. The GN method results in stable and computationally efficient Hessian matrices; hence, the method has been used for many EM studies (e.g., Mackie and Madden, 1993; Haber et al., 2000b; Sasaki, 2001; Usui et al., 2017).

In the GN method, the Jacobian or sensitivity matrix, which contains the derivatives of the data with respect to the model parameters, must be calculated in each iteration. Although some closed-form expressions are available for some EM models, generally, numerical methods are preferred for calculating Jacobian matrices. (An overview for the DC method is given by Spitzer, 1998.) Traditionally, each column of the Jacobian matrix can be formed by perturbing each model parameter in turn, carrying out a forward modelling for each perturbed model, and calculating a finite-difference approximation to the derivatives. The method requires as many forward modellings as the number of model parameters. When the number of parameters is considered in three-dimensional inverse problems, this is prohibitive. Another method is to use an adjoint-equation approach in which adjoint electric fields are computed for sources at the observation locations, and the inner products of these adjoint fields with the forward-modelled electric field computed. This method requires as many forward modellings as there are data to generate the Jacobian matrix (see Rodi, 1976; Mackie and Madden, 1993). Although the number of data are usually a lot less than the number of parameters in geophysical inversions, and explicit calculation of the transpose of the Jacobian matrix with direct solvers seems to be possible, the matrix requires a large amount of memory due to it being a full, and dense matrix. However,

iterative solvers such as conjugate gradient (CG) and generalized minimal residual (GMRES) do not require explicit knowledge of the Jacobian and GN matrices to solve the linear system but instead require only the results of the products of these matrices with the CG or GMRES vectors.

The CG method has attracted more attention due to its applicability to either solution of the linear systems (e.g., Mackie and Madden, 1993; Zhang et al., 1993; Günther et al., 2006; Siripunvaraporn and Egbert, 2009) or the minimization problems (e.g., Newman and Alumbaugh, 2000; Rodi and Mackie, 2001; Newman and Bogss, 2004) in geophysical inversion. The method can calculate a new vector only using the previous vector called conjugacy based on linear relations; this property provides the method with memory efficiency. Further, the convergence rate of the method can be accelerated by using a preconditioner (Haber, 2004). However, the GMRES solver introduced by Saad and Schultz (1986) has greater stability than the CG solver. The solver uses the Arnoldi process for constructing an $l_2$-orthogonal basis of Krylov subspaces. Also, the solver has the capability to solve nonsymmetric matrices. There are a few applications for geophysical inverse problems in the literature (Jahandari and Farquharson, 2017; Ansari et al., 2018; Ansari and Craven, 2020). In this study, both solvers, preconditioned CG and nonpreconditioned GMRES, are implemented.

As mentioned above, generally, the number of parameters needed to be determined is much greater than the amount of data in geophysical inversions. This means that inversions are under-determined. Also, the measured data includes some uncertainties. Therefore, many models can be found which fit the measured data. Further geological information is vital for the reliability of inversions and to reduce the ambiguity of

inversions. Geological constraints can be incorporated by using relations of adjacent cells (Li and Oldenburg, 1996; Bosch et al., 2001; Lelièvre and Oldenburg, 2009; Farquharson, 2007). Here, minimum-structure inversion is used for the CSAMT method. This procedure has been applied for the inversions of various geophysical methods (e.g., Li and Oldenburg, 1996; Farquharson and Oldenburg, 1998; Günther et al., 2006; Lelièvre and Farquharson, 2013; Mosher and Farquharson, 2013). An objective function, which is the sum of the measures of data misfit and model structure, is minimized by the GN method. $l_2$ measures are used for the data misfit and model structure; nonetheless, different types of measures can be used (see Farquharson and Oldenburg, 1998; Farquharson, 2007).

The purpose of this study is to develop an interpretation tool for the CSAMT method. For this purpose, new three-dimensional forward-modelling and inversion codes have been developed. The FE method is applied to obtain the forward-modelling responses in the new algorithm, and computational domains are discretized with unstructured grids. The new inversion code uses a minimum-structure inversion procedure with the GN method. Software FacetModeller (Lelièvre et al., 2018) and TetGen (Si, 2015) are used for building models and generating unstructured tetrahedral grids. The direct solver MUMPS (Amestoy et al., 2001) is used for forward modelling and the pseudo forward modelling used in the sensitivity computations. Also, SPARSKIT (Saad, 1990) is used in some parts of the developed code for sparse matrix-vector operations. Forward-modelling and inversion programs, as well as preconditioned CG and nonpreconditioned GMRES solvers, are coded in the Fortran language. A number of examples are given from simple to complex for both forward modelling and inversion to verify the codes.

# Chapter 2

# The Controlled-Source Audio-Frequency Magnetotelluric Method

## 2.1 Introduction

The controlled-source audio-frequency magnetotelluric (CSAMT) method, which was introduced by Goldstein (1971), is one of the electromagnetic methods using grounded electric wires and large magnetic loops as sources. The method is similar to magnetotelluric (MT) and audio-frequency magnetotelluric (AMT) methods, which use natural sources. The advantage of the CSAMT method over the natural-source methods is that it has high signal strength due to the artificial sources. This ensures the CSAMT method is able to investigate the top 2-3 km of the subsurface efficiently (Zonge and Hughes, 1991).

Generally, the grounded electric wire, whose length is about 1 to 3 km, is used as a source of the CSAMT method. If the distance between source and sounding areas is at least 3 to 4 km (with this distance depending on ground conductivity and transmitter frequency), the fields at the sounding area can be considered as plane waves and thus treated like in the MT method. The sounding frequency ranges from 0.1 Hz to 10 kHz, and orthogonal electric and magnetic field components are measured over this frequency range. The measurements of electric fields are made parallel to the

transmitter, and there are two configurations: broadside and collinear. While the broadside configuration refers to measuring the electric field parallel to the transmitter and on its centerline, the collinear configuration refers to measuring the electric field parallel to the transmitter and on its axis (Sandberg and Hohman, 1982, see Figure 2.1). The electric fields are measured by an electric dipole whose length is 10 to 150 m, and the dipole is terminated by two nonpolarizing potential electrodes. A third electrode can be used to determine noise by locating it at the center of the dipole. The electric field measurements include the potential difference between the potential electrodes and the associated phase angle reference to the source signal. The magnetic field is measured by using magnetic field antenna. The magnetic field measurement, which is done simultaneously with the electric field measurement, resembles the electric field measurement and consists of a voltage and phase angle. Horizontal electric and magnetic fields that are perpendicular to each other are used to determine apparent resistivity (Zonge and Hughes, 1991).

## 2.2 Measurement types of the CSAMT method

Depending on the complexity of the geology and the consideration of surveys, a CSAMT measurement can involve from two individual components to ten individual components. Two individual components correspond to a scalar measurement (e.g., $E_x$ and $H_y$) and ten individual components correspond to a tensor measurement (e.g., $E_{x1}$, $E_{x2}$, $E_{y1}$, $E_{y2}$; see Figure 2.1). CSAMT measurements can be classified as scalar, vector and tensor measurements associated with measured components and the number of sources used. The tensor measurements can overcome complex geological structures, and the measurements can be used to map geological features directly due

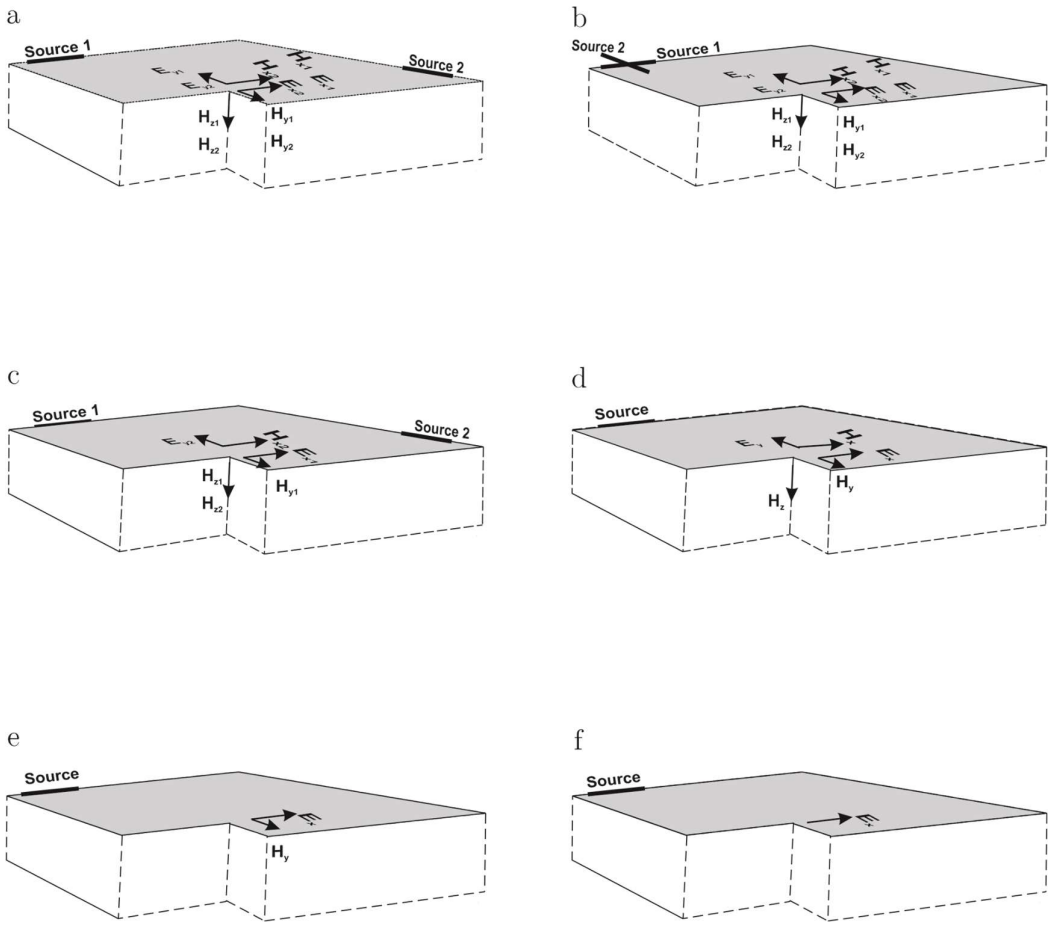


Figure 2.1 CSAMT measurement types: a) tensor separated-sources configuration, b) tensor coinciding sources configuration, c) partial-tensor configuration using separated sources, d) vector CSAMT measurement, e) scalar CSAMT measurement, and f) scalar CSAET measurement (adapted from Zonge and Hughes, 1991).

to the high survey resolution when soundings are made closer together. The tensor CSAMT measurements include five components ($E_x$, $E_y$, $H_x$, $H_y$, and $H_z$) for each of two sources. Nonetheless, this type of measurement is tedious compared to other measurement types due to the use of two sources. As shown in Figure 2.1a-c, the tensor survey can be conducted by separated or coinciding sources. The separated-source configuration ensures widely separated polarizations; hence, the configuration approximates the natural-source measurements. Nevertheless, the use of the configuration may cause problems such as source overprint effect on measurements if

the geological features are significantly different between these sources. The effect is directly related to the physical and geometric structures of survey areas, and it may affect the whole survey (Zonge and Hughes, 1991; Hughes and Carlson, 1987). Since the sources are located at the same place in the coinciding-source configuration, a source overprint effect is less likely to occur. Further, this measurement type is easier in terms of fieldwork. If the geologic strike is known, the sources are oriented to be strike parallel and perpendicular. However, an arbitrary orientation can be used if the strike direction is unknown. In addition, partial-tensor configurations (Figure 2.1c) can be used as well if the strike is well known.

The vector measurement (Figure 2.1d), which uses a single source, can be used by measuring four or five components ($E_x$, $E_y$, $H_x$, $H_y$, $H_z$) in complex geology. Although this type of system involves less data than the tensor configurations due to the use of the single source, the vector measurement is efficient to determine two-dimensional (2D) and three-dimensional (3D) geological features when regional anisotropy does not dominate. In other words, when resistivities do not depend on the directions, it can be used for the definition of complex geological structures (Zonge and Hughes, 1991).

The scalar CSAMT (Figure 2.1e) measurement consists of two components $E_x$, $H_y$ or $E_y$, $H_x$, and the measurement is run by using a single source polarization. The measurement is adequate to determine one-dimensional (1D) geological structures. However, it can be used for 2D and 3D modelling by increasing data acquisition density if again survey areas are isotropic. The main advantage of the scalar measurement is high data acquisition speed. Lastly, controlled-source audio-frequency electrotellurics (CSAET) including only one component of the electric field

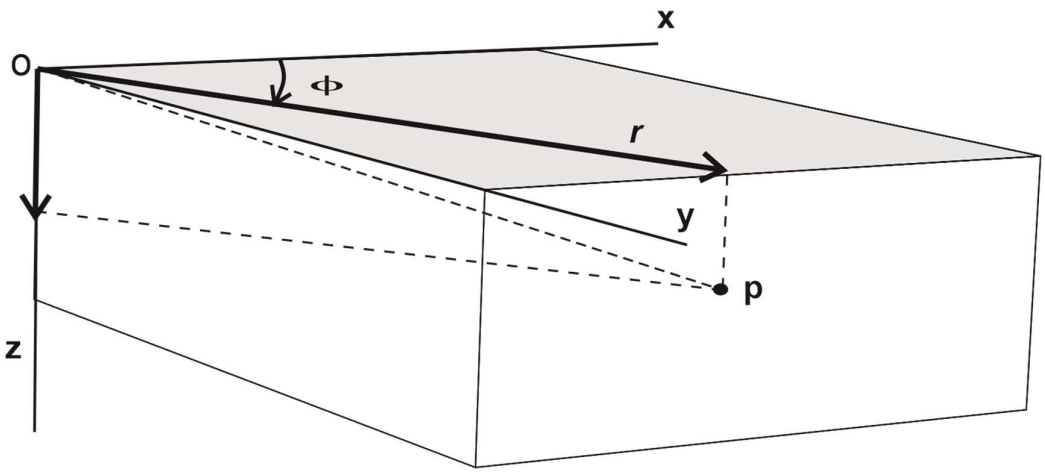


Figure 2.2 Demonstration of the geometric parameters in cylindrical coordinates.

is a simple version of the scalar CSAMT measurement. This type of system, generally, is used in survey areas in which the magnetic field is fairly uniform, and the magnetic field is measured at a few stations to calculate the resistivity. However, it may cause significant errors in the calculation of resistivity (Zonge and Hughes, 1991).

### 2.3 The effect of the physical and geometric parameters on data

Not only can physical parameters affect the CSAMT data, but geometric parameters, source-sounding separation ($r$), and angle between source and sounding locations ($\phi$) also can have an influence on the data. Figure 2.2 shows the geometric measurement parameters in cylindrical coordinates.

A survey area can be divided into three regions in accordance with the wavenumber ($k = (i\mu\sigma\omega)^{1/2}$ where $\mu$ is the magnetic permeability, $\sigma$ is the electrical conductivity, $\omega$ is the angular frequency, and $i$ is the imaginary unit) and separation ($r$). The region electrically near the transmitting source is defined by small induction numbers

($|kr| \ll 1$) and is known as the near-field zone. The region electrically far from the dipole is defined by a large induction number ($|kr| \gg 1$) and is known as the far-field zone. The region between these zones is known as the transition zone. Since the wavenumber is related to the frequency and resistivity, they have a direct link with these zones. The effect of $r$ is given for a homogeneous earth whose conductivity is $10^{-3}$ S/m by using the broadside configuration in Figure 2.3a. The distance and frequencies change from 1 to 16 km and from 1 and 4096 Hz, respectively, and $\phi$ is 90°. The magnetic field reduces sharply when $r$ increases. This causes the apparent resistivity values to approach the actual resistivity value. Figure 2.3b shows the dependence of the data on the ground resistivity as it changes from 16 to 4096 Ωm. $r$ and $\phi$ are fixed at 4 km and 90°, respectively. The magnetic field reduces sharply; for the low resistivity values, the reductions are seen for even low frequencies. Therefore, the near-field zone is smaller in conductive regions. The behavior of the electric and magnetic fields as $\phi$ varies is given in Figure 2.3c. The angle changes from 0 to 60°, and the conductivity of the earth is $10^{-3}$ S/m. $r$ is 4 km. The fields are affected sharply at low frequencies; hence, apparent resistivity is affected by the angle changing in the near field. Each graph has a notch that shows the transition zone, and it is clearer for 60° in Figure 2.3c.

Further, there are other parameters such as topography that can affect the data. Any electromagnetic measurement is affected by current density changes due to the topography. For instance, valleys in which resistivities are artificially high result in higher current densities. The opposite situation occurs in hills. Therefore, topography should be considered in CSAMT modelling.

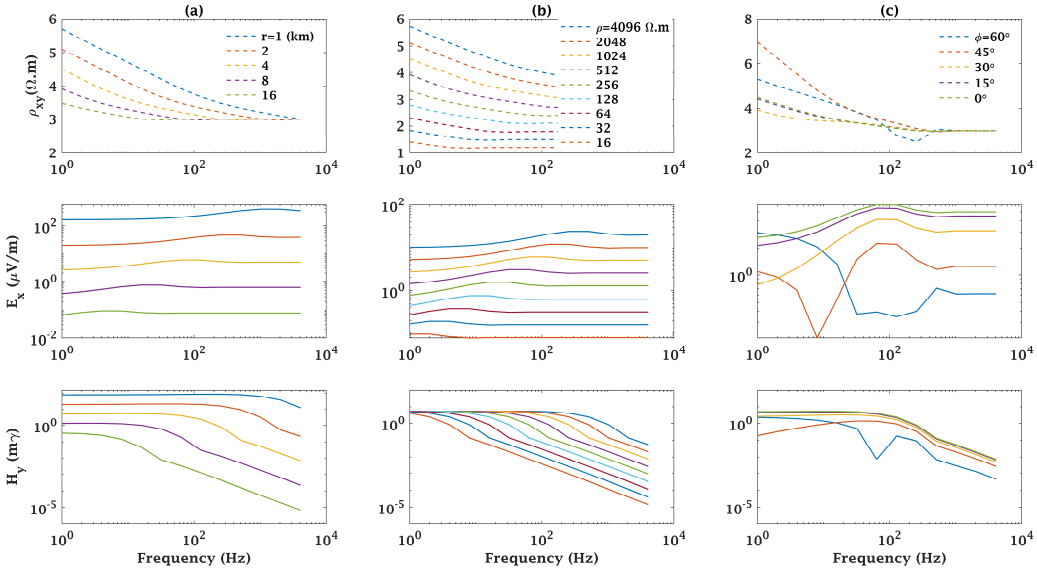


Figure 2.3 Influence of the variables on CSAMT measurements: a) separation, b) ground resistivity, and c) angle (adapted from Zonge and Hughes, 1991).

## 2.4 Calculation of apparent resistivity and phase

As mentioned in Section 2.1 and above, if the observation locations are in the far-field of a source, the fields can be considered as plane waves and the MT equations for apparent resistivity and phase used. The scalar impedance (Z) is defined as the ratio of the orthogonal components of the E and H fields:

$$Z = \left| \frac{E}{H} \right| \tag{2.1}$$

The apparent resistivity is given by

$$\rho = \frac{1}{\omega \mu_0} |Z|^2 \tag{2.2}$$

where $\omega$ is the angular frequency and $\mu_0$ is the magnetic permeability of free space, and phase ($\varphi$) can be calculated by

$$\varphi = Arg\left(\frac{\Im(Z)}{\Re(Z)}\right) \tag{2.3}$$

where $\Im$ and $\Re$ show imaginary and real parts of the impedance (Zonge and Hughes, 1991). The tensor impedance is given as

$$\begin{bmatrix} E_x \\ E_y \\ E_z \end{bmatrix} = \begin{bmatrix} Z_{xx} & Z_{xy} & Z_{xz} \\ Z_{yx} & Z_{yy} & Z_{yz} \\ Z_{zx} & Z_{zy} & Z_{zz} \end{bmatrix} \begin{bmatrix} H_x \\ H_y \\ H_z \end{bmatrix} \tag{2.4}$$

The z-component of the $E$ field ($E_z$) is very small at low frequencies; hence, this component is not measured. In this case, the tensor impedances become

$$\begin{aligned} E_x &= Z_{xx}H_x + Z_{xy}H_y \\ E_y &= Z_{yx}H_x + Z_{yy}H_y \end{aligned} \tag{2.5}$$

Equations 2.5 show that there is a mutual dependence between $E$ and $H$ fields. Unlike natural-source measurements, the source of the CSAMT method does not have an infinite number of polarizations due to its finite location and orientation. Therefore, tensor measurements require ten components. In accordance with this, Equation 2.5 can be written as

$$\begin{aligned} E_{x1} &= Z_{xx}H_{x1} + Z_{xy}H_{y1} \\ E_{y1} &= Z_{yx}H_{x1} + Z_{yy}H_{y1} \end{aligned} \tag{2.6}$$

$$\begin{aligned} E_{x2} &= Z_{xx}H_{x2} + Z_{xy}H_{y2} \\ E_{y2} &= Z_{yx}H_{x2} + Z_{yy}H_{y2} \end{aligned} \tag{2.7}$$

in which the subscripts 1 and 2 denote source numbers. From Equations 2.6 and 2.7, the tensor impedances are obtained as

$$Z_{xx} = \frac{E_{x1}H_{y2} - E_{x2}H_{y1}}{H_{x1}H_{y2} - H_{x2}H_{y1}} \tag{2.8}$$

$$Z_{yy} = \frac{E_{y1}H_{x2} - E_{y2}H_{x1}}{H_{x2}H_{y1} - H_{x1}H_{y2}} \tag{2.9}$$

$$Z_{xy} = \frac{E_{x2}H_{x1} - E_{x1}H_{x2}}{H_{x1}H_{y2} - H_{x2}H_{y1}} \tag{2.10}$$

$$Z_{yx} = \frac{E_{y2}H_{x1} - E_{y1}H_{y2}}{H_{x2}H_{y1} - H_{x1}H_{y2}} \tag{2.11}$$

In the 3D case, components are nonzero and not equal, unlike in 1D and 2D cases. Since the main objective of tensor measurements is to determine structures, the impedances can be rotated in accordance with a strike (see Zonge and Hughes, 1991). Lastly, the vector measurements are useful in areas of complex geology, as mentioned in Section 2.2. Although the full tensor is not determined due to the use of only one source polarization, scalar impedance based on polarization ellipse orientations can be used.

However, the full impedance tensor cannot be determined when only one source polarization is used. A rotationally constant scalar impedance is obtained by choosing scalar field components oriented along the major axes of the polarization ellipse. To calculate the impedance independent of the coordinate system, the phase of the electric field polarization-ellipse maximum is given as:

$$\varphi = 0.5 \tan^{-1}\left[\frac{\Im\left(E_x^2 + E_y^2\right)}{\Re\left(E_x^2 + E_y^2\right)}\right] \tag{2.12}$$

and orientation is given by:

$$\theta = \tan^{-1}\left(\frac{\Re\left(E_y e^{i\varphi}\right)}{\Re\left(E_x e^{i\varphi}\right)}\right) \tag{2.13}$$

The electric field component parallel to the major axis of the ellipse ($E_m$) is obtained from:

$$E_m = E_x \cos\theta + E_y \sin\theta \tag{2.14}$$

The magnetic field component ($H_m$) can be obtained in a similar way. $E_m$ and $H_m$ are nearly orthogonal, and the scalar impedance is calculated by:

$$Z_m = \left|\frac{E_m}{H_m}\right| \tag{2.15}$$

The corresponding apparent resistivity and phase are then calculated using Equations 2.2 and 2.3 (Zonge and Hughes, 1991).

# Chapter 3

# Finite Element Boundary Value Problems in the Frequency Domain

## 3.1 Introduction

All electromagnetic phenomena are described by the empirical Maxwell's equations, which are a set of four equations. Maxwell's equations are uncoupled first-order linear differential equations; however, they are connected by constitutive relations. Although Maxwell's equations can be solved analytically for some models, the solutions are restricted to simple and unrealistic cases such as wholespaces and halfspaces and some simple geometric shapes. However, analytical solutions are useful to check the accuracy of numerical solutions (Sadiku, 2001; Ward and Hohmann,1988).

This chapter begins with a brief description of Maxwell's equations in the time and frequency domains and the relevant boundary conditions. Then the FE method is explained for the vector and scalar potentials using the Helmholtz equation and the equation of conservation of charge.

## 3.2 Maxwell's equations and boundary conditions

EM fields are explained with four equations; in the time domain, Maxwell's equations in their differential and integral forms are:

$$\nabla \times \mathbf{E} + \frac{\partial \mathbf{B}}{\partial t} = 0 \qquad \oint_C \mathbf{E} \cdot d\mathbf{l} + \iint_S \frac{\partial \mathbf{B}}{\partial t} \cdot d\mathbf{S} = 0 \tag{3.1}$$

$$\nabla \times \mathbf{H} - \frac{\partial \mathbf{D}}{\partial t} = \mathbf{J} \qquad \oint_C \mathbf{H} \cdot d\mathbf{l} - \iint_S \frac{\partial \mathbf{D}}{\partial t} \cdot d\mathbf{S} = \iint_S \mathbf{J} \cdot d\mathbf{S} \tag{3.2}$$

$$\nabla \cdot \mathbf{B} = 0 \qquad \oiint_S \mathbf{B} \cdot d\mathbf{S} = 0 \tag{3.3}$$

$$\nabla \cdot \mathbf{D} = \rho \qquad \oiint_S \mathbf{D} \cdot d\mathbf{S} = \iiint_V \rho dV \tag{3.4}$$

Equation 3.1 is known as Faraday's law and states that time-varying magnetic flux density **B**, through a surface, generates electric field intensity, **E**, around the outline of the surface. The second Maxwell's equation (Equation 3.2) is Ampère's law: the law states that the line integral of the magnetic field intensity **H** around a closed path is equal to the total current flowing through the surface enclosed by the path. Relation 3.3 is the law of conservation of magnetic flux or Gauss's law: the law states that there is no monopole; in other words, the total magnetic flux density **B**, through any closed surface, is zero. The last equation is Coulomb's law which states that the flux of the displacement current **D** through a closed surface is equal to the electric charge density in the volume that is enclosed by the surface (Sadiku, 2001). **J** is the electric current density; it is given by Ohm's law which is one of the constitutive relations and explains the relation between **E** and **J**:

$$\mathbf{J} = \sigma \mathbf{E} \tag{3.5}$$

where σ is the electrical conductivity. The other two constitutive relations explain the relation between **B**-**H** and **D**-**E**:

$$\mathbf{B} = \mu\mathbf{H} \tag{3.6}$$

$$\mathbf{D} = \varepsilon\mathbf{E} \tag{3.7}$$

where, $\mu$ and $\varepsilon$ are magnetic permeability and dielectric permittivity, which are assumed to be linear and isotropic. Also, magnetic permeability is normally taken to be $\mu=\mu_0$ which is the magnetic permeability of free space. Due to the use of low frequencies in the CSAMT method, the quasi-static approximation, in which the displacement current **D** is ignored, can be used (Ward and Hohmann, 1988). Therefore, electrical conductivity is the only variable for earth models.

Using the Fourier transform, Faraday's and Ampère's laws can be written in the frequency domain:

$$\nabla \times \mathbf{E} + i\omega\mathbf{B} = 0 \tag{3.8}$$

$$\nabla \times \mathbf{H} - i\omega\mathbf{D} = \mathbf{J} \tag{3.9}$$

where $i = \sqrt{-1}$ and $\omega$ is the angular frequency (Ward and Hohmann, 1988). An EM problem is a boundary value problem that should satisfy both differential equations and boundary conditions; in other words, the problem should incorporate information about both the behaviour of the fields throughout the domain as well as on the boundary of the domain. The boundary conditions at the interface between two media, namely medium 1 and 2, are given as the following:

$$E_{1t} = E_{2t} \tag{3.10}$$

$$H_{1t} = H_{2t} \tag{3.11}$$

$$B_{1n} = B_{2n} \tag{3.12}$$

$$J_{1n} = J_{2n} \tag{3.13}$$

$$D_{1n} - D_{2n} = \rho \tag{3.14}$$

where subscripts *t* and *n* are the tangential and normal components, respectively. The tangential components of the field intensities (Conditions 3.10 and 3.11) are continuous across the interface of two media. At the same time, the normal components of **B** and **J** are continuous at the interfaces of the media. Condition 3.13 is valid for the stationary situation, which says that $\partial\rho/\partial t = 0$; however, **J** is is not necessarily continuous at every instant in time (see Ward and Hohmann, 1988). However, the normal component of **D** is discontinuous across the interface because of the accumulation of electric charge density.

The boundary conditions should also be defined at the boundaries of the numerical domain. The attenuation of EM fields is exponential, and if there is a source in the problem region (as for most geophysical EM problem), and the boundaries are far enough from the source, then the first kind of boundary condition (Dirichlet) can be applied:

$$\left(\mathbf{n} \times \mathbf{E}\right)_{\Gamma} = 0 \tag{3.15}$$

where $\Gamma$ is the outer boundary, and **n** is the normal vector for the boundary surfaces. Other boundary conditions can be applied (see Sadiku, 2001; Jin, 2014).

### 3.3 Vector-scalar potentials formulation

Faraday's and Ampère's laws can be re-written for a region containing electric and magnetic sources with a time dependence of $e^{i\omega t}$:

$$\nabla \times \mathbf{E} + i\omega \mathbf{B} = -\mathbf{J}_m^s \tag{3.16}$$

$$\nabla \times \mathbf{H} - \sigma \mathbf{E} = \mathbf{J}_e^s \tag{3.17}$$

where $\mathbf{J}_m^s$ and $\mathbf{J}_e^s$ are magnetic and electric current density source terms, respectively (Ward and Hohmann, 1988). These two equations are first-order linear differential equations, and the E-field equation, i.e., the second-order partial differential equation (PDE), can be obtained by taking the curl of Equation 3.16 and using Equation 3.17:

$$\nabla \times \nabla \times \mathbf{E} + i\omega\mu_0\sigma \mathbf{E} = -i\omega\mu_0 \mathbf{J}_e^s - \nabla \times \mathbf{J}_m^s \tag{3.18}$$

which is the general form for the decoupled Helmholtz equation. From Maxwell's equations, **B** is divergence-free ($\nabla \cdot \mathbf{B} = 0$); therefore, it can be expressed as the curl of a vector potential **A**:

$$\mathbf{B} = \nabla \times \mathbf{A} \tag{3.19}$$

Substituting Equation 3.19 into Equation 3.16 gives

$$\nabla \times \left( \mathbf{E} + i\omega \mathbf{A} \right) = 0 \tag{3.20}$$

Since the curl in Equation 3.20 equals zero, the term in parentheses can be expressed as the gradient of a scalar, giving

$$\mathbf{E} = -i\omega \mathbf{A} - \nabla \phi \tag{3.21}$$

where $\phi$ is the scalar potential and its sign is arbitrary (Ward and Hohmann, 1988). However, this decomposition suffers from non-uniqueness. To overcome this non-uniqueness, the Coulomb gauge condition, suppressing the freedom of vector potential, is frequently used (Equation 3.22):

$$\nabla \cdot \mathbf{A} = 0 \tag{3.22}$$

Replacing **E** in Equation 3.18 with the potentials from Equation 3.21 gives

$$\nabla \times \nabla \times \mathbf{A} + i\omega\mu_0\sigma\mathbf{A} + \mu_0\sigma\nabla\phi = \mu_0\mathbf{J}_e^s - \frac{i}{\omega}\nabla \times \mathbf{J}_m^s \tag{3.23}$$

where **A** and $\phi$ are complex-valued functions associated with position and frequency. Lastly, this equation requires one more extra condition which is the conservation of charge which is given by

$$\nabla \cdot \mathbf{J} = \begin{cases} -\nabla \cdot \mathbf{J}^s & \text{at the source location} \\ 0 & \text{otherwise} \end{cases} \tag{3.24}$$

where the current density, **J**, is associated with the electric field by Ohm's law (**J**=σ**E**). Substituting Equation 3.21 into Equation 3.24 gives

$$-i\omega\nabla \cdot (\sigma\mathbf{A}) - \nabla \cdot (\sigma\nabla\phi) = -\nabla \cdot \mathbf{J}_e^s \tag{3.25}$$

The system of equations consisting of Equations 3.23 and 3.25 are square and diagonally dominant. To solve these equations, the boundary condition of the first kind (Dirichlet) can be applied.

$$(\mathbf{n} \times \mathbf{A})_\Gamma = 0 \tag{3.26}$$

$$\phi_{\Gamma} = 0 \tag{3.27}$$

The boundary conditions should be also defined at material interfaces for the potentials. As mentioned in Section 3.2, the tangential components of the field intensities are continuous between two media. Therefore, the tangential component of **A** and $\nabla\phi$ must be continuous at the interfaces of two media (Condition 3.28). The normal component of **A** is also continuous due to the Coulomb gauge condition (Condition 3.29). The decomposition satisfies the continuity of the normal component of the current density (Condition 3.30). Lastly, the normal component of $\nabla\phi$ is discontinuous between two media (Condition 3.31).

$$A_{1t} = A_{2t} \tag{3.28}$$

$$A_{1n} = A_{2n} \tag{3.29}$$

$$\sigma_1 \left( \mathbf{A} - \nabla\phi \right)_{1n} = \sigma_2 \left( \mathbf{A} - \nabla\phi \right)_{2n} \tag{3.30}$$

$$\nabla\phi_{2n} - \nabla\phi_{1n} = \frac{\rho}{\varepsilon} \tag{3.31}$$

### 3.4 The Finite Element Method

The general form of the boundary-value problem is given by the following equation in a domain, $\Omega$, which may be 1D, 2D, or 3D depending on a defined problem:

$$\mathcal{L}\mathcal{X} = f \tag{3.32}$$

where $\mathcal{L}$ is the differential operator, $\mathcal{X}$ is the unknown function to be determined, and $f$ is a known function. The differential operator ($\mathcal{L}$) also is self-adjoint, $\langle \mathcal{L}\mathcal{X}, \psi \rangle = \langle \mathcal{X}, \mathcal{L}\psi \rangle$; it can be seen by determining $\mathcal{X}$ and $\psi$ as real values for

convenience and using Green's identity. Conventionally, the Rayleigh-Ritz variational method, or Galerkin's, which uses the concept of the weighted residuals, can be used for the solution of a boundary-value problem. Nonetheless, Galerkin's method is more general and has wider applications than the Rayleigh-Ritz method since the method does not need a functional for the solution of a boundary-value problem (Sadiku, 2001; Jin, 2014). The analysis can be divided into four main steps, which are domain discretization, selection of the interpolation (basis) function, formulation of the system of equations, and solution of the system of equations.

### 3.4.1 Domain discretization

The domain discretization is the first and a significant step in finite element analysis since it will affect the accuracy of numerical results and computation time. Tetrahedral elements having four nodes can be used to subdivide a volume domain. In the general case, the tetrahedral element is the best choice for arbitrary shapes since it is more suitable for the boundary of an arbitrary domain. Further, the accuracy of the numerical results can be increased by using higher-order elements. In this case, the implementation of the method may become difficult (Sadiku, 2001; Jin, 2014).

Another important point is the structure of tetrahedral elements; they should not have narrow inner angles. Even though these kinds of elements are admissible, they may reduce the accuracy of the numerical solution. The error is inversely proportional to the sine of the smallest inner angle of an element (Jin, 2014). Moreover, the use of fine meshes for a domain increases the accuracy of the solution; however, this causes more unknown parameters and results in more memory being needed. Due to the rapid variations of the fields, small tetrahedral elements can be used around sources,

whereas coarse elements can be used towards the boundary. Furthermore, arrays related to the boundary nodes, the coordinates of each node, and the global numbers of each element, etc., are defined to impose prescribed values of a function on the boundary, i.e., the boundary conditions.

### 3.4.2 Scalar interpolation function

After domain discretization, the unknown function ( $\mathcal{X}$ ) within each element needs to be approximated. The typical (linear) tetrahedral element has four nodes (Figure 3.1). For each node numbered 1,2,3 and 4, $\mathcal{X}$ can be approximated as:

$$\tilde{\mathcal{X}}(x,y,z) = a^e + b^e x + c^e y + d^e z \tag{3.33}$$

$$\begin{aligned}
\tilde{\mathcal{X}}_1^e &= a^e + b^e x_1^e + c^e y_1^e + d^e z_1^e \\
\tilde{\mathcal{X}}_2^e &= a^e + b^e x_2^e + c^e y_2^e + d^e z_2^e \\
\tilde{\mathcal{X}}_3^e &= a^e + b^e x_3^e + c^e y_3^e + d^e z_3^e \\
\tilde{\mathcal{X}}_4^e &= a^e + b^e x_4^e + c^e y_4^e + d^e z_4^e
\end{aligned} \tag{3.34}$$

where $\tilde{\mathcal{X}}$ is an approximated function, and the coefficients $a^e$, $b^e$, $c^e$ and $d^e$ can be determined by enforcing Equation 3.33 at four nodes of the elements:

$$\tilde{\mathcal{X}}^e(x,y,z) = \sum_{j=1}^{4} N_j^e(x,y,z)\tilde{\mathcal{X}}_j^e \tag{3.35}$$

The $N_j^e(x,y,z)$ are interpolation functions that are given by

$$N_j^e(x,y,z) = \frac{1}{6V^e}\left(a_j^e + b_j^e x + c_j^e y + d_j^e z\right) \tag{3.36}$$

where $V^e$ is the volume of element

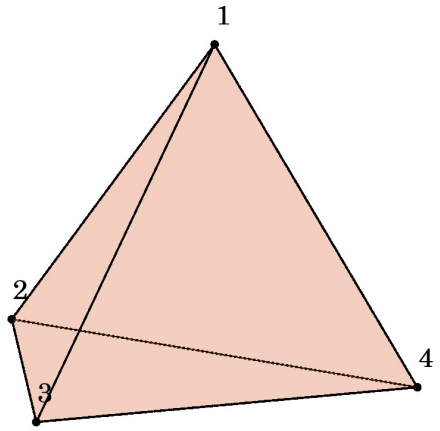


Figure 3.1 A linear tetrahedron element.

$$V^e = \frac{1}{6}\begin{vmatrix} 1 & 1 & 1 & 1 \\ x_1^e & x_2^e & x_3^e & x_4^e \\ y_1^e & y_2^e & y_3^e & y_4^e \\ z_1^e & z_2^e & z_3^e & z_4^e \end{vmatrix} \tag{3.37}$$

Also, the interpolation functions have the property:

$$N_i^e\left(x_j, y_j, z_j\right) = \delta_{ij} = \begin{cases} 1 & i = j \\ 0 & i \neq j \end{cases} \tag{3.38}$$

### 3.4.3 Vector interpolation function

Vector finite elements is an approach that assigns degrees of freedom to the edges instead of the nodes of the elements; for this reason, they are also called edge elements. The use of the node-based finite elements, calculated by interpolating the nodal values, causes some problems when vector electric or magnetic field equations are used. The first problem is nonphysical solutions due to the lack of enforcement of the divergence condition. The second one is the difficulty of imposing boundary

conditions at material interfaces. The last problem is an inconvenience in treating conducting and dielectric edges and corners due to field singularities (Jin, 2014). Although these types of elements were introduced by Whitney (1957), further discussion was given by Nédélec (1980) for tetrahedral elements.

Consider the tetrahedron element given in Figure 3.2. Its edge elements are shown associated with the nodes. If the scalar interpolation functions (Equation 3.36) are shown as $L_1^e$, $L_2^e$, $L_3^e$ and $L_4^e$, the corresponding vector function for the pair of nodes 1 and 2, can be written as:

$$\mathbf{W}_{12} = L_1^e \nabla L_2^e - L_2^e \nabla L_1^e \tag{3.39}$$

It can be easily seen that the vector function is divergence-free, which also means that the approximate function is also divergence-free within the element:

$$\nabla \cdot \mathbf{W}_{12} = \nabla \cdot \left( L_1^e \nabla L_2^e \right) - \nabla \cdot \left( L_2^e \nabla L_1^e \right) = 0 \tag{3.40}$$

Further, the following equation can be written:

$$\nabla \times \mathbf{W}_{12} = \nabla \times \left( L_1^e \nabla L_2^e \right) - \nabla \times \left( L_2^e \nabla L_1^e \right) = 2 \nabla L_1^e \times \nabla L_2^e \tag{3.41}$$

The curl of the vector function is nonzero; therefore, the basis functions and their curls are complete to the zeroth-order. Let $\mathbf{e}_1$ be the unit vector extending from node 1 to node 2 (Figure 3.2), $L_1^e$ is a linear function whose value changes from one to zero at nodes 1 and 2, respectively, and $L_2^e$ is a linear function whose value changes from $\mathbf{e}_1 \cdot \nabla L_2^e = 1 / \ell_1^e$ where $\ell_1^e$ is the length of the edge connecting nodes 1 and 2:

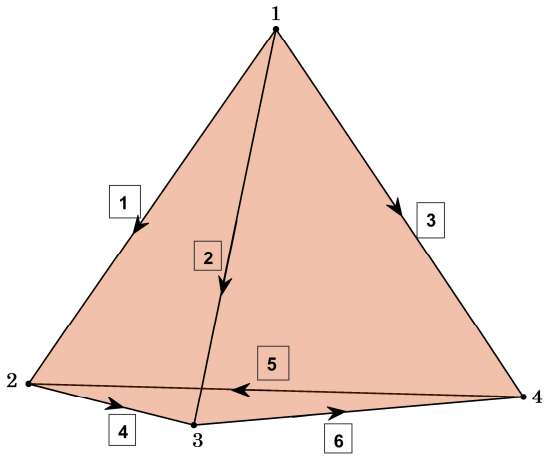


Figure 3.2 A tetrahedral element with its nodes and edges

$$\mathbf{e}_1 \cdot \mathbf{W}_{12} = \left( L_1^e + L_2^e \right) / \ell_1^e = 1 / \ell_1^e \tag{3.42}$$

It means that $\mathbf{W}_{12}$ has a constant tangential component along the edge (1,2); however, it has no tangential component along the other five edges because $L_1^e$ vanishes along edges (2,3), (2,4) and (1,2), and $L_2^e$ vanishes along edges (1,3), (1,4) and (3,4). Moreover, $\mathbf{W}_{12}$ has a tangential component on the element faces (1,2,3) and (1,2,4) because these faces contain edge (1,2). This vector function satisfies the necessary problems mentioned above (Jin, 2014). In its general form, the vector interpolation function is given as:

$$\mathbf{N}_j^e = \mathbf{W}_{j1j2} \ell_j^e = \left( L_{j1}^e \nabla L_{j2}^e - L_{j2}^e \nabla L_{j1}^e \right) \ell_j^e \tag{3.43}$$

### 3.4.4 Discretization of vector-scalar formulation

Galerkin's method, which is used here and is one of the weighted residual methods, starts with setting up the residual which is given by:

$$r = \mathcal{L}\tilde{\mathcal{X}} - f \neq 0 \tag{3.44}$$

The best approximation for $\tilde{\mathcal{X}}$ will be the one that reduces the residual $r$ to the least value at all points in a domain (Ω), i.e.,

$$R_i = \int_\Omega \left( w_i r \right) d\Omega = 0 \tag{3.45}$$

where $R_i$ denotes the weighted residual and $w_i$ are chosen weighting functions. The weighting function can be chosen to be the same as used for the expansion of the approximate solution. Using Equations 3.44 and 3.23, the vector residual can be obtained as:

$$\mathbf{r} = \nabla \times \nabla \times \tilde{\mathbf{A}} + i\omega\mu_0\sigma\tilde{\mathbf{A}} + \mu_0\sigma\nabla\tilde{\phi} - \mu_0\mathbf{J}_e^s + \frac{i}{\omega}\nabla \times \mathbf{J}_m^s \tag{3.46}$$

where $\tilde{\mathbf{A}}$ and $\tilde{\phi}$ are the approximated vector and scalar potentials, respectively. Equating the weighted residual (Equation 3.45) to zero gives:

$$\begin{aligned} \int_V \mathbf{W} \cdot \left( \nabla \times \nabla \times \tilde{\mathbf{A}} \right) dV + i\omega\mu_0 \int_V \sigma \mathbf{W} \cdot \tilde{\mathbf{A}} dV + \mu_0 \int_V \sigma \mathbf{W} \cdot \nabla\tilde{\phi} dV - \\ \mu_0 \int_V \mathbf{W} \cdot \mathbf{J}_e^s dV + \frac{i}{\omega} \int_V \mathbf{W} \cdot \nabla \times \mathbf{J}_m^s dV = 0 \end{aligned} \tag{3.47}$$

The first term in the left-hand side is integrated by parts:

$$\begin{aligned} \int_V \mathbf{W} \cdot \left( \nabla \times \nabla \times \tilde{\mathbf{A}} \right) dV = \int_V \left( \nabla \times \mathbf{W} \right) \cdot \left( \nabla \times \tilde{\mathbf{A}} \right) dV - \\ \int_{\gamma+\Gamma} \mathbf{W} \times \left( \nabla \times \tilde{\mathbf{A}} \right) \cdot \mathbf{n} dS \end{aligned} \tag{3.48}$$

By rearranging Equation 3.47 in accordance with Equation 3.48 gives:

$$\int_V (\nabla \times \mathbf{W}) \cdot \left(\nabla \times \tilde{\mathbf{A}}\right) dV - \int_{\gamma+\Gamma} \mathbf{W} \times \left(\nabla \times \tilde{\mathbf{A}}\right) \cdot \mathbf{n} dS + i\omega\mu_0 \int_V \sigma \mathbf{W} \cdot \tilde{\mathbf{A}} dV + \mu_0 \int_V \sigma \mathbf{W} \cdot \nabla \tilde{\phi} dV = \mu_0 \int_V \mathbf{W} \cdot \mathbf{J}_e^s dV \tag{3.49}$$

The surface integral term in Equation 3.49 expresses the behavior of the approximated vector potential at the inner, $\gamma$, and outer, $\Gamma$, boundaries of the mesh.

The same procedure can be applied to Equation 3.25 by using a scalar weight function:

$$r = -i\omega\nabla \cdot \left(\sigma \tilde{\mathbf{A}}\right) - \nabla \cdot \left(\sigma \nabla \tilde{\phi}\right) + \nabla \cdot \mathbf{J}_e^s \tag{3.50}$$

where $r$ is the scalar residual. Substituting this into Equation 3.45 and integrating by parts gives

$$i\omega \int_V \nabla W \cdot \sigma \tilde{\mathbf{A}} dV - i\omega \int_{\gamma+\Gamma} W \sigma \tilde{\mathbf{A}} \cdot \mathbf{n} dS + \int_V \nabla W \cdot \sigma \nabla \tilde{\phi} dV - \int_{\gamma+\Gamma} W \nabla \tilde{\phi} \cdot \mathbf{n} dS = -\int_V W \nabla \cdot \mathbf{J}_e^s dV \tag{3.51}$$

The surface integrals that are related to the inner boundaries in Equations 3.49 and 3.51 can be ignored. It can be seen that nodes that are not on boundaries will not have any contribution to the solution. All elemental surfaces directly connected to an internal node lie inside $V$ and are shared by two elements. Since the normal components of $\nabla \times \tilde{\mathbf{A}}$ and $\nabla \tilde{\phi}$ are continuous but the unit vector **n** changes sign between two connected elements, their contributions cancel each other. Therefore, only nodes residing on boundaries have contributions. Nonetheless, nodes residing on $\Gamma$ where homogeneous Dirichlet boundary conditions are applied are discarded; hence, these boundary nodes do not need to be considered (Jin, 2014).

Approximated vector and scalar potentials can be expressed with linear interpolation (basis) functions as described in detail in Sections 3.4.2 and 3.4.3:

$$\tilde{\mathbf{A}} = \sum_{j=1}^{n_{edges}} \tilde{A}_j \mathbf{N}_j \tag{3.52}$$

$$\tilde{\phi} = \sum_{k=1}^{n_{nodes}} \tilde{\phi}_k N_k \tag{3.53}$$

where $\mathbf{N}_j$ and $N_k$ are the vector and scalar interpolation functions, respectively. The numbers $n_{edges}$ and $n_{nodes}$ are the numbers of edges and nodes in a tetrahedron element, respectively, and since linear interpolation functions are used, these numbers are 6 and 4 for each tetrahedron. By ignoring the surface integrals and using the basis functions for the weighting functions, Equations 3.49 and 3.51 can be written as:

$$\begin{aligned} &\sum_{j=1}^{N_{edges}} \tilde{A}_j \int_V (\nabla \times \mathbf{N}_i) \cdot (\nabla \times \mathbf{N}_j) dV + i\omega\mu_0 \sum_{j=1}^{N_{edges}} \tilde{A}_j \int_V \sigma \mathbf{N}_i \cdot \mathbf{N}_j dV + \\ &\mu_0 \sum_{k=1}^{N_{nodes}} \tilde{\phi}_k \int_V \sigma N_i \cdot \nabla N_k dV = \mu_0 \left( \int_V N_i \cdot \mathbf{J}_e^s dV + \int_V N_i \cdot \nabla \times \mathbf{M} dV \right) \end{aligned} \tag{3.54}$$

$$\begin{aligned} i\omega \sum_{j=1}^{N_{edges}} \tilde{A}_j \int_V \nabla N_l \cdot (\sigma N_j) dV + \sum_{k=1}^{N_{nodes}} \tilde{\phi}_k \int_V \nabla N_l \cdot (\sigma N_k) dV \\ = -\int_V N_l \nabla \cdot \mathbf{J}_e^s dV \end{aligned} \tag{3.55}$$

where $i=1,\ldots,N_{edges}$ and $l=1,\ldots,N_{nodes}$, and $N_{edges}$ and $N_{nodes}$ are the total numbers of edges and nodes, respectively, in the volume. The equations are solved for the approximate vector potential ( $\tilde{\mathbf{A}}$ ) and scalar potential ( $\tilde{\phi}$ ).

### 3.4.5 Solution of the discrete system

The left-hand sides of Equations 3.54 and 3.55 contain node-based and edge-elements basis functions and the scalar and vector potentials to be determined. The right-hand sides of these equations contain interactions between the basis function and sources. Before solving the system of equations, Dirichlet boundary conditions are imposed. To force the condition, the elements of the coefficient matrix corresponding to nodes and edges on the problem boundaries are set to zero except the diagonal element (Jin, 2014). Further, the corresponding element in the source vector is set to zero in the equations. The matrix form of the system of equations is:

$$\begin{bmatrix} \mathbf{C}+\omega\mu_0\mathbf{D} & \mu_0\mathbf{F} \\ i\omega\mathbf{G} & \mathbf{H} \end{bmatrix} \begin{Bmatrix} \tilde{A} \\ \tilde{\phi} \end{Bmatrix} = \begin{Bmatrix} \mu_0\left(S_1+S_2\right) \\ S_3 \end{Bmatrix} \tag{3.56}$$

By separating the real and imaginary parts of the system of equations, the matrix form is given as:

$$\begin{bmatrix} \mathbf{C} & -\omega\mu_0\mathbf{D} & \mu_0\mathbf{F} & 0 \\ \omega\mu_0\mathbf{D} & \mathbf{C} & 0 & \mu_0\mathbf{F} \\ 0 & -\omega\mathbf{G} & \mathbf{H} & 0 \\ \omega\mathbf{G} & 0 & 0 & \mathbf{H} \end{bmatrix} \begin{Bmatrix} \tilde{A}^R \\ \tilde{A}^I \\ \tilde{\phi}^R \\ \tilde{\phi}^I \end{Bmatrix} = \begin{Bmatrix} \mu_0\left(S_1+S_2\right) \\ 0 \\ S_3 \\ 0 \end{Bmatrix} \tag{3.57}$$

where

$$C_{ij} = \int_V \left(\nabla\times\mathbf{N}_i\right)\cdot\left(\nabla\times\mathbf{N}_j\right)dV \tag{3.58}$$

$$D_{ij} = \int_V \sigma\mathbf{N}_i\cdot\mathbf{N}_j dV \tag{3.59}$$

$$F_{il} = \int_V \nabla N_l \cdot \left(\sigma N_j\right) dV \tag{3.60}$$

$$H_{lk} = \int_V \nabla N_l \cdot \left(\sigma N_k\right) dV \tag{3.61}$$

**G** is the transpose of the matrix **F**, the subscripts $i$ and $j$ are 1,…,$N_{edges}$, and the subscripts $l$ and $k$ are 1,…, $N_{nodes}$,

$$S_1 = \int_V \mathbf{N}_i \cdot \mathbf{J}_e^s dV \tag{3.62}$$

$$S_2 = \int_V \mathbf{N}_i \cdot \nabla \times \mathbf{M} dV \tag{3.63}$$

$$S_3 = -\int_V N_l \nabla \cdot \mathbf{J}_e^s dV \tag{3.64}$$

$\tilde{A}^R$, $\tilde{A}^I$, $\tilde{\phi}^R$ and $\tilde{\phi}^I$ are the real and imaginary parts of the coefficients.

When the grounded wire is used as a source, the contribution from the magnetic current ($S_2$) would be zero. The other sources ($S_1$ and $S_3$) are the same. Therefore, the system of equations (Equation 3.56) can be written as:

$$\begin{bmatrix} \mathbf{C} + \omega\mu_0\mathbf{D} & \mu_0\mathbf{F} \\ i\omega\mathbf{G} & \mathbf{H} \end{bmatrix} \begin{Bmatrix} \tilde{A} \\ \tilde{\phi} \end{Bmatrix} = \begin{Bmatrix} \mu_0 S_1 \\ S_3 \end{Bmatrix} \tag{3.65}$$

An infinitesimal magnetic dipole can be represented by a point source, and in this case, the contributions of other two sources ($S_1$ and $S_3$) would be zero; therefore, the system of equations (Equation 3.56) can be written as:

$$\begin{bmatrix} \mathbf{C}+\omega\mu_0\mathbf{D} & \mu_0\mathbf{F} \\ i\omega\mathbf{G} & \mathbf{H} \end{bmatrix} \begin{Bmatrix} \tilde{A} \\ \tilde{\phi} \end{Bmatrix} = \begin{Bmatrix} \mu_0 S_2 \\ 0 \end{Bmatrix} \tag{3.66}$$

The system of equations is constructed by using the developed forward modelling code and solved by using the direct solver MUMPS. Once the system of equations (Equation 3.64 or 3.65) is solved, the electric field is calculated with Equation 3.21. The magnetic field is calculated by taking the curl of the vector interpolation functions and using the vector potential ( $\tilde{\mathbf{A}}$ ):

$$\mathbf{H} = \frac{1}{\mu_0} \sum_{j=1}^{N_{edges}} \tilde{A}_j \nabla \times N_j \tag{3.67}$$

# Chapter 4

# Forward-Modelling Examples

## 4.1 Introduction

In this chapter, the accuracy of the developed code is shown with a number of examples. In the first two examples, the FE results that are obtained by using magnetic and electric sources in homogeneous whole-space and half-space are compared with the analytic solutions. The other three examples are more realistic models that are found in the literature, and the FE results obtained in this study are compared with other numerical solutions such as the finite-volume (FV) method and the integral-equation (IE) solution. In the last example, the real-life situation which includes topography and an arbitrarily shaped ore body is modelled. Also, the effect of the mesh quality on the accuracy of the FE results and the resource usage are given in this chapter.

## 4.2 A magnetic point source

For this verification example, an infinitesimal z-directed magnetic dipole represented by a point source is considered. The location of the magnetic dipole is at the center of the conductive wholespace of 0.01 S/m, and its dipole moment is equal to unity. Figure 4.1 shows the side view of the model. In the figure, the magnetic point source is denoted by the black dot; the observation points along the x-axis with 200 m spacing from -6 km to 6 km are shown by the blue dots. The dimension of the

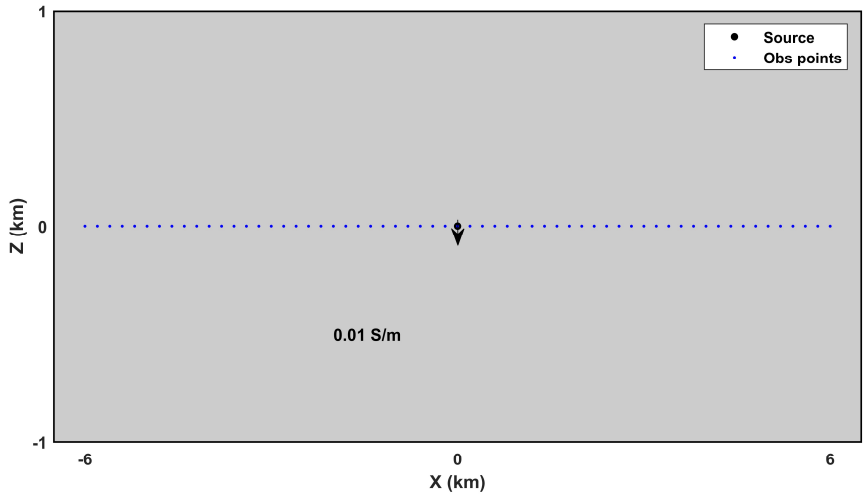


Figure 4.1 The side view of the conductive whole-space for the z-directed magnetic dipole with 1 A/m dipole moment

problem region is 50 km from -25 km to 25 km for all three directions. The region was tetrahedralized by using TetGen (Si, 2007) and locally refined at the source and observation locations by inserting additional nodes to increase the accuracy of the solution (Figure 4.2 and 4.3). Further, as mentioned in Section 3.4.1, the quality of the tetrahedral elements affects the accuracy of the solutions. Therefore, to avoid bad quality tetrahedrons that have narrow inner angles, the parameters maximum radius-edge ratio and minimum dihedral angles (the definitions of these constraints are given in Section 4.8) were chosen carefully, taking into account the limited computer memory. To reduce the total number of tetrahedral elements in the region, the size of the tetrahedrons is increased towards the boundaries by defining the volume constraints. Therefore, choosing the computational area bigger than necessary affects the number of tetrahedral elements slightly; however, this guarantees the boundaries are sufficiently far away from the source. The number of elements, nodes, and edges

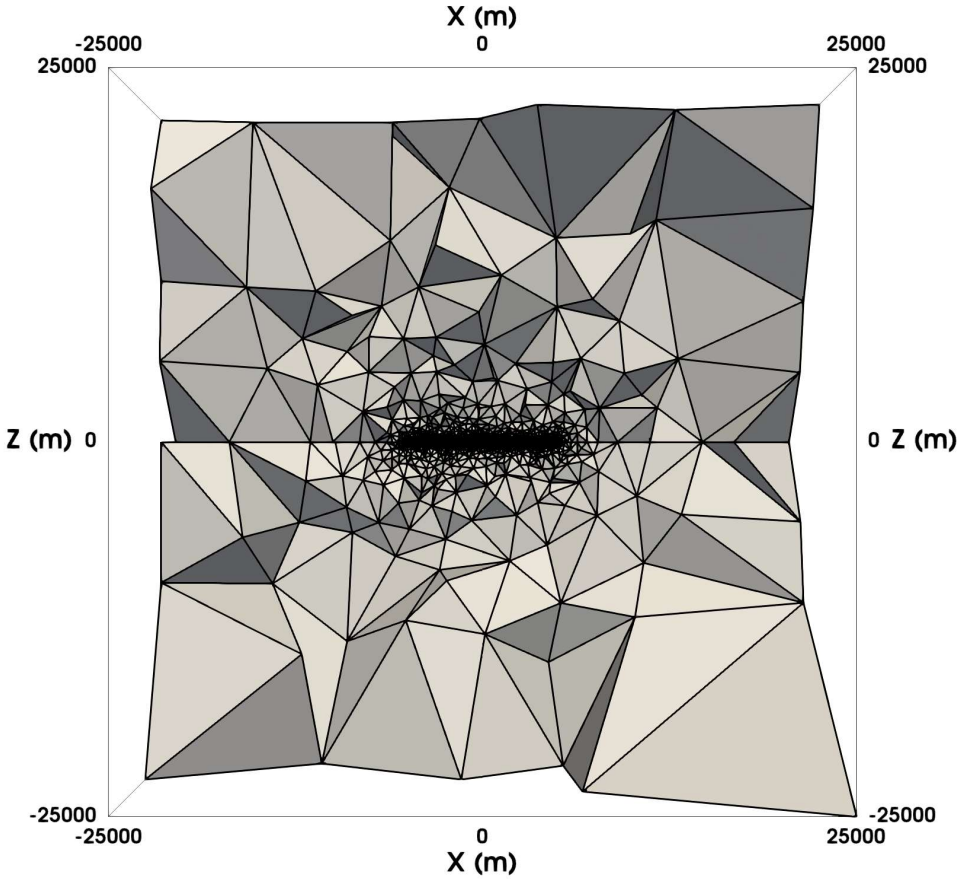


Figure 4.2 The xz-section of the mesh for the conductive whole-space model.

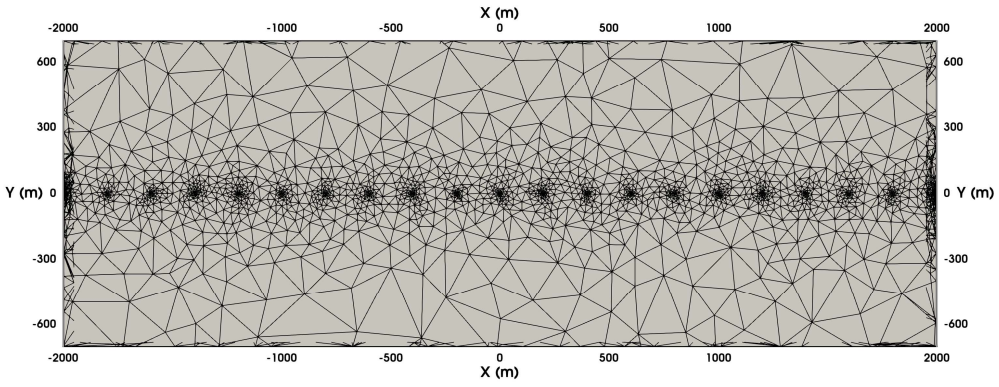


Figure 4.3 An enlarged xy-section of the mesh from the center of the model.

for this example were 132110, 21607, and 153877, respectively, and this resulted in 350968 unknowns. To solve the linear system, the parallel version of MUMPS was

used with the LU factorization option, which is for unsymmetric matrices, and the computation was done on a laptop having an Intel I7-9750H processor and 40 GB memory. The total runtime was about 90 seconds, and the total memory usage was about 4 GB for this example. Figure 4.4 shows the component of the total magnetic field at the observation points for 3 Hz. The result obtained by the **A**-$\phi$ finite-element approach is compared against the analytic equation given by Ward and Hohmann (1988). In the figure, the blue circles show the **A**-$\phi$ result, and the black lines show the analytic result. It can be seen that there is a good agreement between the analytical and **A**-$\phi$ results. The relative errors are 0.002 for the real part, 0.04 for the imaginary part ( RE=$\left\|E^{An}-E^{FE}\right\|/\left\|E^{An}\right\|$).

### 4.3 Conductive half-space and electric dipole

In this example, a tiny length electric dipole source is considered on the Earth's surface. The Earth's surface is excited by the source terms $S_2$ (Equation 3.63) and $S_3$ (Equation 3.64), and the system of equations that is given in Equation 3.65 is solved to obtain the potentials. The closed-forms of the source terms are given in Appendix A. The conductivity of the homogeneous half-space and air are 0.01 S/m and $10^{-8}$ S/m, respectively (see Figure 4.5). In the figure, the solid red line shows the source location, and the blue dots denote the observation locations. 1 A current runs through the 10 m wire extending from -5 m to 5 m in the x-direction. The dimension of the problem region is 50 km from -25 km to 25 km for the three directions. The observation points extend along the x-direction spaced by 200 m from -6 km to 6 km. Around observation locations the mesh was locally refined by inserting additional tetrahedrons whose size is 4 m for the accuracy of the solution, and the sizes of the

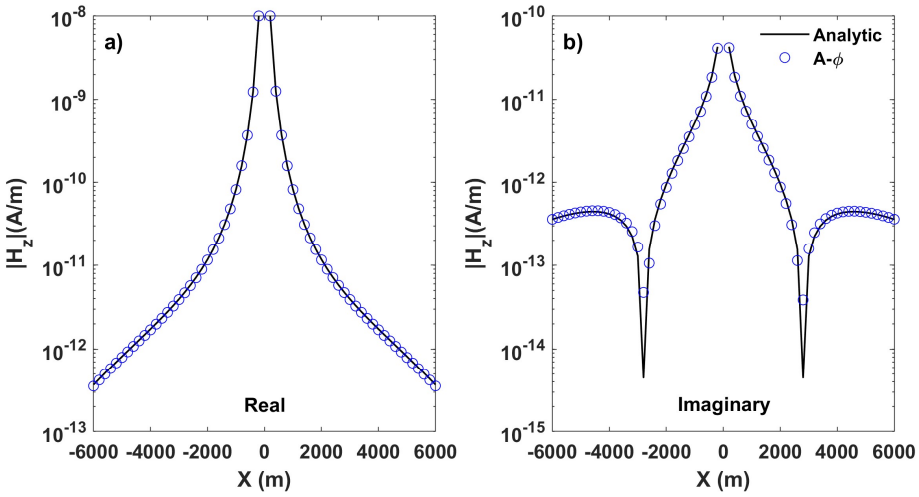


Figure 4.4 A comparison of the z-component of the magnetic field for 3 Hz for the whole-space example.

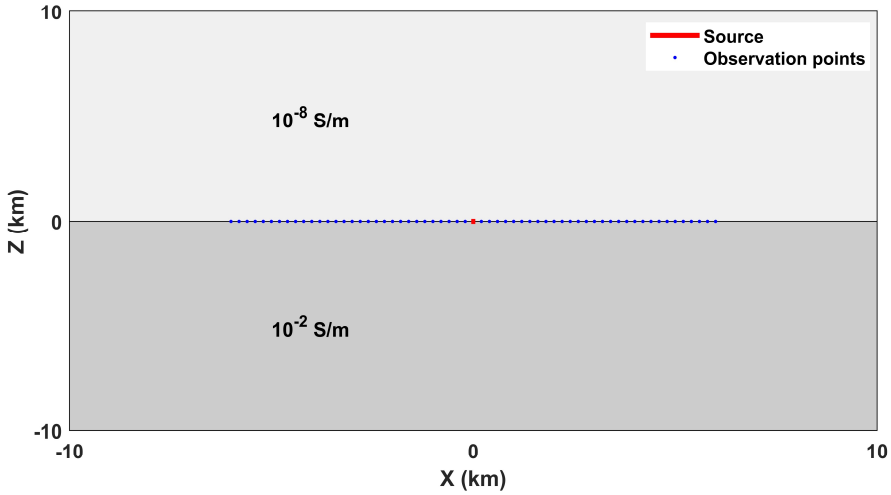


Figure 4.5 The side view of the homogeneous half-space example.

tetrahedral elements were gradually increased towards the boundaries (Figure 4.6 and 4.7). The number of elements, nodes, and edges for this example were 287836, 47257, and 335691, respectively; this resulted in 765896 unknowns, and the number of nodes and edges on the boundaries, for this example, were 595 and 1957, respectively. The system of equations was solved by the parallel version of MUMPS. The total run time

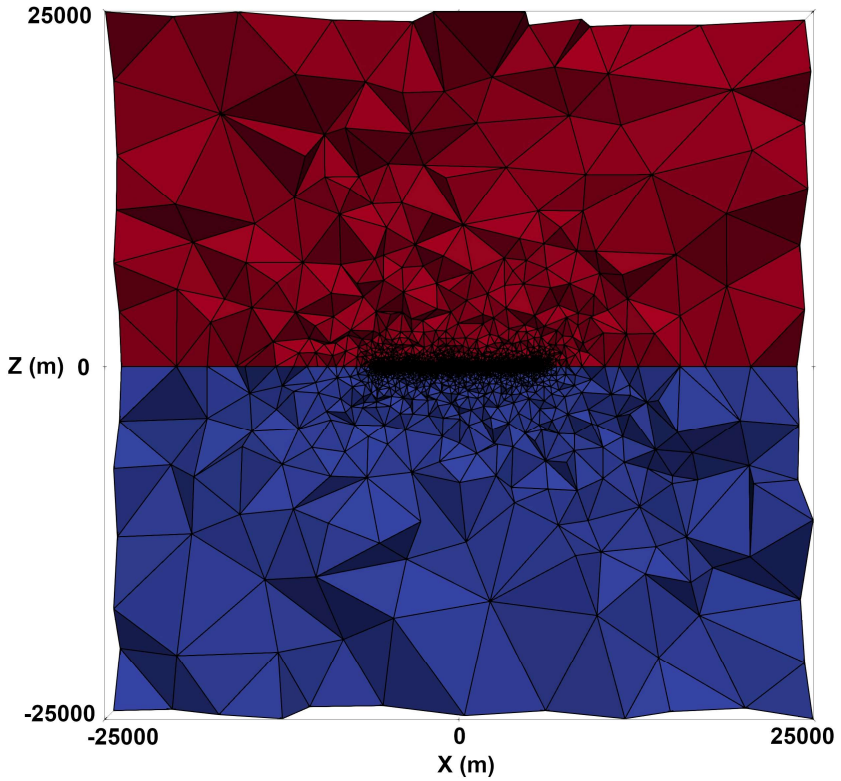


Figure 4.6 The xz-section of the mesh for the homogeneous half-space model for the electric dipole source.

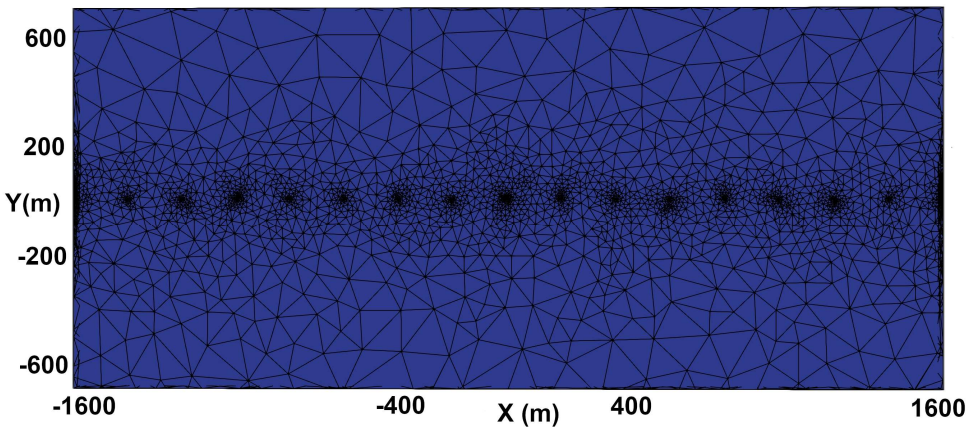


Figure 4.7 An enlarged xy-section of the homogeneous half-space example

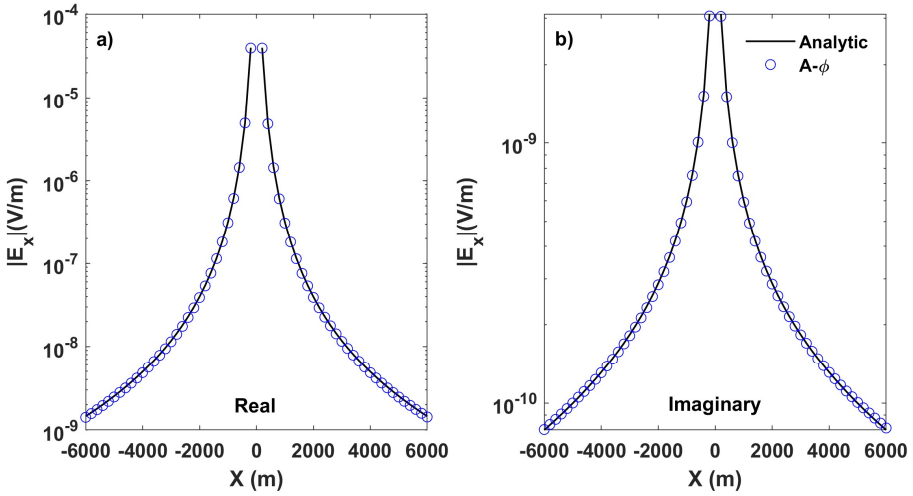


Figure 4.8 The real and imaginary parts of $E_x$ for the homogeneous half-space example for a frequency of 0.1 Hz.

was about 7 minutes, and the memory usage about 11.5 GB. Figure 4.8 shows the x-component of the electric field for the frequency of 0.1 Hz. The result obtained from the vector and scalar potential formulation was compared with the analytic solution given by Ward and Hohmann (1998). It can be said that there is a good agreement between **A**-$\phi$ and analytical results. The fit between **A**-$\phi$ and analytical solutions is 98 percent for the real part and 99 percent for the imaginary part.

## 4.4 Conductive half-space with a block

This example represents a geophysical scenario that uses an x-directed long grounded wire whose length is 100 m starting at the center of the computational domain. In this model, there is a buried conductive block (0.2 S/m) with dimension 120×200×400 m in a conductive half-space of 0.02 S/m with its center at 1000, 0 and -300 m in the x-, y- and z-directions, respectively, from the Earth's surface.

The model is depicted in Figure 4.9. In the figure, the solid red line denotes the grounded wire; the blue dots show the observation points starting at 400 m and ending

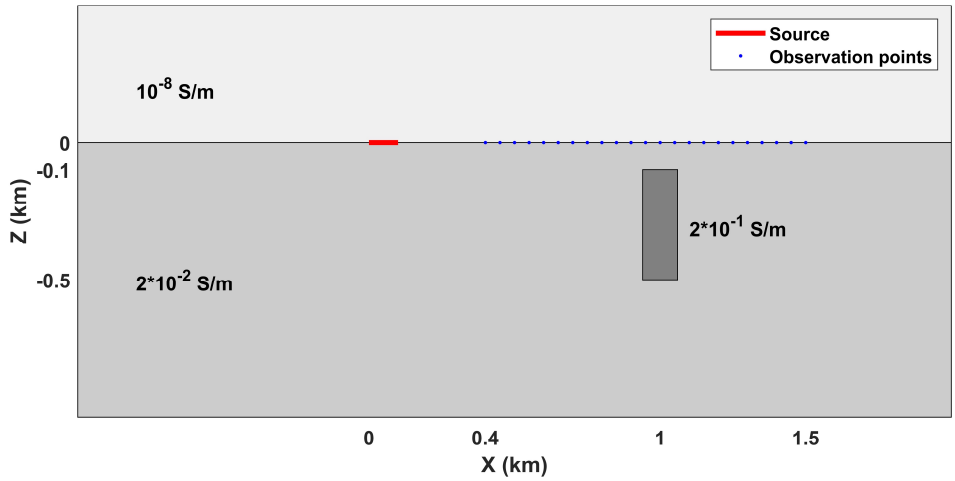


Figure 4.9 The xz-section of the plan view of the conductive block example in a half-space.

at 1500 m along the x-direction. The source and observation locations were refined by adding tetrahedrons of 5 m size to improve the accuracy of the solution. Thus, the 100 m long wire was divided into 54 segments. In the model, finer tetrahedrons were used by setting the maximum volume of the tetrahedrons inside of the conductive block equal to 800 $m^3$ to represent the conductive block correctly. The total region, whose dimension is 40 km for each of the three directions, consists of 221496 elements, 37630 nodes, and 263903 edges with 4778 nodes and 14897 edges lying on the boundaries. An enlarged cross-section of the mesh is given in Figure 4.10.

The system of equations is the same as Equation 3.65, and it was solved by using the parallel version of MUMPS with the LU factorization option. The total run time was about 6.5 minutes, and the memory usage was about 9.4 GB. The FE result was verified with the IE solution given by Farquharson and Oldenburg (2002) and the FV solution given by Jahandari and Farquharson (2015). The relative errors are given for the secondary electric field. The comparison is given in Figure 4.11. Panel a in the figure shows the homogeneous half-space response of the model, and panel b shows

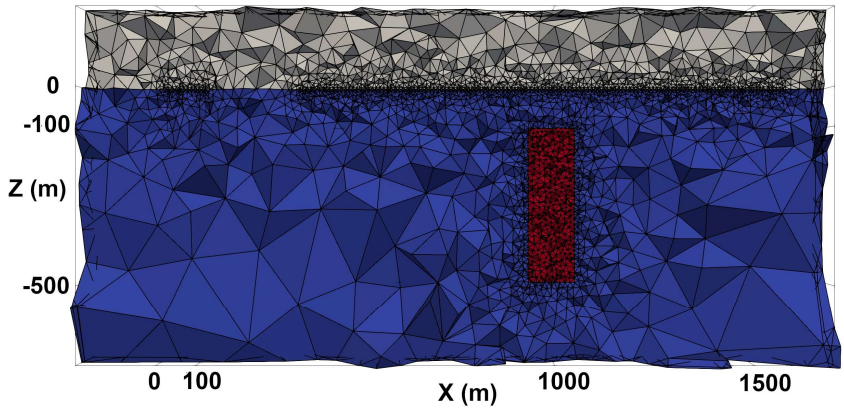


Figure 4.10 An enlarged xz-section of the tetrahedral mesh for the conductive block example.

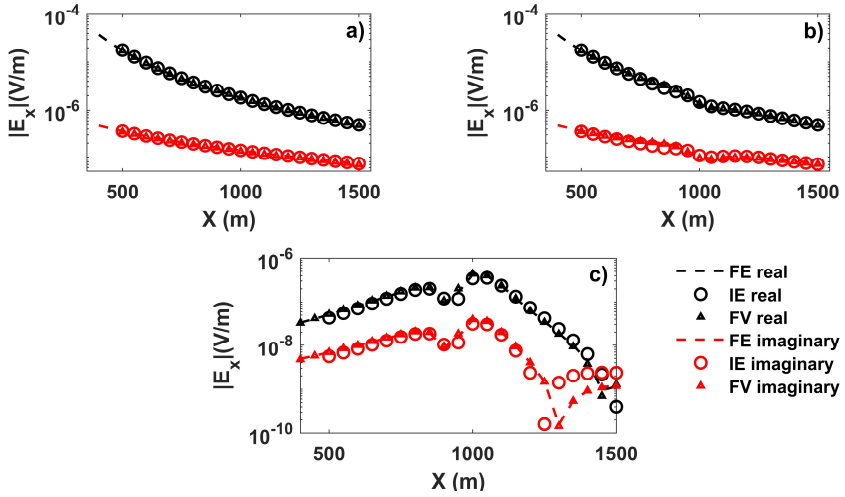


Figure 4.11 The comparison of the FE result with the IE and the FV solutions for the example shown on Figure 4.9 and 4.10. The IE and FV results are given, respectively, by Farquharson and Oldenburg (2002) and Jahandari and Farquharson (2014).

the half-space response with the block. The differences between the homogeneous half-space response and half-space response with the block give the secondary field which is shown in Figure 4.11c. The relative error between the IE and FE solutions is 0.15 for the real part and 0.20 for the imaginary part. For the FV method, the relative error is 0.07 for the real part and 0.05 for the imaginary part. It can be said that there is a good match with the other two numerical methods. However, it can be said that

the points at the end of the profile cause relative errors to increase between the FE and the IE solutions. The reason for the inconsistency at these points is probably due to the crude discretization of the conductive block (5×5×5 blocks) used for the IE solution (see Farquharson and Oldenburg, 2002, for details).

### 4.5 CSAMT-like measurement with a conductive block

In this scenario, a grounded electric wire whose length is 1000 m extending along the x-direction from -500 m to 500 m on the flat Earth's surface was used with a dipole moment of 40,000 Am. The conductivity of the buried block is 1 S/m in a homogeneous half-space of 0.01 S/m. The dimension of the block is 1000×1000×300 m in the x-, y-, and z-directions, respectively, and its center is at the point 0, -8500, and -550 m. The observation points lie on the Earth's surface and extend from -10 km to 10 km with a spacing of 100 m in the x- and y-directions; this results in more than 400 observation points. The computational domain of 40 km for each direction was divided into tetrahedral elements. The source and observation locations were locally refined by inserting tetrahedrons of 10 m size (Figure 4.12). For the block, finer tetrahedrons were used by equating the maximum volume of the tetrahedrons in the block to 30000 $m^3$. The 1 km of the grounded wire was represented with 228 segments. The entire domain consists of 769596 elements, 125010 nodes, and 895416 edges.

The linear system was solved by using MUMPS on a workstation having an Intel Xeon E5-2630v4 processor and 32 GB memory. The total run time and memory

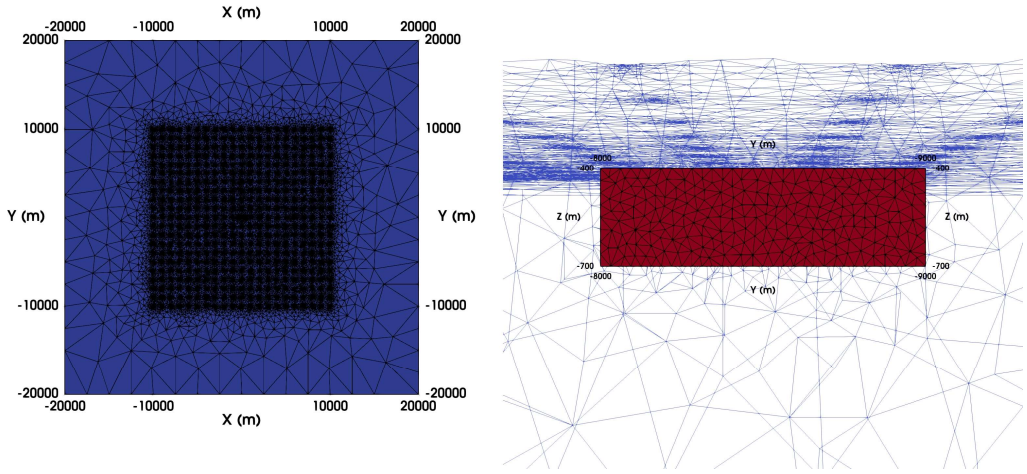


Figure 4.12 The left panel shows the xy-section of the flat Earth's surface and observation points extending from -10 km to 10 km. The right panel shows the yz-section of the block in the mesh.

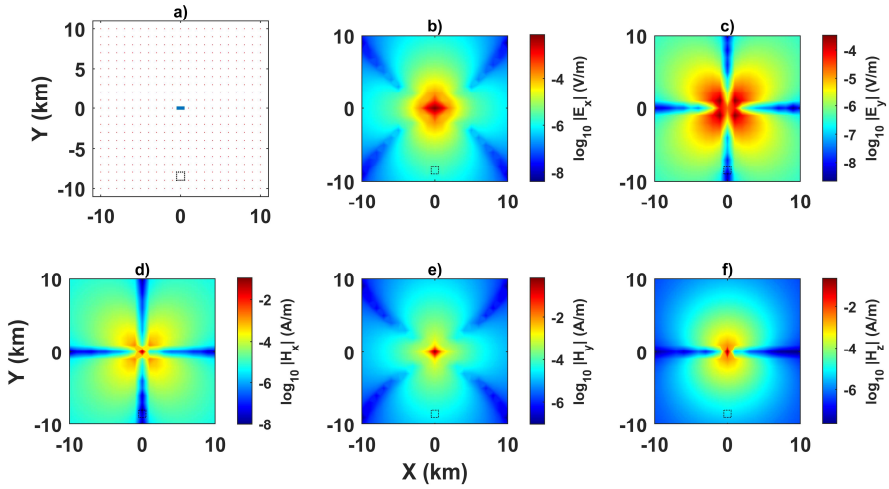


Figure 4.13 The plan view of the model, and, for a frequency of 10 Hz, the contour maps of the EM fields. a) The red dots are observation points; the solid blue line is the source location, and the dotted square is the location of the block. b-c) Electric field components. d-f) Magnetic field components.

usages were about 22 minutes and 28 GB for this example. The result obtained from the FE potential approach was verified through comparison with the result given by Zhang et al. (2020). Zhang et al. solved the same geophysical scenario by using COMSOL software, which is general-purpose software for modelling, design, etc. For the comparison, the behavior of the electromagnetic fields is shown as contour maps

for the components $E_x$, $E_y$, $H_x$, $H_y$, and $H_z$ (Figure 4.13). In Figure 4.13a, the red dots denote observation points; the blue line represents the grounded wire, and the dotted black line shows the buried block. Figure 4.13b-c show the contour maps of the x- and y-components of the electric fields. The contour maps of the magnetic field components are given in Figure 4.13d-f. The color scale of the maps fits the given maps by Zhang et al. (2020). The clear anomaly can be seen in the x-component of the electric field and the vertical component of the magnetic field. Further, the shape of the block is well defined in the x-component of the electric field.

### 4.6 A layered Earth model

In this geophysical scenario, a layered Earth model is considered by using two y-directed long grounded wires of 2 km on the flat Earth's surface. The purpose of this scenario is to simulate the oil and geothermal reservoirs that can occur over volcanic bedrock. Typically, in this type of reservoir, a thick conductive layer that is rich in clay minerals settles over a resistive basement, and the conductive layer decreases the permeability of the fluids; therefore, the layer acts as a trap for oil and geothermal water (Mitsuhata et al., 2002; Mitsuhata et al., 1999). For this purpose, the vertical component of the magnetic field is calculated for two sources for the frequencies of 0.3 and 3 Hz at 12 points that start at -3 km and end at 9 km along the x-axis. The plan view is depicted in Figure 4.14. The FE result is verified through comparison with the 2.5-D FE solution of Mitsuhata et al. (2002).

In the 3D model, the layers were extended up to boundaries, and the dimension of the region is 40 km for each direction. The problem region was subdivided into a tetrahedral grid giving 329932 elements, 54945 nodes, and 387608 edges. The parts

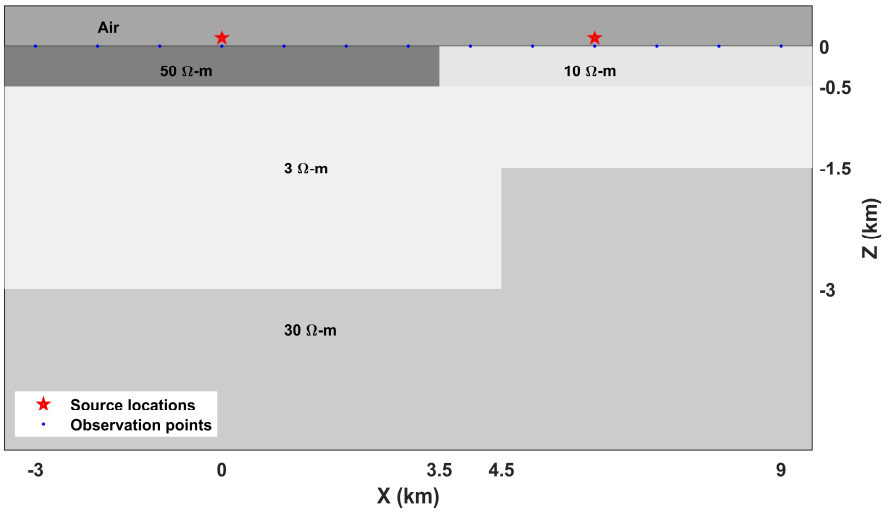


Figure 4.14 A side view of the layered Earth model. The blue dots are observation points, and the stars denote the y-directed sources of 2 km.

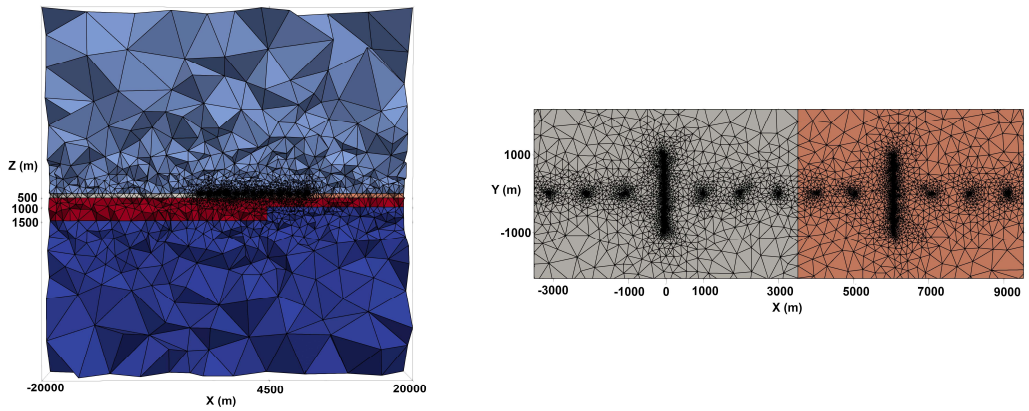


Figure 4.15 Unstructured tetrahedral mesh of the model: Left panel shows the xz-section of the mesh, right panel shows the refined observation points and source locations in the xy-section.

of the mesh around the source locations and observation points were locally refined by adding tetrahedrons of 10 m size (Figure 4.15). The first source (at x=0 km) and second source (at x=6 km) pass through 585 and 574 elements, respectively. The current in the wires is unity; hence, the electric dipole moment of the wires equals 2000 Am.

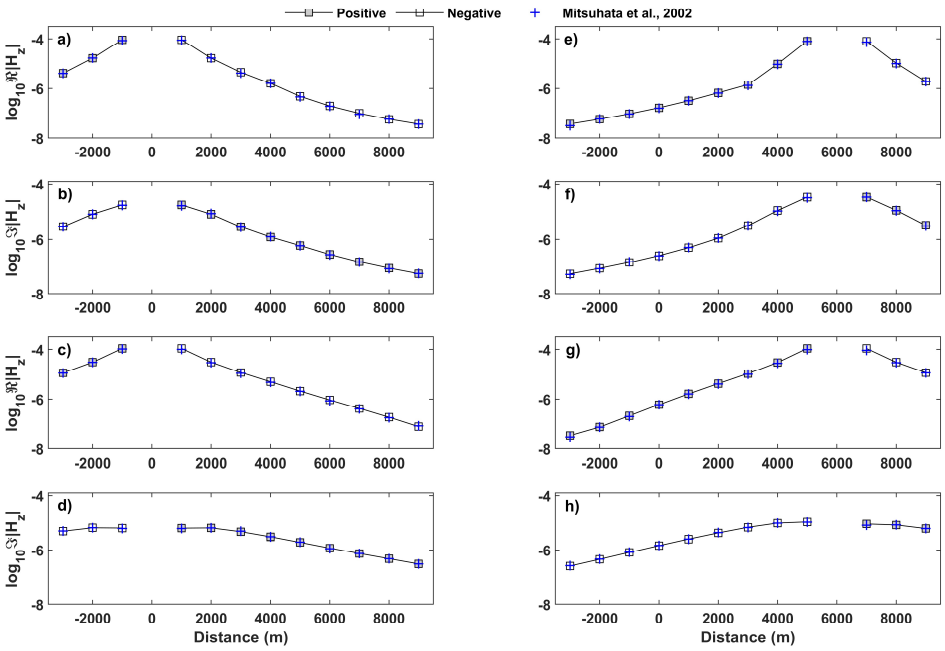


Figure 4.16 The data calculated from the layered Earth model shown in Figure 4.14. The left panels show the data that are generated by the first source (x=0 km) for frequencies of 3 (a-b) and 0.3 (c-d) Hz. The right panels show the data that are generated by the second source (x=6 km) for the frequencies of 3 (e-f) and 0.3 (g-h) Hz.

The system of equations was solved with MUMPS. The total run time and total memory usage were about 25 minutes and 17.8 GB. The left-hand side matrix in Equation 3.65 was factorized once for each frequency, and the factorized matrix was re-used for the first and second sources. Figure 4.16 shows the forward-modelling result for two frequencies of 0.3 and 3 Hz. It can be seen that the potential formulation result has a good match with the 2.5-D result of Mitsuhata et al. (2002). Because the slope of the primary field masks the effect on the data of the discontinuity and the uplift; at first glance, recognizing the discontinuity in the first layer and the uplift of the basement is difficult. However, it can be seen that in Figure 4.16e, that is, for the second source at the frequency of 3 Hz, the slope of the curve is different than the general incline in the positive side of the curve until 3 km. Therefore, it can be said

from the curves' character that the areas which are close to the source can be defined well and are most sensitive. The sensitivity decreases when the distance between source and observation points increases (Mitsuhata et al., 2002).

### 4.7 Realistic Ovoid model

This example represents a realistic model with a complex body and topography. The model used here was built by Jahandari (2015) considering gravity, helicopter EM, and drilling data which were obtained on a massive sulphide deposit at the region Voisey's Bay, Labrador, Canada. However, the model was rebuilt to make a synthetic dataset with a grounded electric wire source. The frame of the complex ore body, and the tetrahedralized surface are shown in Figure 4.17. It can be seen that unstructured tetrahedral grids reflect the topography and complex body accurately. A 1A current was considered in the 500 m long x-directed grounded electric wire, and the EM fields were calculated at 31 points on a profile. The observation and source locations of the mesh were refined by adding tetrahedrons of 5 m size. This resulted in 123008 elements, 19823 nodes, and 143111 edges. The frequency was 50 Hz for this example, and the conductivity of the half-space was chosen to be 0.001 S/m. However, several conductivity values were used for the ore body to show how the code works with large conductivity contrasts. Note that Jahandari (2015) found the conductivity value of the ore body to be 100 S/m with the trial-and-error forward-modelling approach applied to the helicopter EM data.

The system of equations was solved with MUMPS. The total run time was about 2.5 minutes, and the memory usage was about 6 GB. The x-component of the electric

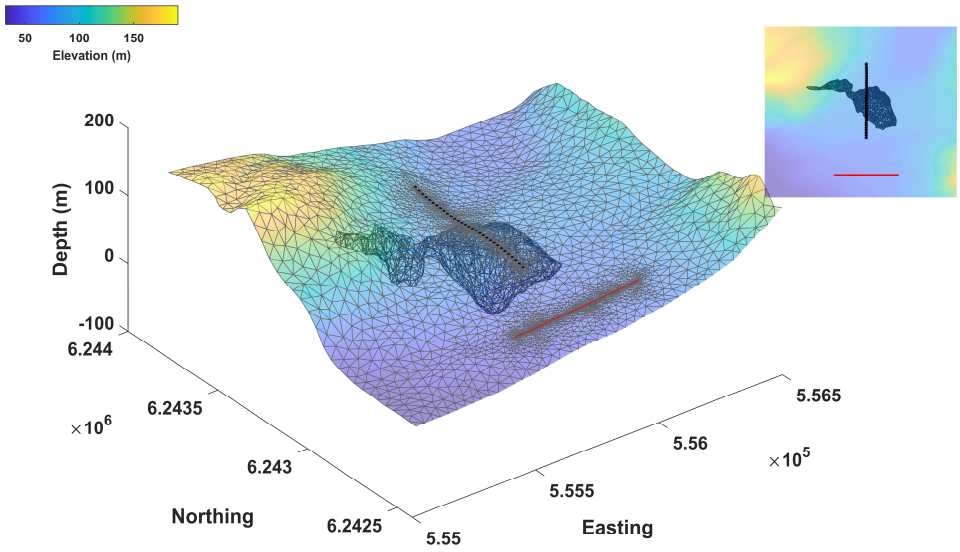


Figure 4.17 Surface mesh and ore body of the realistic model. The black dots show the observation locations, and the red line indicates the source location.

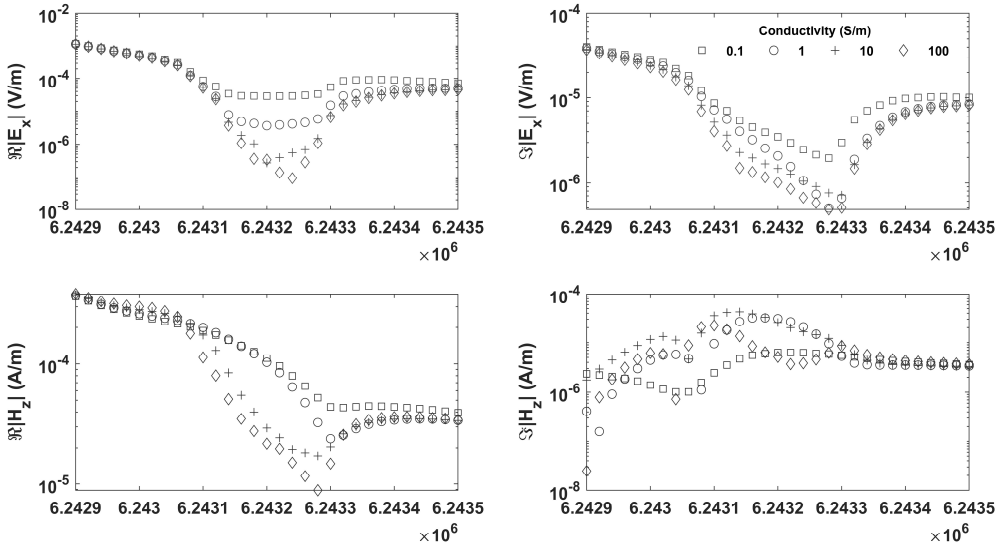


Figure 4.18 The data calculated from the realistic Ovoid body shown in Figure 4.17. The top two panels show the x-component of the electric field; the bottom two panels show the vertical component of the magnetic field. The right panels show the real parts of the electric and magnetic fields components, and the left panels show the imaginary parts of the components.

field and vertical component of the magnetic field are given in Figure 4.18. It can be seen that the responses are consistent for various conductivity contrasts.

## 4.8 Mesh quality and local refinement

The quality of the tetrahedral girds affects the accuracy of the numerical solutions, as mentioned in Section 3.4.1. Mesh qualities are controlled by a few constraints, which are maximum radius-edge ratio bound and minimum dihedral angle bound in TetGen (Si, 2015). The radius-edge ratio of tetrahedrons is defined as the ratio between the radius of its circumscribed ball and the length of the shortest edge. The default values, namely when the radius-edge constraint is not used, is 2, and high values of this constraint reduce the mesh quality. The second constraint, minimum dihedral angle, is defined as the angle between two faces, and small angles cause a reduction in mesh quality. Another significant factor that highly affects the accuracy of the numerical solutions is the size of the tetrahedrons used for the refinement of source and observation locations.

In this section, several tests were conducted to demonstrate the effect of the mesh quality and refinement, and resource usage was observed. For the tests, a homogeneous half-space model was used with the conductivity of 0.01 S/m. A 1A current was put through the 20 m wire extending from -10 m to 10 m in the x-direction. The frequency was 0.1 Hz. Observation sites were located from -6 km to 6 km with a spacing of 200 m. The numerical results were compared with the analytical solution that is given by Ward and Hohmann (1988). To generate tetrahedral grids of different qualities, maximum radius-edge ratio bound and minimum dihedral angle bound were used from 1.8 to 1.3 and from 4 to 18, respectively. Further, some tests were repeated by inserting additional tetrahedrons the size of 10 m and 5 m for the refinement of the observation locations. The minimum dihedral angle and the size of

Table 4.1 Effects of the maximum radius-edge ratio on FE results. The size of the tetrahedrons used for refinements was 10 m, and the minimum dihedral angle was 16 degrees.

| Cell Size | *R/L* | N. nodes | N. elements | N. edges | LU fac t (s) | Solution t (s) | Total t (s) | Memory usage for LU Fac. (MB) | Error (%) real/imag | |
|---|---|---|---|---|---|---|---|---|---|---|
| 10 m | **1.8** | 20058 | 114031 | 136785 | 49.6 | 0.56 | 73.8 | 3376 | 3.9 | 4.7 |
| | **1.6** | 23177 | 133329 | 159192 | 64.8 | 0.71 | 92.1 | 4199 | 10.6 | 5.9 |
| | **1.4** | 37515 | 222012 | 262237 | 194.4 | 1.4 | 237.4 | 8983 | 1.4 | 2.0 |
| | **1.3** | 59124 | 355582 | 417486 | 524.6 | 3.3 | 595.3 | 17813 | 3.4 | 6.0 |

Table 4.2 Effects of the maximum radius-edge ratio on FE results. The size of the tetrahedrons used for refinements was 5 m, and the minimum dihedral angle was 16 degrees.

| Cell size | *R/L* | N. nodes | N. elements | N. edges | LU fac. t (s) | Solution t (s) | Total t (s) | Memory usage for LU Fac. (MB) | Error (%) real/imag | |
|---|---|---|---|---|---|---|---|---|---|---|
| 5 m | **1.8** | 23817 | 136582 | 163078 | 60.4 | 0.67 | 86.2 | 4122 | 2.3 | 3.5 |
| | **1.6** | 30084 | 175199 | 207974 | 92.8 | 0.96 | 127.2 | 5796 | 5.2 | 2.1 |
| | **1.4** | 48729 | 290655 | 342101 | 254.3 | 2.1 | 307.8 | 11704 | 2.2 | 3.2 |
| | **1.3** | 82838 | 501576 | 587195 | 769.5 | 4.8 | 866.2 | 25248 | 2.5 | 1.1 |

the additional tetrahedrons were 16 and 10 m, respectively, and the variable was the maximum radius-edge ratio for the first test (Table 4.1). In the second test, the size of the refinement grids was 5 m (Table 4.2). It can be seen from these tests that using a small radius-edge ratio does not always improve the numerical solution. On the other hand, using small size refinement cells mostly improves the accuracy of the solutions.

In the third test, the variable was the minimum dihedral angle; the mesh was generated by adding tetrahedrons the size of 5 m and using the maximum radius-edge ratio constraint of 1.4. The results are given in Table 4.3. The minimum error was

Table 4.3 Effects of the minimum dihedral angles on FE results. The size of the tetrahedrons used for refinements was 5 m, and the maximum radius-edge ratio was 1.4.

| Cell size | *D. ang* | N. nodes | N. elements | N. edges | LU fac t (s) | Solution t (s) | Total t (s) | Memory usage for LU Fac. (MB) | Error (%) real/imag | |
|---|---|---|---|---|---|---|---|---|---|---|
| 5 m | **4** | 21284 | 123811 | 147685 | 41.9 | 0.58 | 65.2 | 3347 | 3.8 | 4.6 |
| | **8** | 23270 | 136293 | 162164 | 49.1 | 0.63 | 75.1 | 3841 | 5.1 | 4.1 |
| | **12** | 28923 | 170421 | 201971 | 78.84 | 0.89 | 111.2 | 5371 | 3.5 | 2.8 |
| | **16** | 48729 | 290655 | 342101 | 254.3 | 2.1 | 307.8 | 11704 | 2.2 | 3.2 |
| | **18** | 103402 | 621936 | 727581 | 1371.4 | 99.48 | 1606 | 35388 | 2.3 | 0.8 |

obtained when the minimum dihedral angle of 18 was used. However, this mesh was highly dense and consumed the largest memory. To note that the computer memory (40 GB) was not enough to solve the model; therefore, the swap area that is the part of the storage was used, and the solution of the model took more time than expected. Mostly, the source of the errors is the closest observation points where EM fields change more rapidly. The observation points close to the source may be locally refined with the smaller size of tetrahedrons.

Even though today's computer systems support very large memory or big clusters are available for geophysical modelling, the limits of computers should be considered. These tests show that improving mesh quality brings more tetrahedrons, and hence more computation effort. Further, improvements do not directly reflect in errors. On the other hand, local refinements at observation and source locations demonstrate better results with a moderate number of cells (see Section 4.3). This allows only the area of interest to be refined rather than the entire domain. Also, some experiment

design methods, such as the Taguchi method (Yano et al., 2005), may be useful for statistical aspects for this test.

## 4.9 Conclusions

In this chapter, a number of three-dimensional forward-modelling examples were presented to verify the developed code for the CSMAT method by using the vector and scalar potentials decomposition. Vector and scalar basis functions were used respectively for the vector and scalar potentials. A grounded wire and a magnetic dipole were used as a source, and the three-dimensional domain was discretized into unstructured tetrahedral grids, which is one of the suitable options for arbitrary geological structures and topography and allows domains to be refined locally. The direct solver, MUMPS, was used to solve the linear system of equations of the forward modelling. MUMPS is efficient for the solution of the linear system because it allows the factorization of the coefficient matrix to be reused. This feature is particularly important for the CSAMT method because data acquisition can be made with more than one source, as mentioned in Section 2.2.

In the first two examples, the FE results were compared with the analytical solutions. The comparisons showed that there are good agreements between numerical results and analytical solutions. The other three verification examples involved comparisons with other numerical solutions from the literature such as the finite-volume method, the integral-equation solution, and the finite-element method (COMSOL); it can be said that there are good agreements for all comparisons. Also, the code was tested with a real-life example to show the suitability of the unstructured tetrahedral grids for the topography and ore body. This example showed that the grids can handle real

geological features easily. The forward-modelling responses were not compared with a verified code for this example. However, it can be said that the responses that are obtained from the realistic model are correct based on the agreement of the other given comparative examples. Also, the responses seem to be consistent for the different conductivity values for the amorphous body.

Further, the accuracy of the FE results was examined in terms of mesh quality and local refinement. It was found that although the discretization of domains with high-quality grids generally generates more accurate results, this results in more tetrahedral grids. Further, due to the use of the direct solver for the solution of the linear system, the vector and scalar potentials are less sensitive to the quality of the mesh; in other words, solutions are less sensitive to the conditioning of a problem (Jahandari 2015). Thus, it can be said that it is sufficient to use meshes of average quality with local refinement at observation and source locations.

# Chapter 5

# Inversion of the CSAMT Data

## 5.1 Introduction

In this chapter, the formulation of the minimum-structure inversion, which is one of the gradient-based methods, is derived. The minimum-structure inversion procedure generates a smooth model by combining the measure of the data misfit and the measure of the model structure. The Gauss-Newton (GN) method is used to minimize the objective function. The GN method linearizes the forward-modelling operator and is more efficient for the calculation of the Hessian matrix. However, the Jacobian matrix must be recalculated in each GN iteration. The linear system of the inversion is solved with the implementations of the preconditioned conjugate gradient (CG) and nonpreconditioned generalized minimal residual (GMRES) iterative methods. Hence, the basics of these iterative solvers are briefly discussed here. Also, these solvers do not require the Hessian matrix to be formed explicitly to solve the linear system of the inversion. Therefore, these solvers are memory-efficient for such dense systems.

## 5.2 Minimum-structure inversion

The minimum-structure inversion procedure aims to find the simplest and most robust model that reproduces the observed data by dividing the problem region into many fine cells, and keeping the locations and sizes of these cells constant during the inversion procedure, and finding the conductivity values in the cells. Therefore, the

inversion procedure is a highly under-determined inverse problem that achieves the goal by iteratively minimizing an objective function, $\phi$, that includes data misfit, $\phi_d$, and model structure, $\phi_m$, terms. The objective function is given as the following:

$$\phi^k = \phi_d^k + \lambda^k \phi_m^k \tag{5.1}$$

where the superscript $k$ denotes the $k^{\text{th}}$ GN iteration, and $\lambda$ is the trade-off or regularization parameter that controls the relative balance of the data misfit and model structure terms.

To determine appropriate values of the trade-off parameter, a few methods are available in the literature, such as L-curve criterion, cooling schedule, and using a fixed value (see Constable et al., 1987; Farquharson and Oldenburg, 2004). In this study, the cooling schedule, in which the trade-off parameter is initially chosen as a relatively large number and reduced by a fixed factor, $\lambda^k = \lambda^{k-1} c$, until the data misfit $\phi_d$ is smaller or equal to target misfit (the number of data), is used. This strategy ensures steady convergence to the target misfit.

The measure of data misfit is the sum-of-squares of the differences between the observed data ($\mathbf{d}_{obs}$) and calculated candidate data ($\mathbf{d}_{cal}$) (Equation 5.2):

$$\phi_d^k = \left\| \mathbf{W}_d \left( \mathbf{d}_{obs} - \mathbf{d}_{cal}^k \right) \right\|_2^2 \tag{5.2}$$

where $\| \cdot \|_2$ denotes $l_2$-norm, and $\mathbf{W}_d$ is a diagonal matrix whose elements are the reciprocals of the measurement uncertainties, given by:

$$diag\left(\mathbf{W}_d\right) = 1/\left|\mathbf{d}_{obs}\right| \cdot std(\mathbf{d}_{obs}) \tag{5.3}$$

where *std* indicates the standard deviations of the observed data. The contribution to the misfit measure of the large uncertainties will be small.

The measure of the model structure $\phi_m$ is the summation of the roughness $\phi_r$ and smallness $\phi_s$ measures:

$$\phi_m^k = \alpha_r \phi_r^k + \alpha_s \phi_s^k \tag{5.4}$$

where $\alpha_r$ and $\alpha_s$ are the constant scalars for the relative importance of the roughness and smallness terms. The measure of the roughness is given by:

$$\phi_r^k = \left\| \mathbf{W}_r \mathbf{m}^k \right\|_2^2 \tag{5.5}$$

where $\mathbf{W}_r$ is the first-order spatial finite difference (FD) matrix taking into account neighbor relations in the region of interest, and $\mathbf{m}^k$ is a vector that contains model parameters. The elements of the roughness matrix can be used as -1 and 1 (Günther et al., 2006); however, this can cause bias between neighbouring tetrahedron cells. Therefore, cell properties such as distance between the centroid of the neighbor cells, cell volumes, and face area can be used to avoid bias. An overview and more sophisticated methods to calculate the elements of the roughness matrix are given by Lelièvre and Farquharson (2013). In this study, cell properties are considered to construct the roughness matrix. Assume that $i^{\text{th}}$ tetrahedron is a central tetrahedron and $j^{\text{th}}$ tetrahedron is one of the four adjacent tetrahedrons of the $i^{\text{th}}$ tetrahedron. For each face, the values of the matrix $\mathbf{W}_r$ can be set as the following:

$$\mathbf{W}_{r(f,i)} = -\frac{r}{\sqrt{(V_c + V_n)/2}} \tag{5.6a}$$

$$\mathbf{W}_{r(f,j)} = \frac{r}{\sqrt{(V_c + V_n)/2}} \tag{5.6b}$$

where $r$ is the distance between the centroids of the two adjacent cells, and the denominator, in Equation 5.6, is the square root of the arithmetic mean of the volumes of the center ($V_c$) and neighbor ($V_n$) cells. Therefore, the roughness matrix $\mathbf{W}_r$ is a very sparse matrix that includes only 2 entries in each row, and its dimension is $\mathbf{W}_r \in R^{F \times M}$, where $F$ and $M$ are the number of common faces in the active part and the number of active cells, respectively. The measure of the smallness is given by the following equation:

$$\phi_s^k = \left\| \mathbf{W}_s \left( \mathbf{m}^k - \mathbf{m}^{ref} \right) \right\|_2^2 \tag{5.7}$$

where $\mathbf{W}_s$ is a diagonal matrix whose purpose is to weight the difference between the candidate model vector and reference model vector $\mathbf{m}^{ref}$.

The system of the linear equations for the GN method is derived by taking the derivative of the objective function $\phi$ with respect to the model perturbation $\delta\mathbf{m}$ and equating to zero:

$$\frac{\partial \phi^k}{\partial \delta \mathbf{m}^k} = 0 \tag{5.8}$$

$$\frac{\partial \phi_d^k}{\partial \delta \mathbf{m}^k} + \lambda^k \left( \alpha_r \frac{\partial \phi_r^k}{\partial \delta \mathbf{m}^k} + \alpha_s \frac{\partial \phi_s^k}{\partial \delta \mathbf{m}^k} \right) = 0 \tag{5.9}$$

where,

$$\frac{\partial \phi_d^k}{\partial \delta \mathbf{m}^k} = -2\mathbf{J}^{k-1^T}\mathbf{W}_d{}^T\mathbf{W}_d\left(\mathbf{d}_{obs} - \mathbf{d}_{cal}^{k-1} - \mathbf{J}^{k-1}\delta\mathbf{m}^k\right) \tag{5.10}$$

$$\frac{\partial \phi_r^k}{\partial \delta \mathbf{m}^k} = 2\mathbf{W}_r{}^T\mathbf{W}_r\left(\mathbf{m}^{k-1} + \delta\mathbf{m}^k\right) \tag{5.11}$$

$$\frac{\partial \phi_s^k}{\partial \delta \mathbf{m}^k} = 2\mathbf{W}_s{}^T\mathbf{W}_s\left(\mathbf{m}^{k-1} + \delta\mathbf{m}^k - \mathbf{m}^{ref}\right) \tag{5.12}$$

By substituting Equations 5.10-5.12 into Equation 5.9 and rearranging, Equation 5.13 is obtained:

$$\begin{aligned}\left[\mathbf{J}^{k-1^T}\mathbf{W}_d{}^T\mathbf{W}_d\mathbf{J}^{k-1} + \lambda^k\left(\alpha_r\mathbf{W}_r{}^T\mathbf{W}_r + \alpha_s\mathbf{W}_s{}^T\mathbf{W}_s\right)\right]\delta\mathbf{m}^k \\ = \mathbf{J}^{k-1^T}\mathbf{W}_d{}^T\mathbf{W}_d\left(\mathbf{d}_{obs} - \mathbf{d}_{cal}^{k-1}\right) \\ - \lambda^k\left(\alpha_r\mathbf{W}_r{}^T\mathbf{W}_r\mathbf{m}^{k-1} - \alpha_s\mathbf{W}_s{}^T\mathbf{W}_s\left(\mathbf{m}^{ref} - \mathbf{m}^{k-1}\right)\right)\end{aligned} \tag{5.13}$$

where the left-hand side is the approximation of the Hessian matrix ( $\mathbf{H} \in R^{M\times M}$ ) with the GN method, and the right-hand side is the gradient of the objective function $\phi$ (Farquharson, 2008). $\mathbf{J}$ is the Jacobian or sensitivity matrix, and its dimension is $\mathbf{J} \in R^{n\times M}$ , where $n$ is the number of data. The superscript $T$ denotes the transpose of the matrices. The Hessian matrix is a symmetric and positive definite matrix; therefore, the above system can be solved using iterative solvers such as GMRES and CG. The model update vector is calculated by solving the above system of equations, and the updated model vector $\mathbf{m}^k$ is given with Equation 5.15:

$$\delta\mathbf{m}^k = -\mathbf{H}^{-1}\mathbf{g} \tag{5.14}$$

$$\mathbf{m}^k = \mathbf{m}^{k-1} + \delta\mathbf{m}^k \tag{5.15}$$

The Hessian and Jacobian matrices are very dense matrices; thus, explicitly forming such matrices is an intensive and expensive task in terms of memory and time, especially for the 3D inverse problem because there are thousands of inversion parameters that must be determined. In the next sections, explicitly and implicitly forming of these matrices and solution of Equation (5.14) will be discussed.

## 5.3 Calculation of the Jacobian matrix

The Jacobian matrix must be calculated for each GN iteration to linearize the inverse problem. Traditionally, the matrix is calculated using the FD approach, e.g., using backward difference:

$$\mathbf{J}^k = \frac{\partial \mathbf{F}\left[\mathbf{m}^k\right]}{\partial \mathbf{m}^k} = \frac{\mathbf{F}\left[\mathbf{m}^k\right] - \mathbf{F}\left[\mathbf{m}^k - \Delta m\right]}{\Delta m} \tag{5.16}$$

where **F** is the forward model operator; it is the FE method in this study. $\Delta m$ is the model perturbation. One column of the Jacobian matrix is obtained by solving one forward-modelling solution. This means that for each GN iteration, $M$+1 forward-modelling solutions are required to explicitly construct the Jacobian matrix. Therefore, considering the number of model parameters $M$ for the 3-dimensional inverse problem, it is impractical to obtain the Jacobian matrix using the FD method. The other method is the use of forward modelling sensitivities. By using the linear system of equations of the forward modelling (Equation 3.32), the model response at the $k^{\text{th}}$ iteration is given by:

$$\mathbf{d}_{cal}^{k} = \mathbf{F}\left[\mathbf{m}^{k}\right] = \mathbf{Q}\mathcal{X} \tag{5.17}$$

where the matrix $\mathbf{Q}$ is a sparse matrix, $\mathbf{Q} \in R^{n \times N}$, to calculate the $\mathbf{E}$ and $\mathbf{H}$ fields at the observation locations from the potentials that are obtained solving the linear system of the forward modelling. This matrix is independent of the model parameters. By taking the derivative of Equation 5.17 with respect to the model parameters:

$$\mathbf{J}^{k} = \mathbf{Q}\frac{\partial \mathcal{X}}{\partial \mathbf{m}^{k}} \tag{5.18}$$

where,

$$\frac{\partial \mathcal{X}}{\partial \mathbf{m}^{k}} = -\mathcal{L}^{-1}\left(\frac{\partial \mathcal{L}}{\partial \mathbf{m}^{k}}\mathcal{X}\right) \tag{5.19}$$

By substituting Equation 5.19 into Equation 5.18, the Jacobian matrix can be expressed as the product of the three matrices:

$$\mathbf{J}^{k} = \mathbf{Q}\mathcal{L}^{-1}\mathbf{G} \tag{5.20}$$

where $\mathbf{G} \in R^{N \times M}$ and is given as the following:

$$\mathbf{G} = -\left\{\partial\mathcal{L}/\partial m_1\mathcal{X}, \partial\mathcal{L}/\partial m_2\mathcal{X}, ..., \partial\mathcal{L}/\partial m_M\mathcal{X}\right\} \tag{5.21}$$

Note that if the secondary-field approach is used for the forward modelling, the source terms in the forward-modelling operator are not independent of model parameters; therefore, these terms should be considered for the calculation of the sensitivities.

The transpose of the Jacobian matrix can be written by rearranging Equation 5.20:

$$\mathbf{J}^{k^T} = \mathbf{G}^T \left[ \mathcal{L}^T \right]^{-1} \mathbf{Q}^T \tag{5.22}$$

Considering Equation 5.20, *M* pseudo-forward modellings are required to construct the Jacobian matrix; however, Equation 5.22 requires *n* pseudo forward modellings (Newman and Hoversten, 2000; Rodi and Mackie, 2001; Newman and Boggs, 2004; Siripunvaraporn, 2012). Therefore, using Equation 5.22 is more computationally efficient. Nonetheless, explicitly forming such a dense matrix consumes very large amounts of memory, and it is not necessary when any iterative solvers that belong to the Krylov subspace family are used. These solvers only need the products of the Hessian matrix with a vector to solve linear systems of the inverse problem.

The vector product of the Jacobian and its transpose are given by the following equation:

$$\mathbf{J}^k \mathbf{p} = \mathbf{Q} \mathcal{L}^{-1} \mathbf{G} \mathbf{p} \tag{5.23}$$

$$\mathbf{J}^{k^T} \mathbf{q} = \mathbf{G}^T \mathcal{L}^{T^{-1}} \mathbf{Q}^T \mathbf{q} \tag{5.24}$$

where **p** and **q** are arbitrary vectors, and two pseudo-forward modelling are required for the calculation of these products of the Jacobian matrix and its transpose with a vector (Newman and Hoversten, 2000; Rodi and Mackie, 2001). In the next section, the basics of the conjugate gradient method shall be demonstrated.

## 5.4 Preconditioned conjugate gradient method

The conjugate gradient (CG) method is one of the favorite methods in inverse problems, and it has proven itself. Although other iterative solvers such as MINRES and GMRES are more stable than the CG solver (Saad and Schultz, 1986; Jahandari

and Farquharson, 2017), the CG method has been preferred due to its simple implementation and that it has been adapted for both linear and nonlinear problems. The CG method requires a symmetric and positive definite matrix. Assume the linear system as follows:

$$\mathbf{A}\mathbf{x} = \mathbf{b} \tag{5.25}$$

where **A** is a square, symmetric, and positive definite matrix, and **x** and **b** are the vectors. Equivalently, Equation 5.25 can be expressed as the following:

$$\min \phi(\mathbf{x}) = \frac{1}{2}\mathbf{x}^T \mathbf{A}\mathbf{x} - \mathbf{b}\mathbf{x} \tag{5.26}$$

This equivalence allows the CG method to be used as a solver for linear systems and as a technique for minimization problems (Nocedal and Wright, 1999). For a particular vector $\mathbf{x}_k$, the residual $\mathbf{r}_k$ can be written as the following:

$$\mathbf{r}_k = \mathbf{b} - \mathbf{A}\mathbf{x}_k \tag{5.27}$$

The CG method can generate a set of vectors $\mathbf{p}_k$ with a property known as conjugacy in a very computationally efficient way and can compute a new vector by using only the previous vector $\mathbf{p}_{k\text{-}1}$, which means that the method requires little memory. The sequence of the $\mathbf{x}_k$ is given by the following equation:

$$\mathbf{x}_{k+1} = \mathbf{x}_k + \alpha_k \mathbf{A}\mathbf{p}_k \tag{5.28}$$

where

$$\alpha_k = \frac{\mathbf{r}_k^T \mathbf{y}_k}{\mathbf{p}_k^T \mathbf{A} \mathbf{p}_k} \tag{5.29}$$

where the vector $\mathbf{y}_k$ is the solution of a preconditioned linear system. The sequence of the residual is calculated by the following equation:

$$\mathbf{r}_{k+1} = \mathbf{r}_k - \alpha_k \mathbf{A} \mathbf{p}_k \tag{5.30}$$

The conjugate direction $\mathbf{p}_{k+1}$ is calculated with a linear combination of the solution of the reduced system and the previous direction $\mathbf{p}_k$:

$$\mathbf{p}_{k+1} = \mathbf{y}_{k+1} + \beta_{k+1} \mathbf{p}_k \tag{5.31}$$

where the scalar is to be determined by the following equation:

$$\beta_{k+1} = \frac{\mathbf{r}_{k+1}^T \mathbf{y}_{k+1}}{\mathbf{r}_k^T \mathbf{y}_k} \tag{5.32}$$

For the initial direction $\mathbf{p}_0$, the solution of the reduced system is used ( $\mathbf{p}_0 = \mathbf{y}_0$ ).

The preconditioning of linear systems accelerates the convergence rate of the CG method (Nocedal and Wright, 1999; Newman and Boggs, 2004). There is no single or best way for all types of linear systems. A good preconditioning strategy is to design the preconditioner for specific types of linear systems. This may be to solve a reduced or simple version ( $\mathbf{M}\mathbf{y} = \mathbf{r}$ ) of the original linear system.

The model structure terms ($\mathbf{W}_r$ and $\mathbf{W}_s$) are very sparse matrices that include only two elements and one element in each row, as mentioned in the previous section. Also, due to the trade-off parameter being a very large number, the linear system of the GN algorithm is dominated by that parameter. Therefore, obtaining an approximate

solution by using only model structure terms is both inexpensive and close to the original system of the GN method (Haber et al., 2000). The reduced system is given as the following:

$$\begin{aligned}\left\{\lambda^k \alpha_r \mathbf{W}_r^T \mathbf{W}_r + \lambda^k \alpha_s \mathbf{W}_s^T \mathbf{W}_s\right\} \mathbf{y}_k \\ = \mathbf{J}^{k-1^T} \mathbf{W}_d^T \mathbf{W}_d \left(\mathbf{d}_{obs} - \mathbf{d}_{cal}^{k-1}\right) \\ - \lambda^k \left(\alpha_r \mathbf{W}_r^T \mathbf{W}_r \mathbf{m}^{k-1} - \alpha_s \mathbf{W}_s^T \mathbf{W}_s \left(\mathbf{m}^{ref} - \mathbf{m}^{k-1}\right)\right)\end{aligned} \tag{5.33}$$

The above system is preconditioned and solved by using incomplete LU factorization and the GMRES solver from the SPARSKIT package (Saad, 1990). The parameters '*lfil' and 'droptol'* for the incomplete LU factorization are chosen 3 and $10^{-3}$ for all examples that are shown in the next Chapter. The reduced system is solved with relatively high tolerance (e.g., $10^{-5}$ or $10^{-6}$) by 100 times iterating the GMRES solver.

### 5.5 Nonpreconditioned generalized minimal residual method

Unlike the CG method, the GMRES method is designed to solve nonsymmetric linear systems. It is an extension of the MINRES method, which can be applied only to symmetric matrices (Saad and Schultz, 1986). Similar to the CG method, the GMRES method starts with the calculation of the residual that is obtained by multiplying the left-hand matrix **A** with an arbitrary vector $\mathbf{x}_0$:

$$\mathbf{r}^0 = \mathbf{b} - \mathbf{A}\mathbf{x}^0 \tag{5.34}$$

In the CG method, the residuals form an orthogonal basis for the space $span\left\{r^0, Ar^0, A^2r^0, ...\right\}$; however, this basis is formed explicitly in the GMRES method.

$$\mathbf{V}^1 = \mathbf{r}^1 / \left\| \mathbf{r}^1 \right\|_2 \tag{5.35}$$

where **V** is a matrix, whose columns span Krylov subspace. The calculation sequence of the Krylov subspace vectors is given as the following:

$$\bar{\mathbf{H}}^k = \mathbf{A}\mathbf{V}^k \tag{5.36}$$

$$\bar{\mathbf{H}}^k = \bar{\mathbf{H}}^k - \left( \bar{\mathbf{H}}^k, \mathbf{V}^l \right) \mathbf{V}^l \tag{5.37}$$

$$\mathbf{V}^{k+1} = \bar{\mathbf{H}}^k / \left\| \mathbf{H}^k \right\|_2 \tag{5.38}$$

where $\bar{\mathbf{H}}$ is an upper Hessenberg matrix, and the superscript $k$ is the current GMRES iteration. $l$ is a number that changes in each GMRES iteration from 1 to k for the calculation of the current elements of the Hessenberg matrix. The above calculation is known as the Gram-Schmidt orthogonalization, and applying this calculation to a Krylov sequence is known as the Arnoldi method. Once the target residual norm is reached, the update vector is given by the following function:

$$\mathbf{x}^k = \mathbf{x}^0 + \mathbf{V}\mathbf{y} \tag{5.39}$$

where the vector **y** is the solution of the upper triangular system:

$$\mathbf{y}^k = \bar{\mathbf{H}}^{k^{-1}} \left\| \mathbf{r}^0 \right\|_2 \mathbf{e}_1 \tag{5.40}$$

where $\mathbf{e}_1$ is a unit vector (Saad and Schultz, 1986). When the number of GMRES iterations (the number of Krylov subspace vectors) increases, the calculation effort and memory requirements will increase. Further, if the number of GMRES iterations is very large, the method may not converge. On the other hand, the GMRES method can be used with the restart option. In the restart option, the number of the Krylov

subspace is chosen as a reasonable number depending on the linear system, and the GMRES algorithm is restarted until the desired residual norm is obtained. Even though choosing the size of the Krylov subspace to be small reduces computational efforts and memory requirements, it can cause the total number of iterations to increase. Therefore, the number of Krylov subspace vectors should be chosen in a careful manner.

# Chapter 6

# Inversion Examples

## 6.1 Introduction

In this chapter, three geophysical scenarios are presented to verify the inversion code. For all scenarios, an x-directed grounded wire is used as a source and data over a range of frequencies are considered. The coefficient matrix of the forward modelling is factorized once for all frequencies using MUMPS for each GN iteration, and this factorization is reused to calculate the vector product of the Hessian matrix. The linear system of the GN method is solved by using preconditioned CG and nonpreconditioned GMRES iterative solvers. In the first example, the conductive block example that is shown in Section 4.4 is inverted using only the x-component of the electric field as data; however, in the second example, both the x-component of the electric field and the z-component of the magnetic field are used to invert the geophysical scenario. For the last example, the Ovoid model shown in Section 4.7 is inverted to show the flexibility of the unstructured tetrahedral grids over complex geology. Similar to the second example, the x-component of the electric field and the z-component of the magnetic field are used as data.

## 6.2 Conductive block example 1

In this example, synthetic data were calculated at 105 observation locations using a 100 m long x-directed grounded wire for four frequencies (100, 30, 3, and 0.3 Hz).

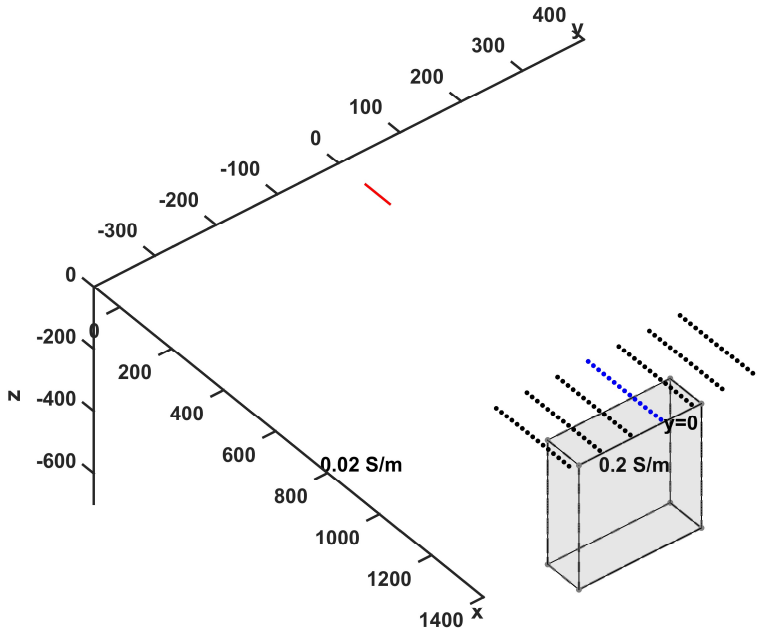


Figure 6.1 Plan view of the model that is used to generate synthetic data. Dots denote observation points, and the blue ones denote the profile used for the comparison between synthetic data and the inversion result. The solid red line shows the source location.

The observation points were located by spacing of 20 m and 50 m for the x- and y-directions, respectively, and the mesh at the observation points and the source location was refined by inserting tetrahedrons of 10 m size. The scenario is depicted in Figure 6.1. To represent the conductive block properly, the maximum volume of the tetrahedrons was set equal to 800 $m^3$. This resulted in 25223 nodes, 149816 tetrahedral elements, and 176822 edges.

The real and imaginary parts of $E_x$ were used as data; therefore, the number of data is 840. Random Gaussian noise was added to each datum with 2% standard deviation to make a noisy dataset. The maximum volume of the tetrahedrons in the active part of the mesh where cell conductivities are not constant was set to 24000 $m^3$, and the dimension of the active part is 1500×800×700 m (see Figures 6.1 and 6.2). The

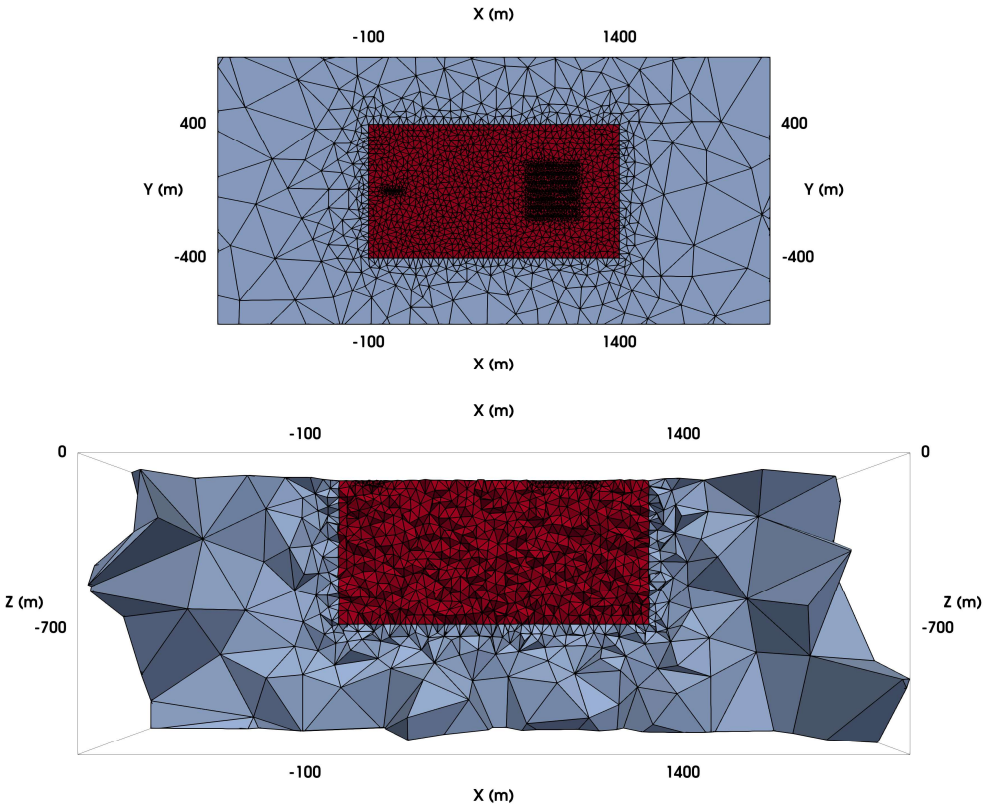


Figure 6.2 Unstructured mesh used for inversion procedure. Top panel shows an enlarged xy section of the mesh; the bottom panel shows an enlarged xz section of the mesh. The dark red section is the active part of the mesh.

number of nodes, elements, and edges for the inversion procedure, are 18536, 115352 (62774 of elements in the active part), and 134263, respectively. This results in more than 1 million unknowns that needed to be determined for four frequencies in each GN iteration.

The inversion was started with the initial guess of 0.02 S/m, which is the half-space conductivity. The computation was done on a laptop having an Intel I7-9750H processor and 40 GB memory. The coefficient matrix of the forward-modelling operator was factorized once with the LU factorization option of MUMPS for four frequencies to obtain forward-modelling response, and this factorization was re-used for the calculation of the vector product of the Jacobian matrix for each GN iteration.

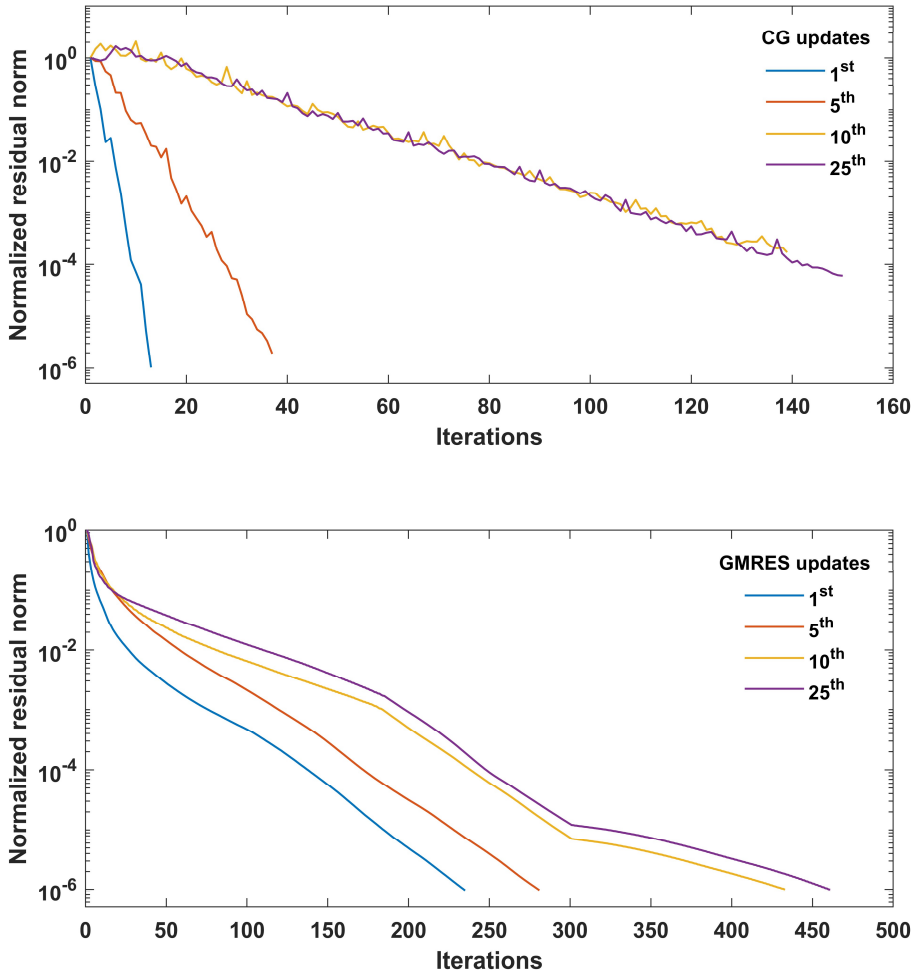


Figure 6.3 Convergence curves of the preconditioned CG solver (top panel) and nonpreconditioned GMRES solver (bottom panel) for different iterations of the GN inversion procedure.

Memory usage was about 25 GB for the factorization step, and the computation time for this step was about 860 s. The solution step took 3.7-4.2 s, which depends on the density of the right-hand side vectors. The inversion procedure was repeated by using preconditioned CG and nonpreconditioned GMRES solvers for the comparison between iterative solvers. The initial trade-off parameter was chosen to be $10^5$ and multiplied by the cooling factor 0.5 for each GN iteration until the target misfit was reached. To avoid over-fitting the data the target misfit was chosen to be 840

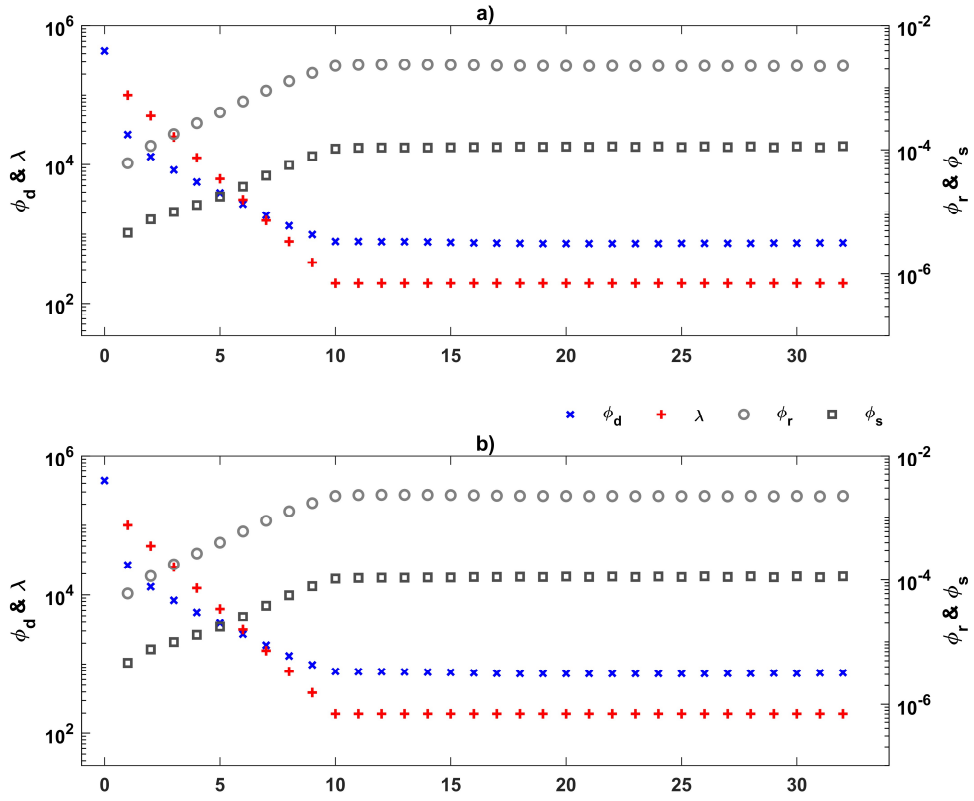


Figure 6.4 Inversion progression with iterations of data misfit, trade-off parameter (left axis), and measure of the model structure (right axis). Panel a for the CG solver; panel b for the GMRES solver.

which is equal to the number of data for this example. When the $l_2$ norm of the model update vector, $\delta\mathbf{m}^k$, was less than $10^{-3}$, the minimum-structure inversion procedure was terminated. For the preconditioned CG algorithm, the reduced system (Equation 5.33) was preconditioned using incomplete LU factorization and solved using the GMRES solver from the SPARSKIT package (Saad, 1990). The parameters '*lfil*' and '*droptol*' were chosen to be 3 and $10^{-3}$ for the incomplete LU factorization. Using a large value for the '*lfil*' can increase the memory demand (Jahandari and Farquharson, 2017) because the parameter controls the number of elements in each row of the triangle matrices L and U. Using a small value for the '*droptol*' can increase

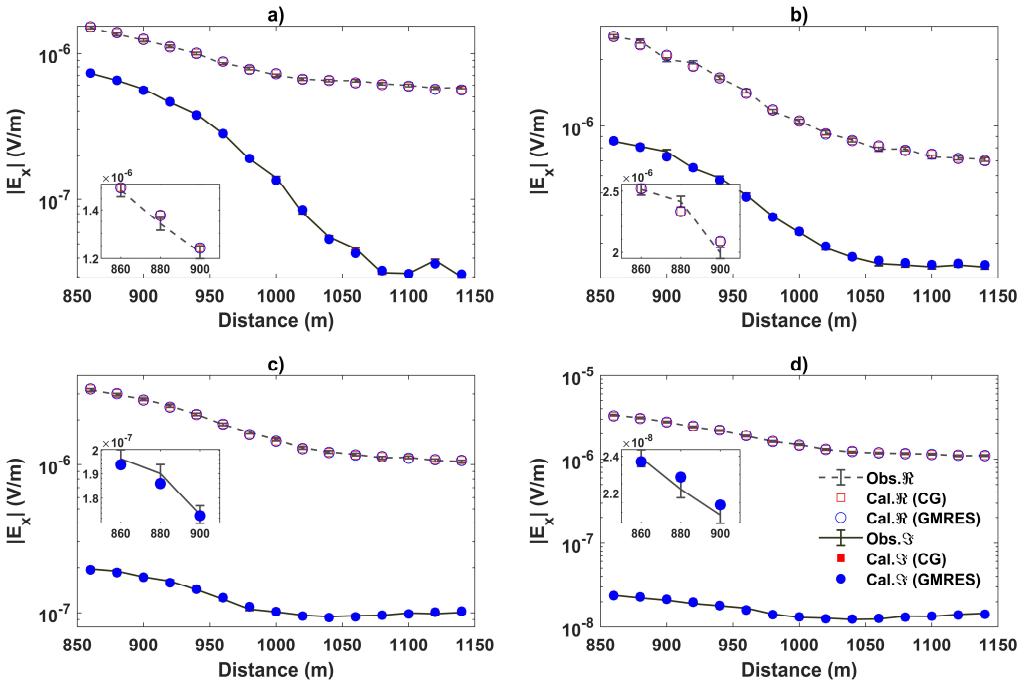


Figure 6.5 A comparison between the observed and calculated data for the profile shown in Figure 6.1 with blue dots. Panels a, b, c, and d show frequencies of 100, 30, 3, and 0.3, respectively.

memory requirements. On the other hand, using a low value for the parameter '*droptol*' can increase the convergence rate because the parameter is a measurement of how 'incomplete' the LU factorization is (Saad, 1996). 100 iterations were found to be enough to reduce the relative residual norm 5-6 orders of magnitude by setting the Krylov subspace to 200. Preconditioning and solving the reduced linear system of the GN method was quite fast (about 13 s) because the left-hand side matrix of the system was very sparse. The vector product of the Hessian matrix must be recalculated in each CG iteration even though the Jacobian matrix does not change during the CG iteration. As mentioned in Section 5.3, two pseudo-forward modellings are needed for the calculation of the vector product of the Hessian matrix. Therefore, approximately 22 s were needed for each preconditioned CG iteration for this example. 150 CG

iterations were used to solve the linear system of each GN iteration, which reduced the residual norm 4 orders of magnitude. For different GN iterations, the convergence curves of the preconditioned CG solver are given in Figure 6.3. By using the CG solver, the target misfit was reached at the $10^{th}$ GN iteration, and the total number of the GN iterations was 32 (Figure 6.4a). Obtaining the result at the end of the 32 GN iterations took approximately 30 hr.

The example was also solved by using the nonpreconditioned GMRES solver with the restart option. The Krylov subspace was 300; the target relative residual norm was $10^{-6}$. Similar to the CG solver, the vector product of the Hessian matrix must be recalculated in each GMRES iteration. However, in this implementation, there was no preconditioning step; therefore, each GMRES iteration approximately took 9 s. Due to the same reason, the GMRES iterative solver requires more iterations. The convergence curves of the GMRES solver are given in Figure 6.3. It can be seen from Figure 6.3 that the GMRES solver is more stable than the CG solver. The target misfit was reached at the $10^{th}$ iteration (Figure 6.4b). The obtained result took 32 GN iterations, and the total computation time was approximately 33 hr for this example. Data fits are given in Figure 6.5 for the profile that is shown with blue dots in Figure 6.1 for all frequencies considered. It can be said that there is a good agreement between synthetic observed and calculated data. The recovered model is given for the xz- and yz-sections in Figures 6.6 and 6.7. The conductive body was fully recovered; however, the model has a smeared-out shape as expected due to the $l_2$ measure of model roughness (see Farquharson, 2008).

## 6.3 Conductive block example 2

In this synthetic example, a grounded electric wire whose length is 400 m extending along the x-direction from -200 m to 200 m on the flat Earth's surface was used with

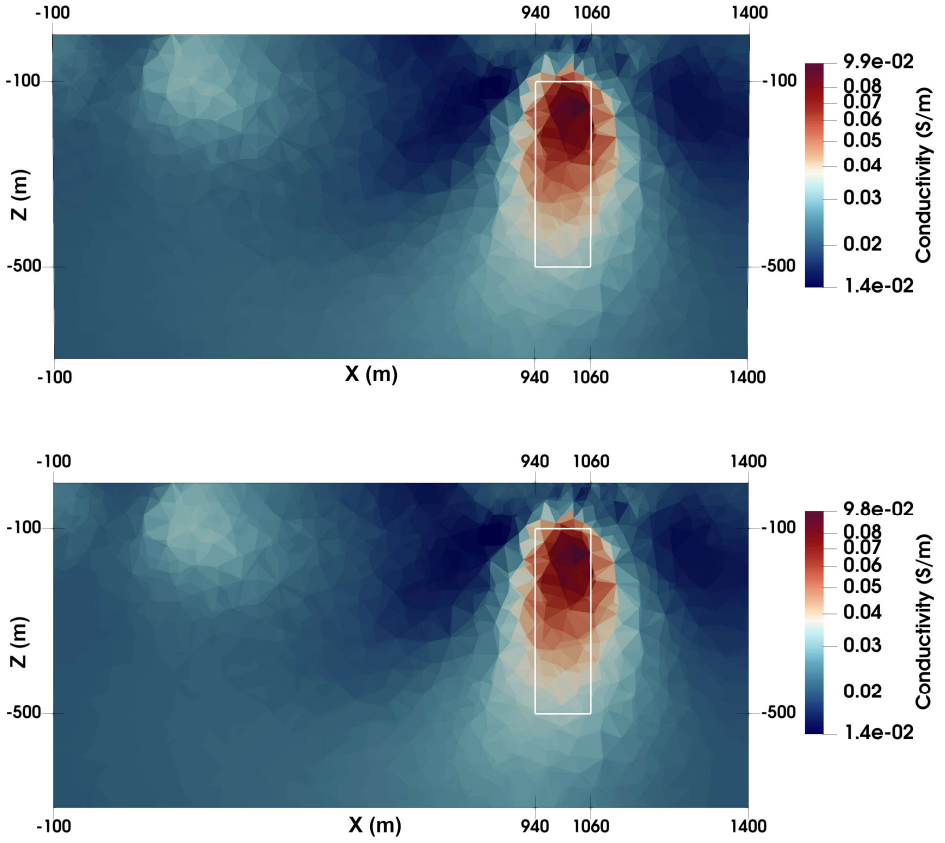


Figure 6.6 xz-section of the recovered models at y=0 m. The top panel shows the recovered model that was obtained using the CG solver; the bottom panel shows the recovered model that was obtained using the GMRES solver. The white rectangle represents the conductive block.

the dipole moment of 400 Am. The conductivity of the buried block is 0.5 S/m in a homogeneous half-space of 0.01 S/m. The dimension of the block is $400 \times 500 \times 300$ m in the x-, y-, and z-directions, respectively (Figure 6.8). The mesh at the source and observation locations were refined by inserting additional tetrahedrons whose size is 10 m. The dataset was calculated at 99 points for the frequencies of 50, 10, and 1 Hz.

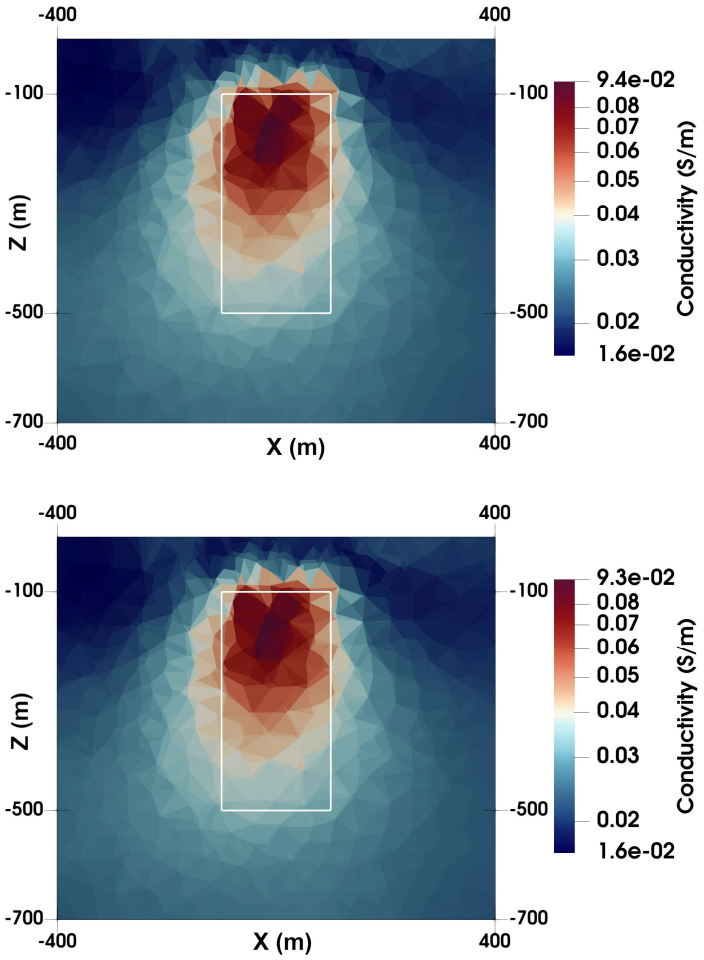


Figure 6.7 yz-section of the recovered model at x=1000 m. The top panel shows the recovered model by using the CG solver; the bottom panel shows the recovered model by using the GMRES solver. The white rectangular represents the conductive block.

The mesh that was used to generate synthetic data consisted of 34062 nodes, 169860 elements, and 239346 edges. The real and imaginary parts of $E_x$ and $H_z$ were used for the inversion; therefore, 1188 data were used for the inversion. Gaussian random noise of 2% of each datum was added to make noisy data. The maximum volume of the tetrahedrons in the active part of the mesh was set to $8.7\times10^4$ $m^3$, and the dimension of the active part was 2000×1900×1000 m. The mesh used for the inversion consisted of 33054 nodes, 202311 elements (108571 of the elements in the

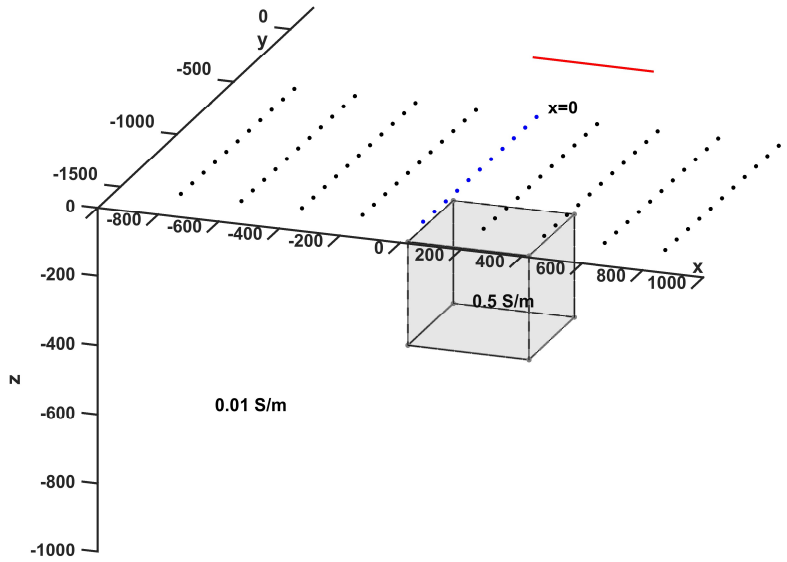


Figure 6.8 Plan view of the second example. Dots show observation locations; blue ones show the profile used for the comparison of observed and calculated data. The solid red line demonstrates the source.

active part), and 237070 edges (Figure 6.9). Initial and reference models were the half-space conductivity. Forward modelling and pseudo-forward modellings were solved by using MUMPS. 34 GB memory was used to factorize the coefficient matrix for the three frequencies. Computation time for the factorization step was about 1430 s, and solution steps took 5-6 s depending on the right-hand side vector. Note that physical memory was not enough to solve this system; therefore, the swap area in the storage was used during factorization. Similar to the first example, the inversion was repeated by using preconditioned CG and nonpreconditioned GMRES solvers. The initial trade-off parameter was chosen as $5\times10^5$, and the parameter was halved in each GN iteration.

The reduced system (Equation 5.33) was preconditioned and solved using incomplete LU factorization and GMRES solver. The preconditioner parameters, '*lfil*' and

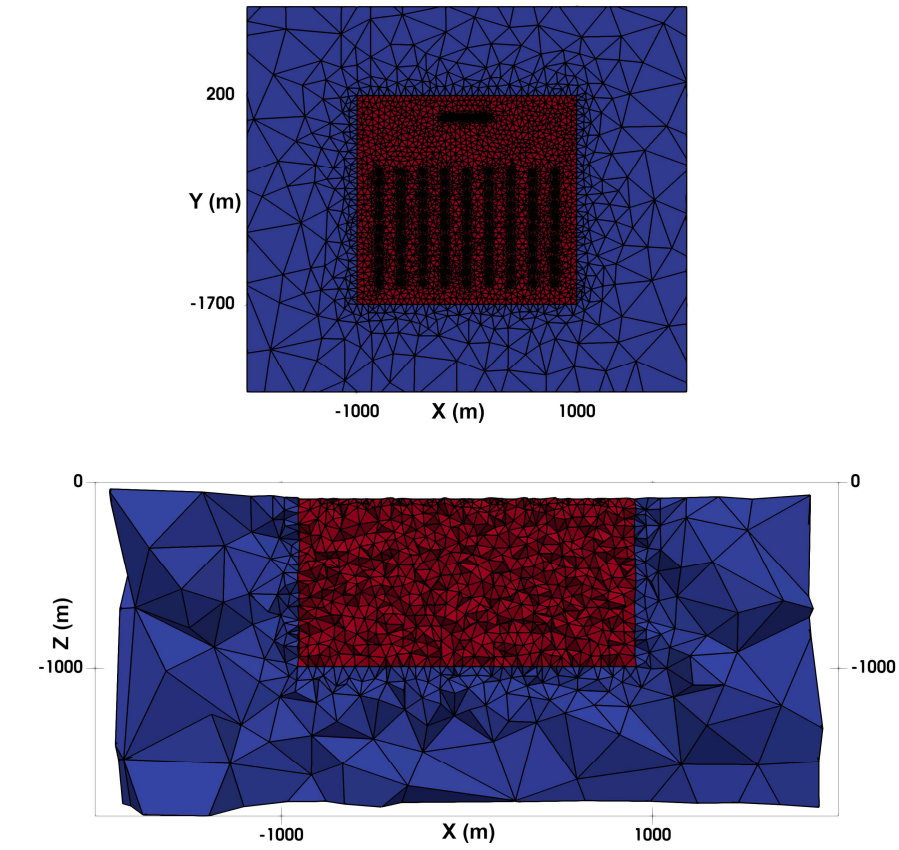


Figure 6.9 Tetrahedral mesh used for the second inversion example. The top panel is the enlarged xy-section; the bottom panel is the enlarged yz-section

'*droptol*', were used as 3 and $10^{-3}$. The Krylov subspace was 200. This step approximately took 14 s, which reduced the residual norm 6 orders of magnitude; therefore, each CG iteration took about 25 s. The preconditioned CG solver was iterated until the residual norm had been reduced 4 orders of magnitude. The convergence curves of the CG solver are given in Figure 6.10. For this example, the CG solver was quite unstable and required many more iterations compared to the first example. Similar to the first example, the nonpreconditioned GMRES iterative solver was used to solve the linear system of the inversion with the restart option. The Krylov subspace was 300, and the target residual norm was $10^{-6}$. Each GMRES

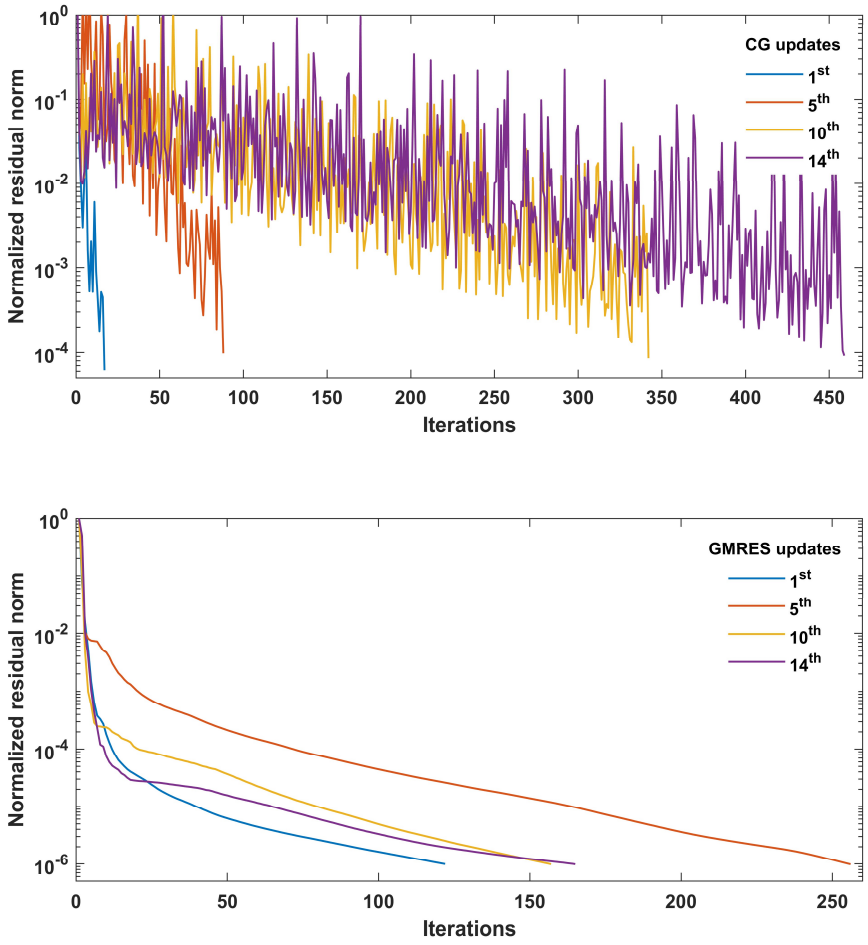


Figure 6.10 Convergence curves of the CG (top) and GMRES (bottom) solvers for various GN iterations.

iteration approximately took 11 s. The convergence of the GMRES solver was quite stable; therefore, reaching the target residual norm took fewer iterations than the CG solver (see Figure 6.10). However, the target misfit (the number of data) could not be reached by using the two solvers because continuing to multiply the trade-off parameter by the cooling factor caused artifacts which led the data misfit to increase. Therefore, the trade-off parameter was reduced until 488, then was kept constant. The inversion was terminated when the norm of the model update vector was less than $10^3$. Total computation times were 26 hr and 22 hr by using the CG and GMRES

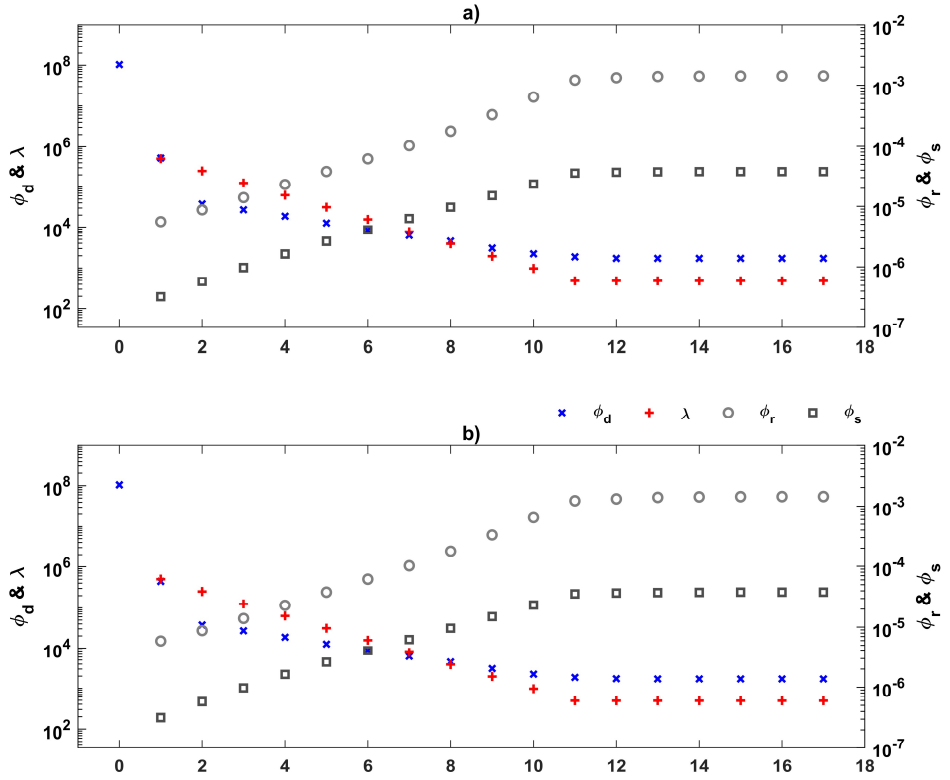


Figure 6.11 Inversion progression with iterations of data misfit, trade-off parameter (left axis), and measure of the model structure (right axis) for the second example. Panel a for the CG solver, panel b for the GMRES solver.

solvers, respectively, and obtaining the final model took 17 GN iterations. The final data misfit was 1714 for both solvers (Figure 6.11).

A comparison between the observed and calculated data is given for the frequency of 10 Hz in Figure 6.12 for the profile shown in Figure 6.8 with blue dots. It can be said that there is a good agreement between observed synthetic and calculated data except for the imaginary part of $H_z$. This component has larger uncertainties compared to the other components; therefore, the contribution of the component to the data misfit is less. The contour maps of the total fields are given for all used frequencies and EM field components in Figures 6.13 and 6.14, and the recovered models are given in Figures 6.15 and 6.16.

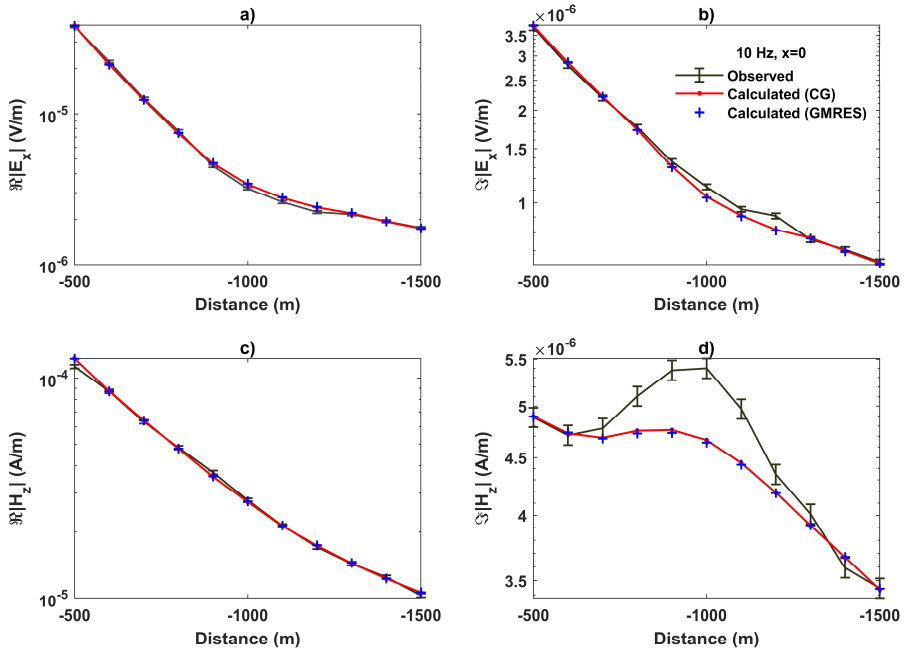


Figure 6.12 A comparison between the observed and calculated data for the profile shown in Figure 6.8 with blue dots. Panels a and b show real and imaginary parts of $E_x$, and panels c and d show real and imaginary parts of $H_z$.

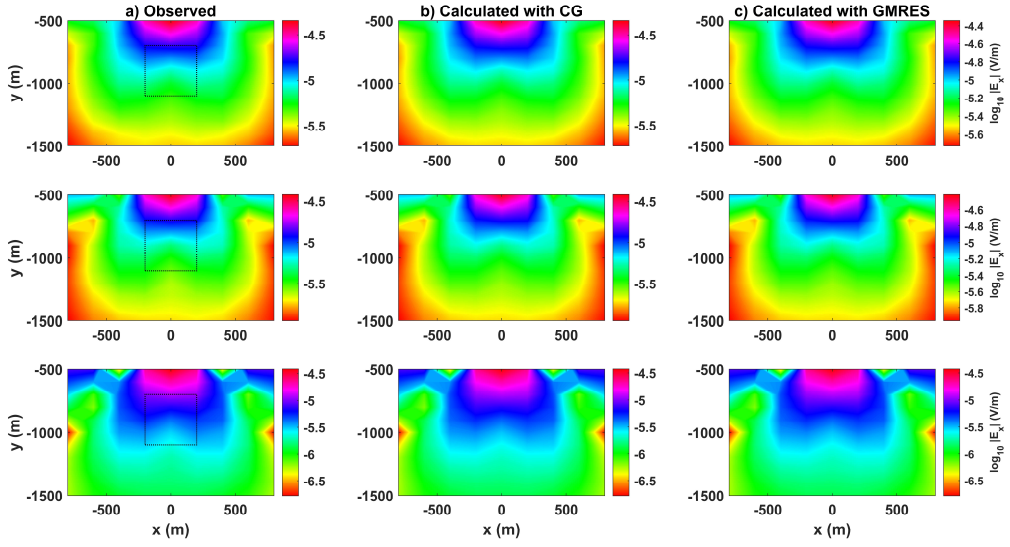


Figure 6.13 Contour maps of the total $E_x$ field. Panels a, b, and c show observed and inverted data for frequencies of 50, 10, and 1 Hz (from top to bottom). The dotted black line denotes the location of the buried block.

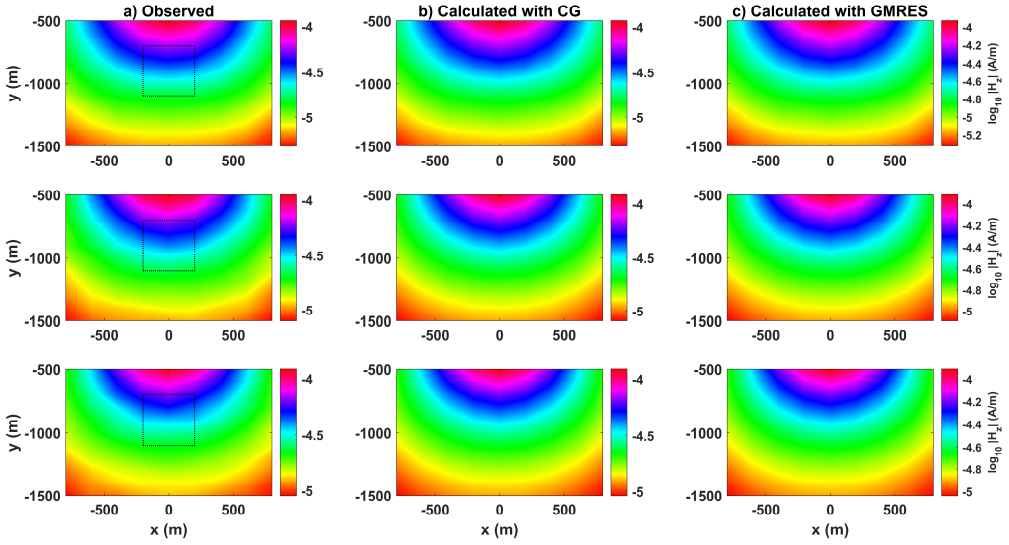


Figure 6.14 Contour maps of the total $H_z$ field. Panels a, b, and c show observed and inverted data for frequencies of 50, 10, and 1 Hz (from top to bottom). The dotted black line denotes the location of the buried block.

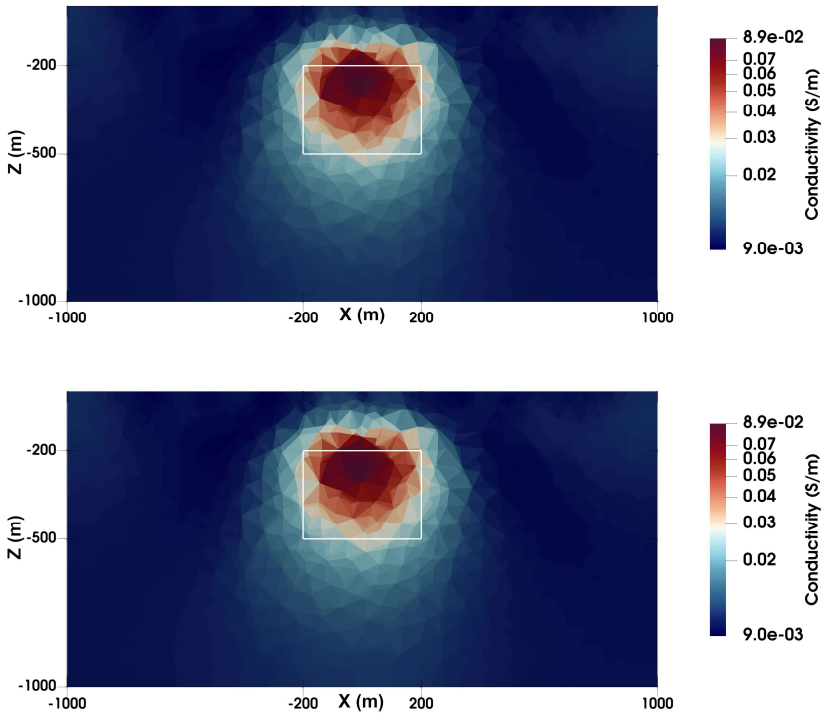


Figure 6.15 xz-section of the recovered models at y=900 m. The top panel shows the recovered model that was obtained using the CG solver; the bottom panel shows the recovered model that was obtained using the GMRES solver. The white rectangle represents the conductive block.

## 6.4 Realistic Ovid model

In this example, a similar model to that shown in Section 4.7 is used. A grounded electric wire whose length is 400 m along the x-direction on the topographic Earth's surface was used with the dipole moment of 400 Am. The conductive body was located 50 m deeper (the inversion algorithm has a tendency to put the ore body deeper because the CSAMT method is not as good as Helicopter EM at determining shallow structures) compared to the forward-modelling example in a homogeneous background of 0.001 S/m and the conductivity of the body was chosen to be 1 S/m (Figure 6.17). The forward-modelling mesh at the source and observation locations was refined by inserting additional tetrahedrons whose size is 5 m. The dataset was calculated at 143 points for the frequencies of 1500 Hz and 500 Hz. The mesh used to

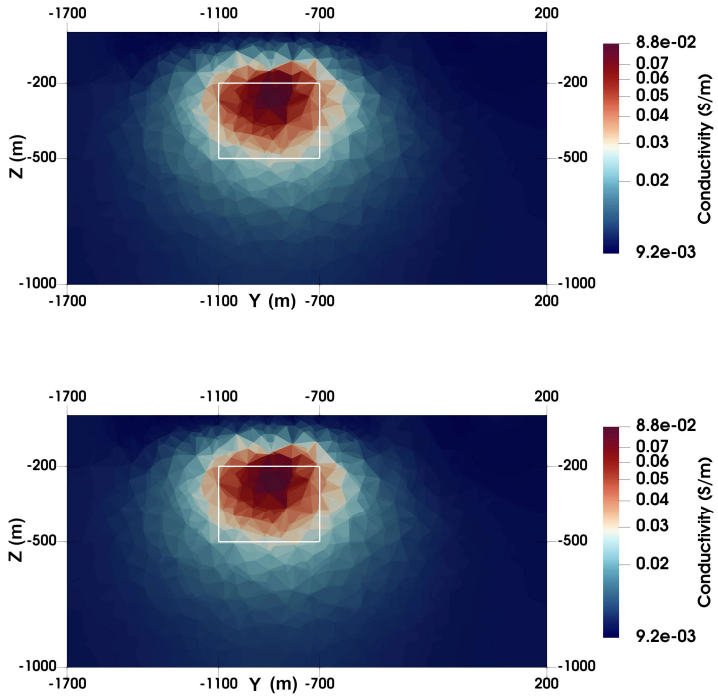


Figure 6.16 yz-section of the recovered model at x=0 m for the second example. The top panel shows the recovered model by using the CG solver; the bottom panel shows the recovered model by using the GMRES solver. The white rectangle represents the conductive block.

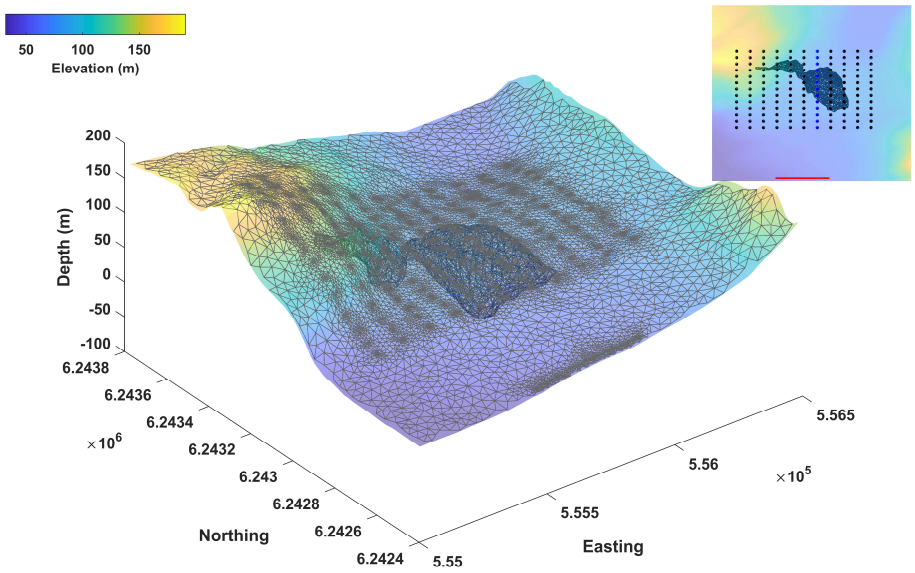


Figure 6.17 Surface mesh and topography of the realistic model. The dots show the observation locations, and the red line represents the grounded wire.

make a synthetic dataset consisted of 44230 nodes, 275849 elements, and 320282 edges.

The real and imaginary parts of $E_x$ and $H_z$ were used for the inversion; therefore, the dataset consisted of 1144 data. To make a noisy dataset, Gaussian random noise of 5% of each datum was added. The mesh used for the inversion consisted of 52044 nodes, 325873 elements (162904 of the elements in the active part), and 378085 edges. The initial and reference models were chosen to be 0.001 S/m. The initial trade-off parameter was chosen as $1\times10^7$ and this parameter was multiplied by the cooling factor of 0.7 in each GN iteration.

The inversion of this model was completed with a laptop having an Intel I7-9750H processor and 40 GB of RAM. Forward modelling and pseudo-forward modelling were solved by using MUMPS. 35 GB memory was used to factorize the linear

systems of equations for the two frequencies. Computation time for the factorization step was about 1560 s, and solutions steps took about 5-6 s depending on the right-hand side vectors. Similar to the previous examples, the inversion process was repeated using preconditioned CG and nonpreconditioned GMRES solvers.

The reduced linear system of the inversion process (Equation 5.33) was solved by using preconditioned GMRES solver in each CG iteration, and this step took about 16 s, which decreased the residual norm of the reduced system 6 orders of magnitude. The preconditioned CG solver was iterated until the residual norm of the inversion (Equation 5.13) had been reduced 6 orders of magnitude. The convergence curves of the CG solver are given in Figure 6.18. It can be seen that the CG solver was quite unstable; however, the convergence rate of the solver was very high in the first

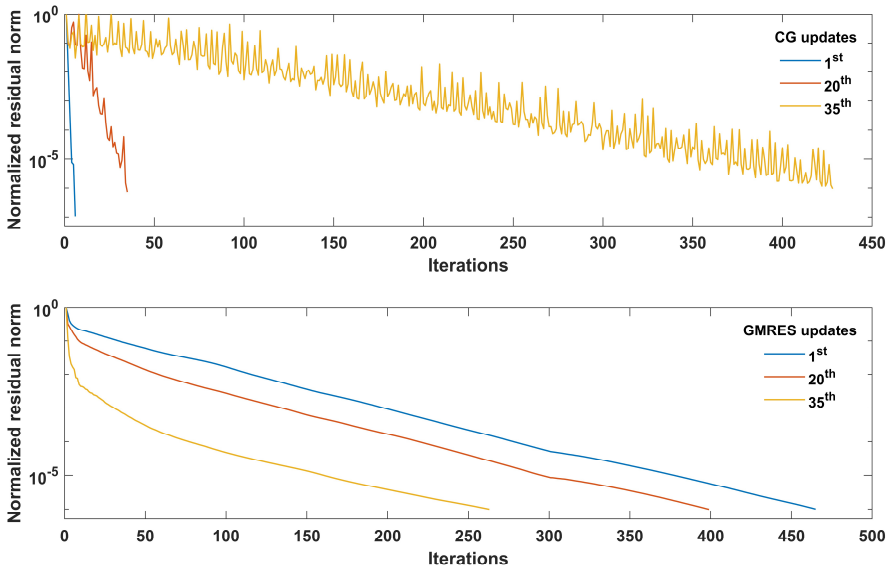


Figure 6.18 Convergence curves of the CG (top) and GMRES (bottom) solvers for the realistic model.

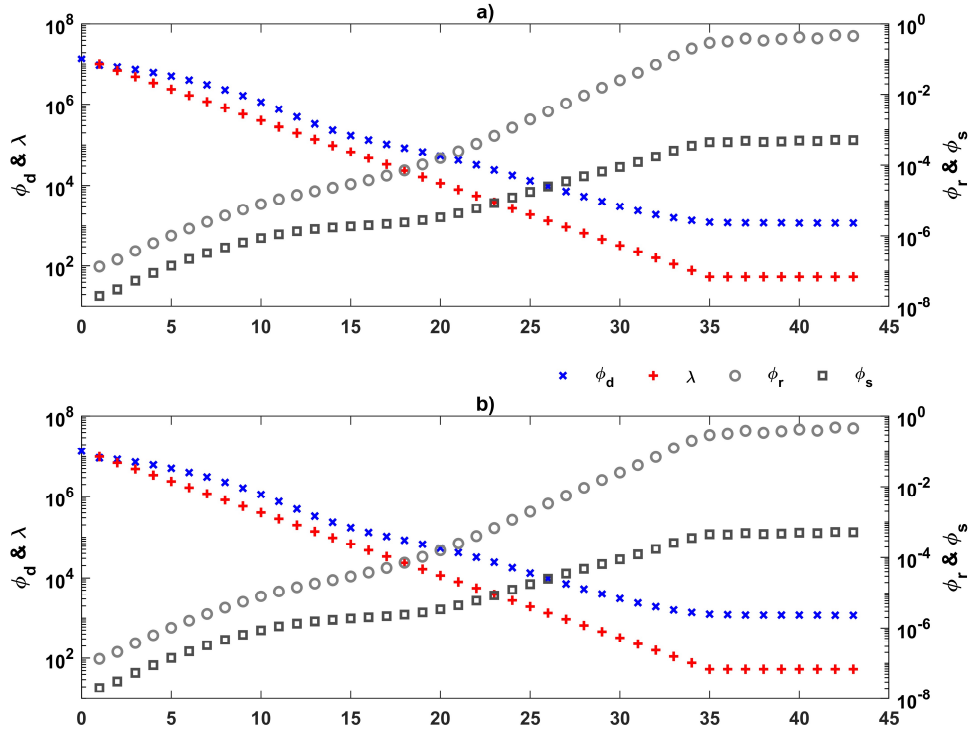


Figure 6.19 Inversion progression with the iterations of data misfit, trade-off parameter (left axis), and measure of the model structure (right axis) for the Ovoid model. Panel a for the CG solver, and panel b for the GMRES solver.

iterations. The target misfit was reached at the 35$^{th}$ iteration, and the inversion was terminated at the 43$^{rd}$ iteration. The total run time was 85 hr for this example. The same dataset was solved using nonpreconditioned GMRES solver. The dimension of the Krylov subspace was 300, and the target residual norm was chosen to be $10^{-6}$. The GMRES solver had a stable convergence (Figure 6.18); however, the convergence rate of the solver was low due to being nonpreconditioned. Similar to the CG solution, the target misfit was reached at the 35$^{th}$ iteration, and the inversion was terminated at the 43$^{rd}$ iteration. The total run time with the nonpreconditioned GMRES solver was about 103 hr. The inversion progression with the iterations for both solvers is given in Figure 6.19. Figure 6.20 shows a comparison between the observed and calculated

data for the profile shown in Figure 6.17 with the blue dots. It can be said that the fit between the observed and calculated data is good. The contour maps of the total fields are given for the two frequencies in Figures 6.21 and 6.22. The recovered model is given in Figures 6.23 and 6.24, and it can be seen that the shape of the recovered model resembles the real model.

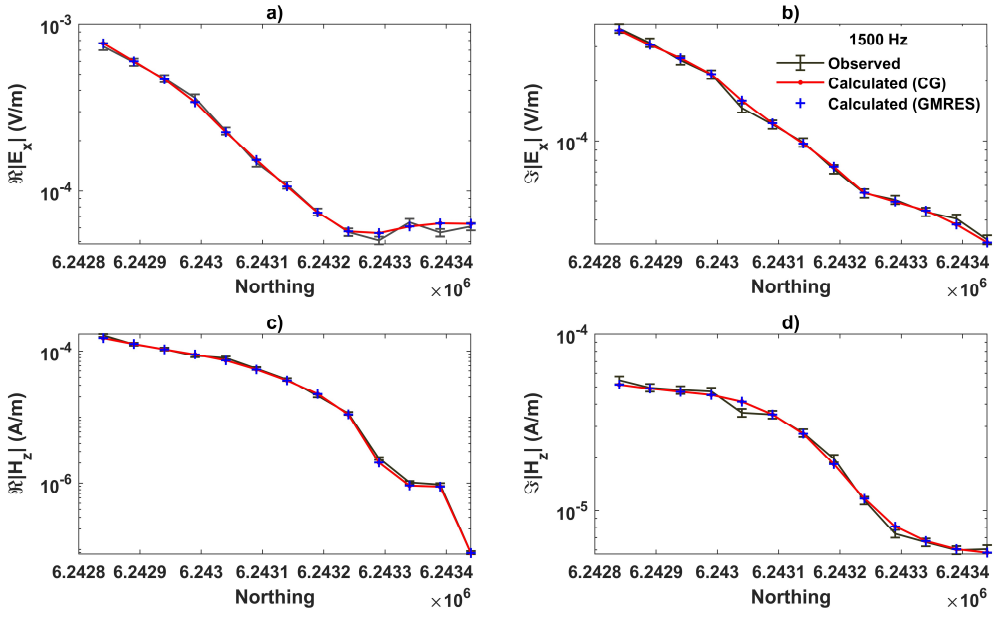


Figure 6.20 A comparison for the Ovoid model between the observed and calculated data for the profile shown in Figure 6.17 with the blue dots. Panels a and b show the real and imaginary parts of $E_x$, and panels c and d show the real and imaginary parts of $H_z$.

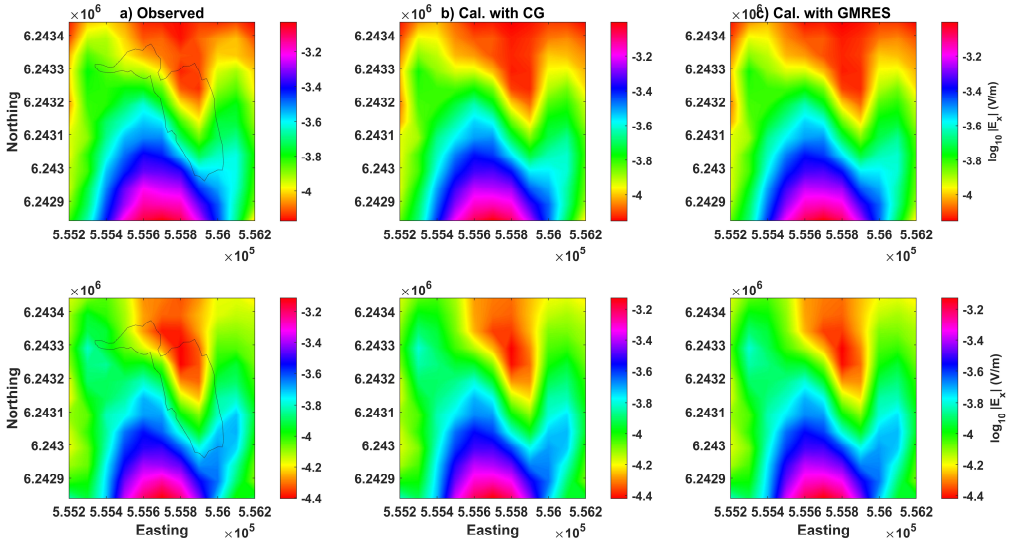


Figure 6.21 Contour maps of the total $E_x$ field for the Ovoid model. Panel a shows the observed data. Panel b and c show the inversion results. The top panels show the results for 1500 Hz and the bottom panels show the results for 500 Hz. The dotted black line represents the frame of the Ovoid body.

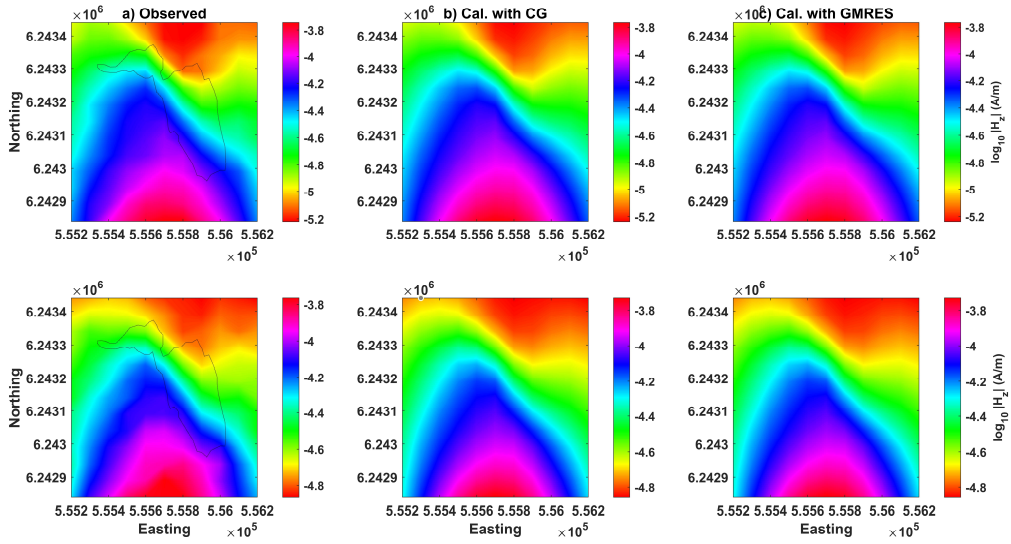


Figure 6.22 Contour maps of the total $H_z$ field for the Ovoid model. Panel a shows the observed data. Panel b and c show the inversion results. The top panels show the results for 1500 Hz and the bottom panels show the results for 500 Hz. The dotted black line represents the frame of the Ovoid body.

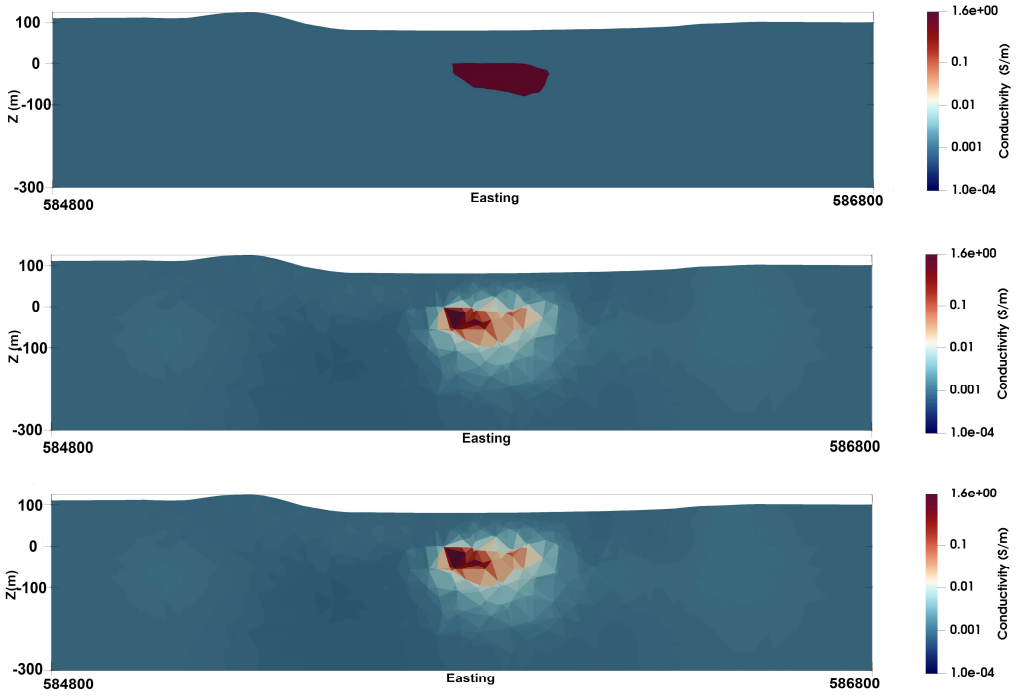


Figure 6.23 The vertical section of the Ovoid and recovered models at northing= 6243100. The middle panel shows the recovered model by using the CG solver; the bottom panel shows the recovered model by using the GMRES solver.

## 6.5 Effect of the Krylov subspace on the convergence rate

As mentioned in Section 5.5, the number of Krylov subspace vectors affects the convergence rate and memory usage of the GMRES solver (also see Jahandari and Farquharson, 2017). In this section, a test was conducted based on different dimensions of the Krylov subspaces for the first inversion example. Krylov subspace dimensions of 50, 100, and 300, respectively, were chosen. The converge curves of the 2$^{nd}$ GN iteration are given in Figure 6.25. Further, the memory usage was observed for the three Krylov subspaces; however, the difference in memory usage was not noticeable because the number of inversion parameters was not large for the first example.

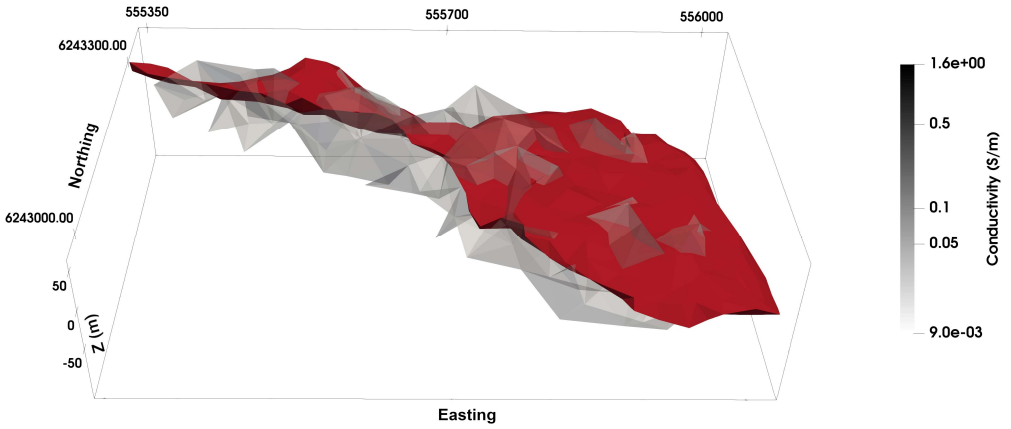


Figure 6.24 A comparison between the Ovoid model and recovered model. The gray model shows the threshold view of the recovered model between the conductivity of 0.01 and 1.6 S/m. The dark red body represents the model used for the forward modelling.

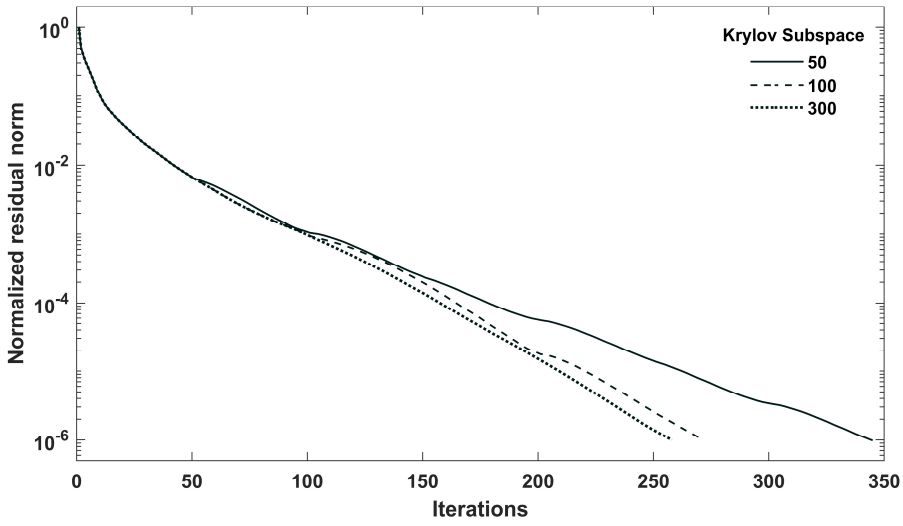


Figure 6.25 A comparison for the GMRES solver with different Krylov subspaces.

It is obvious that if the number of Krylov subspace vectors is chosen as a small number, the GMRES solver requires more iterations. On the other hand, there is not a very large iteration difference between 100 and 300 Krylov space for this example.

## 6.6 Conclusions

In this chapter, minimum-structure inversion was used to invert three synthetic CSAMT datasets. The three-dimensional domain was discretized into tetrahedral grids, and forward-modelling responses were calculated by using **A**-$\phi$ decomposition. The objective function was minimized by Gauss-Newton iterations. $l_2$ measures were used for both the measures of the data misfit and model structure. In each Gauss-Newton iteration, the linear system of equations for the forward modelling was factorized once with MUMPS for all used frequencies. Then this factorization was used for the calculation of vector products of the Jacobian matrix and Hessian matrix. Thus, preconditioned CG and nonpreconditioned GMRES solvers, which do not need the explicit calculation of the matrices for solutions of the linear systems, were used.

It can be said that the minimum-structure inversion was successfully applied by using tetrahedral grids. In the first example, only the x-component of the electric field was used as data. The linear system of the inversion was solved by both preconditioned CG and nonpreconditioned GMRES solvers. Both iterative solvers performed stable convergence rates; therefore, obtaining the final model of the preconditioned CG solver took less time. However, the CG solver was quite unstable in the second and third examples. Even though the nonpreconditioned version of the GMRES method was used, obtaining the recovered model took less time than the preconditioned CG solver. This test showed that the GMRES solver has greater stability than the CG solver. Further, all examples showed that using a preconditioner considerably increases the converge rate of a solver.

# Chapter 7

# Summary

In this thesis, three-dimensional forward modelling and inversion for the CSAMT method were investigated, and forward-modelling and inversion codes have been developed. The forward-modelling of the CSAMT method uses the finite-element scheme with unstructured tetrahedral grids, and the inversion code uses a regularized minimum-structure inversion scheme with the Gauss-Newton method. The main goal was to develop a flexible and complete tool for the interpretation of CSAMT data.

The CSAMT method is a frequency-domain EM method which uses an artificial source or sources. The advantage of the method over MT and AMT methods is that artificial sources provide reliable signals for measurements. A planewave approximation is valid for the method as long as measurements are made at a certain distance from the sources. However, if an inversion is considered for a dataset, then it is not needed to worry about whether the data are in the far-field zone or not. There are different types of measurements depending on the number of sources and components of the electromagnetic fields. The types of measurement used should be defined by considering geology. Further, measurement parameters such as frequency, and the distance between source and observation locations should be chosen carefully before measurements. The analytical solution for a conductive whole space was given to show the effects of these parameters in Chapter 2, and the calculation of the apparent resistivity and phases was given in the same chapter. Unstructured

tetrahedral grids are one of several grids suitable for the purpose of geophysical modelling. They can provide the necessary flexibility between geological contacts as well as for amorphous bodies. Further, they allow locally refined meshes where this is desired, e.g., source and observation locations. The software FacetModeller and TetGen were used for the construction of the models and the generation of tetrahedral grids. In TetGen, mesh quality is controlled by two flags, radius-edge ratio and dihedral angle. These two flags control mesh qualities, namely the shape of the tetrahedral grids, for computational domains.

The E-field equation was decomposed into vector and scalar potentials. The equation of conservation of charge and the Helmholtz equation were discretized by the method of weighted residuals. Vector basis functions were used for the approximation of the vector potentials. Similarly, scalar basis functions were used for the approximation of the scalar potentials. This decomposition results in a better-conditioned system than the direct E-field equation (Chapter 3). The direct solver, MUMPS, was used to solve the forward-modelling linear systems with LU factorization. This is important because MUMPS provides a fast solution when more than one source is used. Several benchmark tests were conducted, from simple to complex. In the first two benchmark tests, the FE results were compared with their analytical solutions; the other three tests were from the literature. In the last example, a realistic model was presented considering complex topography and body. Also, various conductivity values were used for the ore body to show how the code works with the large conductivity contrast. Further tests were conducted to show the effects of mesh quality and refinements on results. As mentioned in the above paragraph, the mesh quality is controlled by two parameters, radius-edge ratio and dihedral angle. Different values

of these parameters (e.g., 1.8 to 1.3 for the radius-edges ratio) and different sizes of refinement tetrahedrons (e.g., 10 and 5 m) were tested to demonstrate the effects on the FE results (Chapter 4).

The rest of this thesis is about inversion for the CSAMT method. Regularized minimum-structure inversion was applied with the Gauss-Newton method to invert the CSAMT data, and the objective function, which combines measures of data misfit and model structures, was minimized with $l_2$ norms. When data misfit reduces, model structure increases in this type of inversion. The measure of model structure part consists of two matrices, smallness and roughness. These matrices ensure geological information for the inversion process, and this helps to reduce ambiguity. The most intensive task in terms of memory and time is the calculation of the Jacobian matrix in gradient-based inversions, and the Jacobian matrix must be recalculated for each Gauss-Newton iteration. However, when iterative solvers such as conjugate gradient and generalized minimal residual methods are used, only vector products of matrices are needed to solve the linear system of inversions. In this thesis, preconditioned CG and nonpreconditioned GMRES solvers were implemented (Chapter 5). Three benchmark tests were conducted for the inversion code. First, synthetic CSAMT data were generated at multiple frequencies over conductive bodies. Noise was added, then the data were inverted by using CG and GMRES solvers. Both solvers could reduce the residual norms down to the desired level, and the recovered models were almost the same. On the other hand, the preconditioned CG solver was quite unstable for the second and third examples. In addition to that, it was seen that using a preconditioned iterative solver considerably increases the convergence rate of the solver.

The developed forward-modelling code is only capable of using a grounded wire as sources; however, the code can be modified easily for a general-purpose of controlled-source EM modelling in the frequency domain. An adaptive mesh refinement method can be considered for future work. The method used here was based on experiments and experiences; therefore, most of the meshes were generated several times for a model. Further, an adaptive mesh refinement method may reduce the computation efforts and improve the forward-modelling and inversion results. Here, the EM variables (e.g., conductivity) were assumed as scalar instead of tensors namely, modelling domains were assumed isotropic. Anisotropy can be investigated both for the forward modelling and inversion for future work because anisotropy may significantly affect EM measurements, for example, in sedimentary formations relevant to hydrocarbon exploration and in sheet-like zones of mineralization.

# References


Amestoy, P.R., Duff, I.S., Koster, J., and L'Excellent, J.Y., 2001, A fully asynchronous multifrontal solver using distributed dynamic scheduling, *SIAM Journal of Matrix Analysis and Applications*, **23**, 15–41.

Ansari, S., and Farquharson, C.G., 2014, 3D finite-element forward modeling of electromagnetic data using vector and scalar potentials and unstructured grids, *Geophysics*, **79**, E149–E165.

Ansari, S.M., 2014, Three-dimensional finite-element numerical modeling of geophysical electromagnetic problems using tetrahedral unstructured grids, PhD thesis, Memorial University.

Ansari, S.M., and Craven, J., 2020, A fully finite-element based algorithm for 3D magnetotelluric inversion, SEG Technical Program Expanded Abstracts.

Ansari, S.M., Craven, J., Schetselaar, E., and Farquharson, C., 2018, A finite-element based algorithm for 3d magnetotelluric inversion using unstructured meshes for complex geological Setti, 80th EAGE Conference and Exhibition 2018, 1-5

Avdeev, D.B., 2005. Three-dimensional electromagnetic modelling and inversion from theory to application. *Surveys in Geophysics*, **26**, 767–799.

Badea, B., Everett M., Newman, G., and Biro, O., 2001, Finite element analysis of controlled-source electromagnetic induction using coulomb-gauged potentials, *Geophysics*, **66**, 786-799.

Bartel, L.C., and Jacobson, R.D., 1987, Results of a controlled source audiofrequency magnetotelluric survey at the Puhimau thermal area, Kilauea Volcano, Hawaii, *Geophysics*, **52,** 665-677.

Biro, O., 1999, Edge element formulations of eddy current problems, *Computer Methods in Applied Mechanics and Engineering*, **169**, 391–405.

Boerner, D.E., Kurtz, R.D., and Jones, A.G., 1993b, Orthogonality in CSAMT and MT measurements, *Geophysics*, **58,** 924-934.

Boerner, D.E., Wright, J.A., Thurlow, J.G. and Reed, L.E., 1993a. Tensor CSAMT studies at the Buchans Mine in central Newfoundland, *Geophysics,* **58,** 12-19.

Bosh, M., Guillen, A., and Ledru, P., 2001, Lithologic tomography: an application to geophysical data from the Cadomian belt of northern Brittany, France, *Tectonophysics*, **331**, 197-227.

Castillo-Reyes, O., Puente J., and Cela, J.M., 2018, PETGEM: A parallel code for 3D CSEM forward modeling using edge finite elements, Computers and Geosciences, **119**, 123-136.

Coggon, J.H., 1971, Electromagnetic and Electrical Modeling by the Finite Element Method, *Geophysics*, **36**, 132-155.

Constable, S.C., Parker, R.L., and Constable, C.G., 1987, Occam's inversion-A practical algorithm for generating smooth models from electromagnetic sounding data, *Geophysics*, **52**, 289-300.

Dunham, W.M., Ansari S., and Farquharson, C.G., 2018, Application of 3D marine controlled-source electromagnetic finite-element forward modeling to hydrocarbon exploration in the Flemish Pass Basin offshore Newfoundland, Canada, *Geophysics*, **83**(2), WB33-WB49.

Farquharson, C. G., and D. W. Oldenburg, 2002, An integral equation solution to the geophysical electromagnetic forward-modelling problems: *in* M. S. Zhdanov and P.E. Wannamaker, eds., Methods in Geochemistry and Geophysics: Elsevier, Inc., 3-19.

Farquharson, C.G., 2007, Constructing piecewise-constant models in multidimensional minimum-structure inversions, *Geophysics*, **73**(1), 1-9.

Farquharson, C.G., and Miensopust, M., 2011, Three-dimensional finite element modelling of magnetotelluric data with a divergence correction, *Journal of Applied Geophysics*, **75**, 699-710.

Farquharson, C.G., and Oldenburg D.W., 1998, Non-linear inversion using general measures of data misfit and model structures, *Geophysical Journal International*, **134**, 213-227.

Farquharson, C.G., and Oldenburg, D.W. 2004, A comparison of automatic techniques for estimating the regularization parameter in non-linear inverse problems. *Geophysical Journal International*, **156**(3):411-425.

Fu, C., Di, Q., and An, Z., 2013, Application of the CSAMT method to groundwater exploration in a metropolitan environment, *Geophysics*, **78**(5), 201-209.

Garcia, X., Boerner, D.E., and Pedersen L.B., 2003, Electric and magnetic galvanic distortion decomposition of tensor CSAMT data. Application to data from the Buchans Mine (Newfoundland, Canada), *Geophysical Journal International*, **154**, 957-969.

Goldstein, M.A., 1971, Magnetotelluric experiments employing an artificial dipole source: Ph.D. thesis, University of Toronto.

Günther, T., Rücker, C., and Spitzer, K., 2006, Three-dimensional modelling and inversion of dc resistivity data incorporating topography – II. Inversion, *Geophysical Journal International*, **166**, 506-517.

Haber, E., 2004, Quasi-Newton methods for large-scale electromagnetic inverse problems, *Inverse Problems*, **21**, 305-323.

Haber, E., Ascher, U.M, Aruliah, D.A., and Oldenburg, D.W., 2000, Fast simulation of 3D electromagnetic problems using potentials, *Journal of Computational Physics*, **163**, 150-171.

Haber, E., Ascher, U.M., and Oldenburg, D., 2000, On optimization techniques for solving nonlinear inverse problems*, Inverse Problems*, **16**, 1263-1280.

Haber, E., Heldmann, S., and Ascher, U., 2007, Adaptive finite volume method for distributed non-smooth parameter identification, *Inverse Problems*, **23**(2), 1659-1676.

Hohmann G.W., 1983, Three-dimensional EM modeling, *Geophysical Surveys*, **6** 27-53.

Hohmann, G.W., 1975, Three-dimensional induced polarization and electromagnetic modeling, *Geophysics*, **40**(2), 309-324.

Hughes, L.J., and Carlson N.R., 1987, Structure mapping at trap spring oilfield, Nevada, using controlled-source magnetotellurics, *First Break*, **5**(11), 403-418.

Jahandari, H., 2015, Three-dimensional numerical modelling of gravity and electromagnetic data using unstructured tetrahedral grids, PhD thesis, Memorial University.

Jahandari, H., and Farquharson, C. (2017), 3-D minimum-structure inversion of magnetotelluric data using the finite-element method and tetrahedral grids. *Geophysical Journal International*, **211**(2),1189-1205.

Jahandari, H., and Farquharson, C.G., 2015, Finite-volume modelling of geophysical electromagnetic data on unstructured grids using potentials, *Geophysical Journal International*, **202**, 1859-1876.

Jahandari, H., and Farquharson, C.G., 2017, 3-D minimum-structure inversion of magnetotelluric data using the finite-element method and tetrahedral grids, *Geophysical Journal International*, 211, 1189-1205

Jin, J.M, 2014, *Finite element method in electromagnetics*, 3rd Ed. John Wiley and Sons, New York.

Lelièvre P.G., and Farquharson, C.G., 2013, Gradient and smoothness regularization operators for geophysical inversion on unstructured meshes, **195**, 330-341.

Lelièvre P.G., and Oldenburg D.W., 2009, A comprehensive study of including structural orientation information in geophysical inversions, *Geophysical Journal International*, 178, 623-637.

Lelièvre, P.G., Carter-Mcauslan, A.E., Dunham, W.M., Jones, D.J., Nalepa, M., Squires, C.L., Tycholiz, M.A., and Farquharson, C.G., 2018, FacetModeller: Software for manual creation, manipulation and analysis of 3D surface-based models, SoftwareX, **7**, 41-46.

Li, G., and Han, B, 2017. Application of the perfectly matched layer in 2.5D marine controlled-source electromagnetic modeling, *Physics of the Earth and Planetary Interiors,* **157,** 157-167.

Li, Y., and Oldenburg D.W., 1996, 3-D inversion of magnetic data, *Geophysics*, **61**(2), 394-408.

Lu, X., and Farquharson, C.G., 2020, 3D finite-volume time-domain modeling of geophysical electromagnetic data on unstructured grids using potentials, *Geophysics*, **85**(6), 221-240.

Mackie, R.L., and Madden T.R., 1993, Three-dimensional magnetotelluric inversion using conjugate gradients, *Geophysical Journal International*, **115**, 215-229.

Mitsuhata, Y., 2000, 2-D electromagnetic modeling by finite element method with a dipole source and topography, *Geophysics*, **65**(2), 465-475.

Mitsuhata, Y., and Uchida, T., 2004, 3D magnetotelluric modeling using the T-Ω method, *Geophysics*, **69**, 108-119.

Mitsuhata, Y., Matsuo K., and Minegishi, M., 1999, Magnetotelluric survey for exploration of a volcanic-rock reservoir in the Yurihara oil and gas field, Japan, Geophysical Prospecting, **47**, 195-218.

Mitsuhata, Y., Uchida, T., and Amano, H., 2002, 2.5-D inversion of frequency-domain electromagnetic data generated by a grounded-wire source, *Geophysics*, **67**(6), 1753-1768.

Mogi, T., 1996, Three-dimensional modeling of magnetotelluric data using finite element method, *Journal of Applied Geophysics,* **35**, 185-189.

Mosher, C.R.W., and Farquharson, C.G., 2013, Minimum-structure borehole gravity inversion for mineral exploration: A synthetic modeling study, *Geophysics*, **78**(2), 25-39.

Nédélec, J.C., 1980. Mixed finite element in $R^3$: *Numerische Mathematik*, **35**, 315-341.

Newman, G.A., and Alumbaugh, D.L., 1995. Frequency-domain modelling of airborne electromagnetic responses using staggered finite differences, *Geophysical Prospecting*, **43**, 1021-1041.

Newman, G.A., and Alumbaugh, D.L., 2000, Three-dimensional magnetotelluric inversion using non-linear conjugate gradients, *Geophysical Journal International*, **140**, 410-424.

Newman, G.A., and Boggs P.T., 2004, Solution accelerators for large-scale three - dimensional electromagnetic inverse problems, *Inverse Problems*, **20**, S151-S170.

Newman, G.A., and Hoversten, G.M., 2000, Solution strategies for two- and three-dimensional electromagnetic inverse problems, *Inverse Problems*, **16**, 1357-1375.

Nocedal, J., and Wright, S., 1999, Numerical Optimization, Springer-Verlag, New York.

Pedrera, A., Martos-Rosillo, S., Galindo-Zaldivar, J., Rodriguez-Rodriguez, M., Benavente, J., Martin-Rodriguez, J., F., and Zuniga-Lopez, M., I., 2016, Unravelling aquifer wetland interaction using CSAMT and gravity methods: the Mollina-Camorra aquifer and the Fuente de Piedra playa-lake, southern Spain, *Journal of Applied Geophysics*, **129**, 17-27.

Rodi, W., and Mackie, L.R., 2001, Nonlinear conjugate gradients algorithm for 2-D magnetotelluric inversion, *Geophysics*, **66**(1), 174-187.

Rodi, W.L., 1976, A technique for improving the accuracy of finite element solutions for Magnetotelluric data, *Geophysical Journal International*, **44**(2), 483-506.

Saad, Y., 1990, Sparskit: A basic tool kit for sparse matrix calculations, Report RIACS-90-20: Research Institute for Advanced Computer Science, NASA, AMES Research Center.

Saad, Y., 1996, Iterative methods for sparse linear systems, Prindle,Webber & Schmidt.

Saad, Y., and Schultz M.H., 1986, GMRES: A generalized minimal residual algorithm for solving nonsymmetric linear systems, *SIAM J. Sci. and Stat. Comput*., **7**(3), 856-869.

Sadiku, M.N.O., 2001, *Elements of electromagnetics*, Oxford University Press.

Sadiku, M.N.O., 2001, *Numerical Techniques in Electromagnetics*: 2nd Ed., CRC Press LLC.

Sandberg. S.K., and Hohmann, G.W., 1982, Controlled-source audiomagnetotellurics in geothermal exploration, *Geophysics*, **47**, 100-116.

Sasaki, Y., 2001, Full 3-D inversion of electromagnetic data on PC., *Journal of Applied Geophysics,* **46**, 45-154.

Sasaki, Y., Yoshihiro, Y., and Matsuo, K., 1992. Resistivity imaging of controlled-source audio-frequency magnetotelluric data, *Geophysics*, **57**, 952-955.

Savin, C., Ritz, M., Join, J., Bachelery, P., 2001, Hydrothermal system mapped by CSMAT on Karthala volcano, Grande Comore Island, Indian Ocean, *Journal of Applied Geophysics*, **48**, 143-152.

Schwarzbach, C., 2009, Stablility of Finite Element Solutions to Maxwell's Equations in Frequency Domain, PhD thesis, Technische Universität Bergakademie Freiberg.

Schwarzbach, C., Börner, R.-U., and Spitzer, K., 2011, Three-dimensional adaptive higher order finite element simulation for geo-electromagnetics-a marine CSEM example, *Geophysical Journal International*, **178**, 63-74.

Si H., 2015, TetGen, a Delaunay-Based Quality Tetrahedral Mesh Generator, *ACM Trans. on Mathematical Software*, **41** (2), Article 11.

Siripunvaraporn, W., 2012, Three-dimensional magnetotelluric inversion: An introductory guide for developers and users, *Survey in Geophysics*, **33**, 5-27.

Siripunvaraporn, W., and Egbert, G., 2009, WSINV3DMT: Vertical magnetic field transfer function inversion and parallel implementation, *Physics of the Earth and Planetary Interiors*, **173**, 317-329.

Spies, B.R., and Frischknecht, F.C, 1991, *Electromagnetic Sounding*, in Nabighian, M.N., Ed., Electromagnetic methods in applied geophysics: Society of Exploration Geophysicists, 2, 285-422.

Spitzer, K., 1998, The three-dimensional DC sensitivity for surface and subsurface sources, *Geophysical Journal International*, **134**, 736-746.

Streich, R., 2009. 3D finite-difference frequency-domain modeling of controlled-source electromagnetic data: direct solution and optimization for high accuracy, *Geophysics*, **74**, F95-F105.

Šumanovac, F., and Orešković, J., 2018, Exploration of buried carbonate aquifers by the inverse and forward modelling of the Controlled Source Audio-Magnetotelluric data, *Journal of Applied Geophysics*, **153**, 47-63.

Usui, Y., Ogawa, Y., Aizawa, K., Kanda, W., Hashimoto, T., Koyama, T., Yamaya, Y., and Kagiyama, T., 2017, Three-dimensional resistivity structure of Asama Volcano revealed by data-space magnetotelluric inversion using unstructured tetrahedral elements, *Geophysical Journal International*, **208**, 1359-1372.

Wang, G., Lei, D., Zhang, Z., Hu, X., Li, Y., Wang, D., and Zhu, W., 2018, Tensor CSAMT and AMT studies of the Xiarihamu Ni-Cu Sulfide Deposit in Qinghai, China, *Journal of Applied Geophysics*, **159**, 795-802.

Wang, K., and Tan H., 2017, Research on the forward modeling of controlled-source audio-frequency magnetotellurics in three-dimensional axial anisotropic media, *Journal of Applied Geophysics,***146**,27-36.

Wannamaker P.E., Hohmann, G.W., and SanFilipo W.A., 1984, Electromagnetic modeling of three-dimensional bodies in layered earths using integral equations, *Geophysics*, **49**(1), 60-74.

Wannamaker, P.E., 1997, Tensor CSAMT survey over the Sulphur Springs thermal area, Valles Caldera, New Mexico, U.S.A., Part I: Implications for structure of the western caldera, *Geophysics*, **62**(2), 451-465.

Ward, S.H., and Hohmann, G. W., 1988, *Electromagnetic theory for geophysical applications*, in M.N., Nabighian, M.N., Ed., Electromagnetic methods in applied geophysics: Society of Exploration Geophysicists, 1, 131-388.

Weiss, C.J., 2013, Project APhiD: A Lorenz-gauged A-$\Phi$ decomposition for parallelized computation of ultra-broadband electromagnetic induction in a fully heterogeneous Earth, *Computers & Geosciences*, **58**, 40-52.

Whitney, H., 1957, *Geometric Integration Theory*: Princeton University Press.

Yano, H., Wu, Y., Taguchi, S., Chowdhury, S., Taguchi, G. 2005, *Taguchi's Quality Engineering Handbook*. US: Wiley.

Yee, K., 1966, Numerical solution of initial boundary value problems involving Maxwell's equations in isotropic media, *IEEE Transactions on Antennas and propagation*, **14**, 302-307.

Zhang M., Farquharson, C.G., and Liu, C., 2020, Response characteristics of gradient data from the frequency-domain controlled-source electromagnetic method, *Journal of Applied Geophysics*, **172**, 103873.

Zhang, J., Mackie R.L., and Madden, T.R., 1995, 3-D resistivity forward modeling and inversion using conjugate gradients, *Geophysics*, **60**(5), 1313-1325.

Zonge, K.L., and Hughes, L.H., 1991, *Controlled-source audio-frequency magnetotellurics*, in Nabighian, M.N., Ed., Electromagnetic methods in applied geophysics: Society of Exploration Geophysicists, 2, 713–809.

# Appendix A

# Elements of the coefficient matrix

The closed forms of the inner product integrals in the coefficient matrix are given here. For the full derivation of the equations, see Ansari (2014) and Jin (2014).

The first inner product integral is the interaction of the curl of vector basis functions between two edges:

$$C_{ij} = \int_V \left(\nabla \times \mathbf{N}_i\right) \cdot \left(\nabla \times \mathbf{N}_j\right) dV = \frac{4\ell_i^e \ell_j^e V^e}{(6V^e)^4}(K_1 + K_2 + K_3) \tag{A.1}$$

where $\ell$ is the length of the edges for a particular element and $V$ is the volume of the element. The terms $K_1$, $K_2$, and $K_3$ are given as the following:

$$K_1 = \left(c_{i1}d_{i2} - d_{i1}c_{i2}\right)\left(c_{j1}d_{j2} - d_{j1}c_{j2}\right) \tag{A.2}$$

$$K_2 = \left(d_{i1}b_{i2} - b_{i1}d_{i2}\right)\left(d_{j1}b_{j2} - b_{j1}d_{j2}\right) \tag{A.3}$$

$$K_3 = \left(b_{i1}c_{i2} - c_{i1}b_{i2}\right)\left(b_{j1}c_{j2} - c_{j1}b_{j2}\right) \tag{A.4}$$

The second term is the interaction of the vector basis functions between two edges:

$$D_{ij} = \int_V \sigma \mathbf{N}_i \cdot \mathbf{N}_j dV = \frac{\sigma^e \ell_i^e \ell_j^e}{(6V^e)^2} \left( L_{i1}^e L_{j1}^e f_{i2\,j2} - L_{i1}^e L_{j2}^e f_{i2\,j1} - L_{i2}^e L_{j2}^e f_{i1\,j2} - L_{i2}^e L_{j2}^e f_{i1\,j1} \right) \tag{A.5}$$

where

$$f_{ij} = b_i^e b_j^e + c_i^e c_j^e + d_i^e d_j^e \tag{A.7}$$

If $i = j$

$$L_i^e L_j^e = \frac{|\mathbf{J}|}{60} \tag{A.7}$$

If $i \neq j$

$$L_i^e L_j^e = \frac{|\mathbf{J}|}{120} \tag{A.8}$$

**J** is the transformation matrix, and it is given as the following:

$$\mathbf{J} = \begin{bmatrix} x_1 - x_4 & x_2 - x_4 & x_3 - x_4 \\ y_1 - y_4 & y_2 - y_4 & y_3 - y_4 \\ z_1 - z_4 & z_2 - z_4 & z_3 - z_4 \end{bmatrix} \tag{A.9}$$

The third inner product integral is the interaction between the vector basis function and the gradient of the scalar basis function:

$$F_{il} = \int_V \nabla N_l \cdot \left( \sigma N_j \right) dV = \frac{\ell_j^e \sigma^e |\mathbf{J}|}{24\left(6V^e\right)^2} \begin{bmatrix} \left( b_{j_2} b_k + c_{j_2} c_k + d_{j_2} d_k \right) \\ -\left( b_{i_1} b_k + c_{i_1} c_k + d_{i_1} d_k \right) \end{bmatrix} \tag{A.3}$$

The fourth term is the interaction between the gradients of the scalar basis functions:

$$H_{lk} = \int_V \nabla N_l \cdot \left(\sigma \nabla N_k\right) dV = \frac{\sigma^e}{36V^e}\left(b_l b_k + c_l c_k + d_l d_k\right) \tag{A.4}$$

# Elements of the source terms

The first source term ($S_1$) deals with the interaction of the vector basis functions and a current segment of a wire.

$$S_1 = \int_V \mathbf{N}_i \cdot \mathbf{J}_e^s dV \tag{A.5}$$

For an x-directed current source, and considering a particular tetrahedron, the above integral can be written as:

$$S_1 = \frac{1}{\left(6V^e\right)^2}\int_V \left(N_x \mathbf{x} + N_y \mathbf{y} + N_z \mathbf{z}\right) \cdot \left(\mathcal{H}\left(x_{i+1}\right) - \mathcal{H}\left(x_i\right)\right) \delta\left(y - y_0\right)\delta\left(z - z_0\right) \tag{A.6}$$

where $N_x$, $N_y$, and $N_z$ are the vector basis functions for the three directions. Because the current segment has only an x-component the above integral can be evaluated as:

$$S_1 = \frac{I\Delta x \ell_j^e}{\left(6V^e\right)^2}\left(a_{i1}b_{i2} - a_{i2}b_{i1}\right) + y_0\left(c_{i1}b_{i2} - c_{i2}b_{i1}\right) + z_0\left(d_{i1}b_{i2} - d_{i2}b_{i1}\right) \tag{A.7}$$

where $\Delta x$ is the segment length, and $I$ is the current.

The second term is the calculation of the dot-product of a vector basis function with the curl of the source term.

$$S_2 = \int_V \mathbf{N}_i \cdot \nabla \times \mathbf{M} dV \tag{A.8}$$

For a vertical magnetization vector, the above integral can be written as:

$$S_2 = \frac{2\ell_j^e m}{\left(6V^e\right)^2}\left(b_{i1}c_{i2} - b_{i2}c_{i1}\right) \tag{A.9}$$

The last source term $S_3$ is given for an x-directed wire:

$$S_3 = -\int_V N_l \nabla \cdot \mathbf{J}_e^s dV \tag{A.10}$$

$$S_3 = \frac{I}{6V^e} b_l \Delta x \tag{A.11}$$